9

Collimation Systems

Contents

9.1 Introduction to Beam Delivery Systems 556
9.1.1 Introduction to Collimation Systems 557
9.2 Post-Linac Collimation 560
9.2.1 Specifications 560
9.2.2 Materials Considerations 569
9.2.3 Tail Re-Population Estimates 578
9.2.4 Wakefield Considerations 587
9.2.5 Lattice Description and Analysis 602
9.2.6 Operational Issues 625
9.2.7 Energy Scaling Laws 629
9.2.8 Nonlinear Collimation Systems 630
9.2.9 Summary and Conclusions 630
9.3 Pre-Linac Collimation 631
9.3.1 Pre-Linac Collimation Function: 631
9.3.2 Pre-Linac Collimation System Requirements: 632
9.3.3 Pre-Linac Collimation Optical Design: 632
9.3.4 Pre-Linac Collimation System Bandwidth 633
9.3.5 Summary 633
9.4 Bunch Length Collimation 634
9.4.1 Introduction 634
9.4.2 Collimator location 635
9.4.3 Particles Loss at Bunch Length Collimators 635
9.4.4 Collimation in the Linac 636
9.4.5 Conclusion and Discussion 637

9.1 Introduction to Beam Delivery Systems

Chapters 9 through 11 describe what are referred to as the beam delivery and removal systems. A schematic of these systems is shown in Figure 9-1. These systems begin at the end of the linac and terminate at a post-IP beam dump. They include a main post-linac collimation system (Section 9.2); an IP switch and big bend (Chapter 10); a pre-final-focus diagnostic and skew-correction section (Section 11.3); a final-focus system (Sections 11.4 to 11.7); and a post-IP beam line (Section 11.8). Chapter 9 also includes the description of the pre-linac horizontal and vertical collimation system (Section 9.3), and a pre-linac bunch-length collimation system (Section 9.4). The design of all of these systems has been strongly influenced by experience with similar systems at the SLC.

Figure 9-2 shows the horizontal and vertical beam envelope from the linac to the IP for the 1-TeV-c.m. beam line, and Figure 9-3 shows the corresponding β functions. The total length is 5.2 km. The first 50 meters contain a post-linac diagnostic chicane, which is then followed by a 2.5-km collimation system. The maximum horizontal points of the envelope in the collimation region, for the most part, correspond to the location of horizontal collimators and chromatic correction sextupoles; the maximum points of the vertical envelope are usually the location of vertical collimators and chromatic correction sextupoles. The next horizontal envelope peak, at 2.6 km, marks the location of the IP switch. After that, up to the 3.0-km marker, is a small envelope region that contains the big (10-mr) bend, and following this, up to the 3.4-km marker, is a small envelope region containing the pre-final-focus diagnostic region. In this region beam sizes in all phases and planes can be measured and the presence of coupling detected and corrected. The region from 3.4 km to 3.8 km contains the beta match into the final focus. Following the beta match, the first two peaks in the horizontal envelope are the positions of the horizontal chromaticity compensation sextupoles. The two large vertical envelope points following these, at about 4.4 km and 4.7 km, are the positions of the vertical chromatic compensation sextupoles. The last peak, in each plane, at the end of the beam line, is located at the position of the final-doublet elements.

Figure 9-4 shows the horizontal dispersion function for the same beam line. The peaks at the very beginning of the beam line are in a post-linac diagnostic region. These regions are similar to others along the linac and are described in Section 7.9.5. Following this and continuing to 2.4 km, one sees the dispersion function of the collimation system. The peak at 2.6 km is in the IP switch, and the small dispersion wiggles which follow are located in the big bend. The small bump at 3.4 km, at the beginning of the beta-match region in the final-focus system, is a short region containing two bends which provide an adjustable entry angle into the final-focus region. The net bend here will have three distinct values corresponding to three distinct final-focus systems that are required to cover the energy range from 350-GeV to 1.5-TeV c.m. Each has slightly different internal bend angles, but all reside on the same support bench and have the same IP location. The layouts are shown in Figure 11-9. The remaining dispersion is in the final-focus system.

We have studied all beam delivery systems for center-of-mass energies from 350 GeV to 1.5 TeV for a broad range of assumptions on beam and IP parameters, and have shown that it is possible to meet the specifications for this entire range. Above 1.0-TeV c.m. the elements of the collimation system also must be relocated. The tunnel length allotted to collimation is adequate to collimate energy and the horizontal and vertical planes at both phases only one time at 1.5-TeV c.m. Since the centroid orbit of the collimation system differs only slightly from a straight line, it would be possible to allocate length at the end of the linac tunnel for collimation at energies above 1-TeV c.m. And it should be sufficient to collimate the FD phase only one time in the collimation system. See Section 9.2.3 for details.

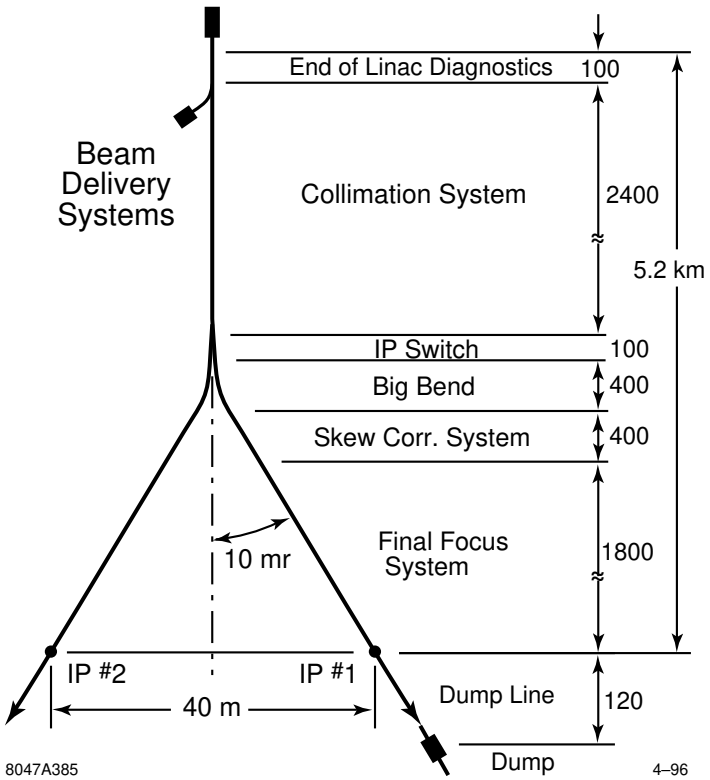

Figure 9-1. *A schematic layout of the beam delivery systems.*

9.1.1 Introduction to Collimation Systems

The post-linac collimation section (Section 9.2) begins with a discussion of system specifications since the design is strongly influenced by assumptions on incoming beam conditions: Of the 10^{12} particles per bunch train, how many particles must be routinely collimated, and how many particles can be safely collimated in the final-focus system? Because the number of particles needing to be collimated is difficult to predict precisely, since it depends on how well the upstream systems have been tuned, we have relied on SLC experience for this estimate. The number of particles that can be collimated in the final-focus system has been determined by edge-scattering and muon transport studies within the final-focus system. These studies are described in Chapter 12. The rough guideline that evolves from these considerations is that there may well be a few times 10^{10} particles in the beam tails at the end of the linac and this number needs to be reduced to a few times 10^6 upon entry into the final-focus system.

Two types of collimation systems have been proposed: linear and nonlinear. In the former, the beam sizes at the collimator are achieved by traditional linear optics methods (quadrupoles); in the latter strong sextupoles are used to blow up the beam. Since the sextupoles are exceedingly strong and system lengths are not reduced in the specific system proposals we have studied, we have opted to look in depth at a linear collimation scheme. It is not precluded that a nonlinear (or combination linear and nonlinear) system could be found that would be operationally superior and have a lower total cost. Our primary objective is to show that at least one collimation system exists that fulfills all functional requirements.

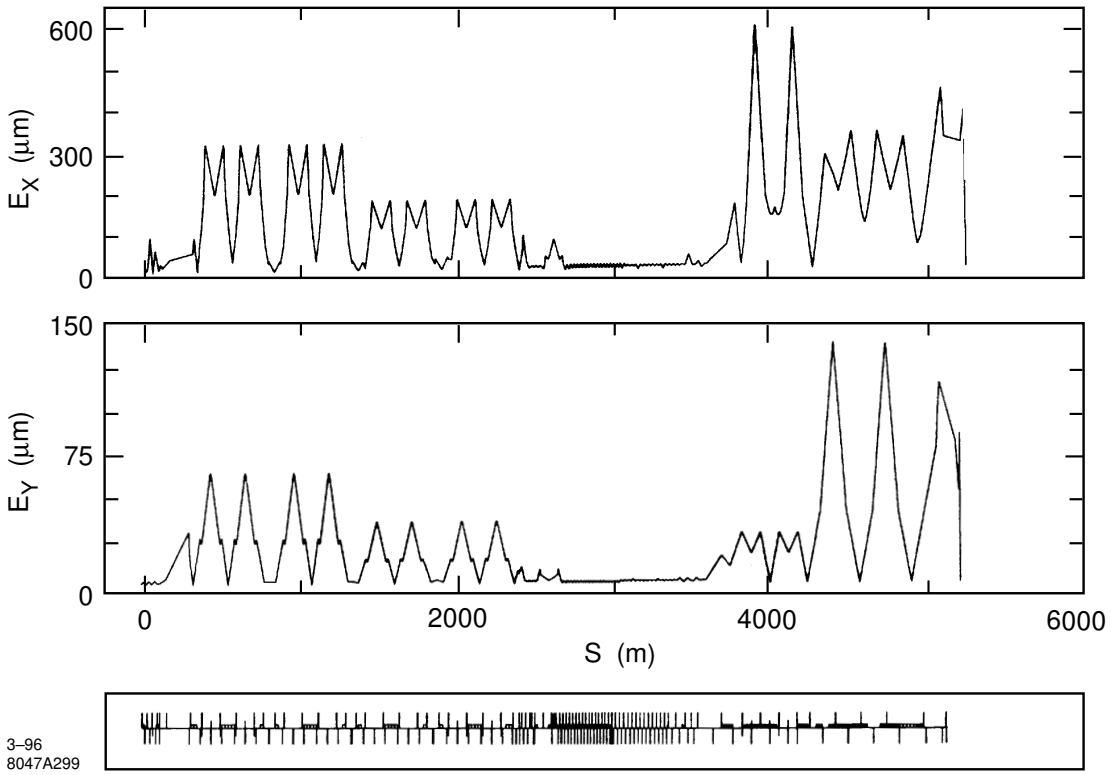

Figure 9-2. *The horizontal and vertical beam envelope from the linac to the IP for the 1-TeV-c.m. beam line.*

Since a small perturbation in upstream conditions could cause a complete bunch train of 10^{12} particles to be incident on the collimators of the collimation system, it is necessary in both the linear and nonlinear systems to rely on a primary collimator that is a spoiler, followed by a secondary collimator which is the absorber. The spoilers must be thermally rugged and very thin ($\leq 1/4$ radiation length). The best material we have found for spoilers is a titanium alloy plated with pure titanium or titanium nitride (TiN) for improved electrical conductivity. The function of the spoilers is to increase the angular divergence of the beam, so that when the beam arrives at the absorber it has a much larger size (millimeters). The absorber, on the other hand, must be able to routinely absorb and remove the energy in the tail of the beam. For the 1-TeV c.m. parameters, 1% of the time-averaged beam power is 84 kW. The preferred material for absorbers is copper.

The wakefields of the collimators can have a very deleterious effect on the beam core. To minimize the wakes, the beam pipe must be tapered before and after the collimator. Even for an on-axis beam core, a parallel-jaw collimator will have a quadrupole wake, which can influence focusing of the core and the trajectory of particles in the tails. And beams that have been mis-steered close to the wall can experience very large wake-induced kicks. All of these wake effects are described in Section 9.2.4.

We consider the geometric wakefields for tapered collimators to be uncertain. There are theoretical results which we will discuss below, but the small tapers and short bunch lengths have made these collimators very hard to simulate with existing numerical modeling codes. The geometric wake for the parallel-plate geometry has changed as this document was going to press. We have incorporated notes in the text describing the change. If the new result stands, because the geometric-part of the wake is now larger than the cylindrical

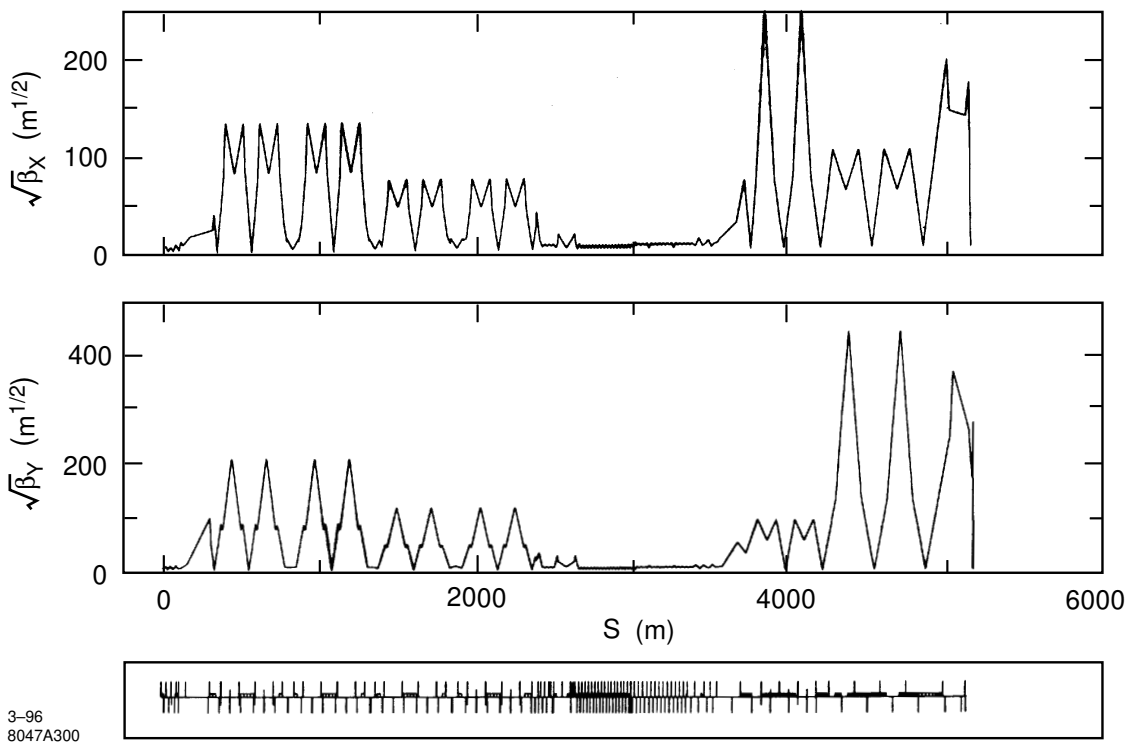

Figure 9-3. *The horizontal and vertical β function from the linac to the IP for the 1-TeV-c.m. beam line.*

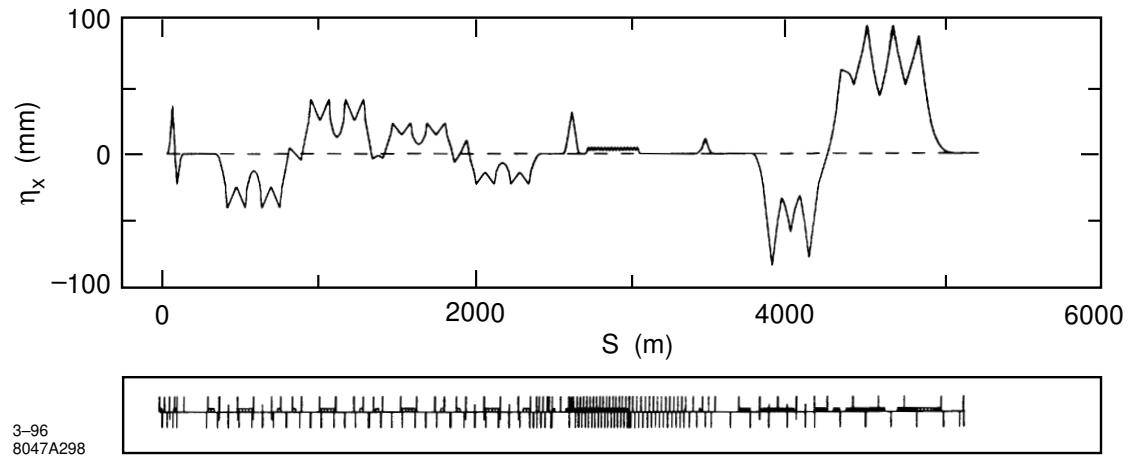

Figure 9-4. *The horizontal dispersion function from the linac to the IP for the 1-TeV-c.m. beam line.*

wake by a factor of about 4, there would be an impetus to use the less-convenient cylindrical geometry collimators.

There has also been some doubt cast on the correctness of the resistive-wall wake formulae we have used for the tapered collimators. A recent measurement of collimator wakes at the SLC has given a wakefield kick that is stronger than expected. The situation indicates a need for clarifying experiments with tapered collimators.

Because of the large β-functions and strong focusing that arise when the beam is blown up with linear optics, there are important chromatic effects to compensate with sextupole pairs. And because it is necessary to collimate each transverse phase at least one time, there are very large R_{12} and R_{34} functions within the system. Large R_{12} and R_{34} functions lead to important tolerances described in Section 9.2.5. Stability tolerances, that must be held between tunings of the waist knobs in the skew correction system, are looser than those within the final-focus system. However the particle backgrounds in the collimation system preclude the beam-based stabilization methods contemplated for the final-focus system. Alternatives are discussed in Section 9.2.6.

Vibration tolerances that must be met between orbit adjustments are greatly simplified by the ground motion studies described in Appendix C which, when applied to the collimation system, show that seismic ground motion has a negligible impact on beam collision offsets at the IP. As a result, vibration tolerances become tolerances between beam-line elements and the ground beneath them, or tolerances on ground motion coming from cultural sources.

9.2 Post-Linac Collimation

9.2.1 Specifications

Incoming Beam Parameter Range

The important parameters from the point of view of the collimation system are:

i) $Nn_b/\sqrt{(\varepsilon_x^N \varepsilon_y^N)}$, total bunch-train charge divided by the square root of the normalized emittance product, for single pulse-train spoiler survival;

ii) $N/(\varepsilon_x^N \sigma_z^{2/3})$ and $N/(\varepsilon_y^N \sigma_z^{2/3})$, for determination of minimum n_x^2 and n_y^2 that can be collimated in each plane (see Eq. 9.45); and

iii) the worst-condition population in tails, for average power loads on absorbers.

The strange units result from omission of a dependence on the surface resistivity of the collimators.

The range of IP parameters under consideration is given in Chapter 12, Table 12-1. Here one sees a maximum charge per bunch of $N = 1.25\ 10^{10}$, a maximum charge per bunch-train of $Nn_b = 1.125\ 10^{12}$, a minimum bunch length of $100\,\mu$m, a minimum horizontal normalized emittance of $\varepsilon_x^N = 4\ 10^{-6}$ m-rad, and vertical normalized emittances which vary from $\varepsilon_y^N = 8$ to $17\ 10^{-8}$ m-rad. The emittances at the end of the linac can be somewhat smaller and, depending on linac alignment conditions, could be as small as $\varepsilon_x^N = 4\ 10^{-6}$ m-rad and $\varepsilon_y^N = 5\ 10^{-8}$ m-rad.

Limit ii) implies that $n_x\sigma_x$ and $n_y\sigma_y$ are independent of energy and emittance. Thus if the downstream beta functions do not change, the physical apertures that may be collimated are independent of energy and incoming beam emittance.

The most sensitive parameter is that of item i), because the required value of the β functions at the spoilers depends on this ratio, and the system length increases as this β function becomes larger.

For evaluating worst conditions we assume the values $\varepsilon_x^N = 4\ 10^{-6}$ m-rad, $\varepsilon_y^N = 5\ 10^{-8}$ m-rad, and $N = 1.25\ 10^{10}$. The worst ratio $N/\sigma_z^{2/3}$, in the parameter range of Table 12-1, occurs when $N = 1.25\ 10^{10}$ and $\sigma_z = 150\,\mu$m. We also assume that a maximum of 1% of the beam may need to be collimated in any phase and any plane, or in energy. The total beam fraction collimated could be as high as 5%. This assumption is discussed in the next section.

Incoming Beam Halo Specification

Experience with the SLC has identified several sources of halo particles: those created

i) during extraction from the damping ring,

ii) in the bunch compressor,

iii) by wakefields within the linac,

iv) by mismatches, misalignment and steering errors in the linac,

v) from acceleration of dark current,

vi) from hard Coulomb and/or bremsstrahlung scattering within the linac, and

vii) from faulty multi-bunch energy compensation.

The first two items may be addressed by the pre-linac collimation system (Section 9.3). A bunch-length collimation system (Section 9.4) can reduce contributions from item iii). Linac diagnostics are intended to reduce iv). Since the injection energy into the linac is at 10 GeV, dark current will be considerably off-energy and presumably not accelerated far.

Item vi) cannot be eliminated, but the number of particles in the tail from this source can be derived [Yokoya 1991] beginning with the scattering angle

$$\Delta\theta = \frac{2Zr_e}{\gamma b} \tag{9.1}$$

of an electron passing at distance b from a nucleus with charge Z. For an azimuthal orientation of an angle ϕ specifying initial conditions, the kick in the horizontal direction would be $\Delta\theta_x = \Delta\theta\cos\phi$. For $\Delta\theta_x \geq n_x\sigma'_x$ we must have $b \leq b_n$ with

$$b_n(\phi) = \frac{2Zr_e}{\gamma n_x \sigma_{x'}}\cos\phi \quad . \tag{9.2}$$

Hence the cross-section for scattering beyond $n_x\sigma'_x$ is

$$\sigma_n = \int_0^{2\pi} d\phi \int_0^{b_n(\phi)} b\,db = \pi b_n^2(0) \quad . \tag{9.3}$$

If ρ is the density of nuclei, then the fraction of particles scattered beyond $n_x\sigma_{x'}$ in length ds is given by

$$\frac{\Delta N}{N} = \pi\rho \int b_n^2(0)ds = \frac{2\pi r_e^2 \rho Z^2}{n_x^2 \varepsilon_x^N} \int \frac{\beta_x(s)ds}{\gamma(s)} \tag{9.4}$$

This can be integrated over the length of the linac. The β function oscillates between minimum and maximum values that scale roughly as the square root of energy (See Chapter 7, Figure 7-1 and 7-2. This oscillation is much more rapid than the change of γ so it may be replaced by an appropriate average, $\xi\beta_x^{\max}(s) = \xi\beta_x^{\max}(0)\sqrt{[\gamma(s)/\gamma(0)]}$. We may take $d\gamma/ds$ to be a constant and carry out an integral over γ to obtain

$$\frac{\Delta N}{N} = \frac{4\pi r_e^2 \sum_i \rho_i Z_i^2}{n_x^2 \varepsilon_x^N} \frac{\xi\beta_x^{\max}(0)L}{\sqrt{\gamma(L)\gamma(0)}} \quad . \tag{9.5}$$

We have included a sum over nuclear species, ρ_i being the density of nuclear species with charge Z_i. If the partial pressure associated with a nuclear species is P_{Gi} then the number of nuclei per unit volume is given by $\rho_i \approx 3\ 10^{22} n_i P_{Gi}\ m^{-3}$ where n_i is the number of nucleons per atom. If we take the major composition of gas within the beam pipe to be N_2 with nuclear charge $Z = 7$, and take $P_G = 10^{-8}$ Torr, $\gamma(0) = 2\ 10^4$, $d\gamma/ds = 10^2$, and $\beta_x^{\max}(0) = 10$ m, we obtain the estimate

$$\frac{\Delta N}{N} \approx \frac{1.4\ 10^{-7}}{n_x^2} \quad \text{or, in a similar manner} \quad \frac{\Delta N}{N} \approx \frac{1.4\ 10^{-5}}{n_x^2} \quad . \tag{9.6}$$

For $N = 10^{12}$, $\Delta N \approx 1.4\ 10^5/n_x^2$ or $\Delta N \approx 1.4\ 10^7/n_y^2$. For collimation at $n_x = 5$ or $n_y = 35$, $\Delta N < 10^4$. We will see below that this number of particles could be safely collimated in the final-focus system.

Bremsstrahlung interactions with beam gas can result in particle energy loss and create tails. The cross section for this process is given in Eq. 11.118. For more than 1% energy loss the cross section is estimated to be about $\sigma_{brems} \approx 6$ barn. This gives the estimate

$$\frac{\Delta N}{N} \approx 2\ 10^{-5} P_G L \tag{9.7}$$

where P_G is the gas pressure in Torr and L is the linac length in meters. For $N = 10^{12}$, $L = 10^4$, and $P_G = 10^{-8}$, we have $\Delta N \approx 2\ 10^3$, which is a smaller number than from Coulomb scattering.

Hence the principal source of concern is item iii), the tail particles generated by wakes in the linac. Compared to the SLC, the bunch-length collimation and pre-linac collimation should help reduce this number, but the number of particles in the longitudinal tails under typical (and worst!) operating conditions remains uncertain. Estimates indicate that tail populations should be less than 10^{-3} or even 10^{-4} [Raubenheimer 1995]. On the other hand, at the SLC it has been necessary on occasion to collimate 10% of the beam particles. When the systems are tuned this number is an order of magnitude smaller.

Assuming that the pre-linac collimation systems and other efforts to minimize tail particles will have a positive impact, we somewhat arbitrarily have adopted the specification that at most 1% of the beam will require collimation at any particular phase, transverse plane, or energy. The system to be described will actually have somewhat higher totals, up to 5%, depending on how beam tails are proportioned. The main impact of choosing a larger collimation percentage is in the size of the absorbers, and they could be designed to remove a higher (or lower) average power load if it was deemed necessary.

Required Collimation Depths

Final-doublet (FD) Phase Depth. The collimation depth at the final-doublet (FD) phase, $\pi/2$ from the interaction-point (IP) phase, is determined by beam emittances and the apertures and β functions in

the final-doublet quadrupoles. The final-doublet β functions are determined by the IP β functions and the final-doublet design parameters: the free space from the last quadrupole to the IP and the strength of the quadrupoles.

Final-doublet designs get more compact and have smaller chromaticity for larger quadrupole gradients, so there is a preference for small apertures. But as we have mentioned in Section 9.2.1 above and shall show below in Section 9.2.4, given β in the doublet, there is a minimum beam aperture, $n_x\sqrt{(\varepsilon_x\beta_x)}$, that can be collimated which is determined by the ratio $N^{1/2}/\sigma_z^{1/3}$. Hence the final-doublet aperture is chosen as small as possible subject to the limits of the collimation system, the range of IP β functions which is to be accommodated, and resistive-wall and geometric wake considerations.

The IP β functions are adjusted to an optimum during operation. If the beam is free from tail particles, the optimum will be determined by the maximum luminosity, or equivalently the minimum IP spot size that can be obtained with the given beam emittance. As the IP β functions are decreased, the linear spot size gets smaller, but the strengths of aberrations from nonlinearities in the final-focus system get larger. The values of the IP β functions shown in the parameter sets of Chapter 12, Table 12-1 will be close to the optimum. Synchrotron radiation, Oide effect and beamstrahlung control are also involved in finding the optimum.

Tail particles create problems in two ways (see Chapter 12 for details): i) by impacting an element of the final doublet, or ii) radiating photons which impact the final doublet. Studies of shower particles and their trajectories through the detector show that only tens of particles per bunch train can be allowed to impact the final doublet. Studies of synchrotron radiation lead to the guideline that the horizontal final-doublet aperture should be twice the collimated aperture, and the vertical aperture should be 1.5 times the collimated aperture.

The answer to the question, "What should be the final-doublet phase collimation depth?" turns out to be "As small as possible." As we shall see below, for the beam parameters under discussion, the minimum collimation apertures are $5\,\sigma_x$ and $35\,\sigma_y$. There needs to be some margin on this number, since the apertures must be gradually enlarged in successive collimation stages, and by the final doublet these minima may increase to $7\,\sigma_x$ and $40\,\sigma_y$. Following the synchrotron radiation guidelines, the final-doublets apertures should be chosen to be equal or greater than $14\,\sigma_x$ and $60\,\sigma_y$. Final-doublet designs are discussed in Section 11.6 and particle trajectories are shown in Section 11.6.5.

Interaction Point (IP) Phase Depth. The collimation depth for the interaction-point (IP) phase can be larger than the final-doublet (FD) phase since in the final-focus system the IP phase is demagnified, and apertures for this phase are more than $45\,\sigma_x$ and $200\,\sigma_y$. Figure 9-5 shows the dynamic aperture of the horizontal and vertical phases of the final-focus system determined from tracking.

There are several advantages of collimating the IP phase at a larger aperture than the FD phase.

i) The wakes will be smaller, and since these wakes give rise to jitter in the final-doublet phase, the beam jitter is reduced in the final-focus system, which is helpful for tuning.

ii) The β functions in the second stage IP-phase collimation can be chosen smaller. This means that the IP-phase collimation section can be shorter and the tolerances less severe.

The smaller β functions of item ii) can only be achieved in the first IP collimation stage if one abandons the principle that the spoiler should be able to survive the impact of a full bunch train. This needs to be carefully evaluated in the context of the machine protection system.

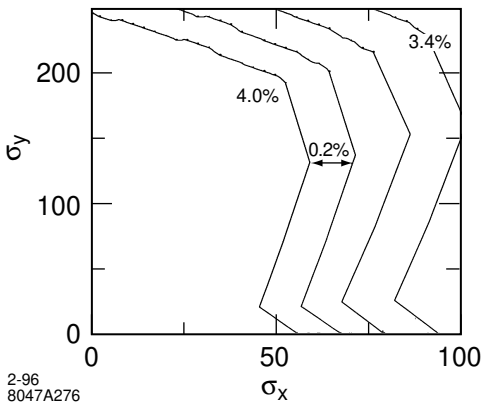

Figure 9-5. *The dynamic aperture of the final-focus system for the IP phase. The FD phase particles have been restricted to be within a diamond region in the $x - \delta$ plane defined by the collimation system, with $|x| \leq 7\sigma_x$ and $|\delta| \leq 0.04$.*

Just how large the collimation in the IP phase can be also depends on beam-line transport within the collimation system and from the collimation system to the IP. The beam line from the collimation system to the final-focus system must be achromatic, so that off-energy IP-phase particles do not migrate into the FD phase. It also requires that there not be significant residual beam-line aberrations from sextupoles or interleaved sextupoles, which distort the phase space of large amplitude particles. These question are addressed in Section 9.2.5.

There is a further constraint on IP-phase apertures that comes from machine-protection considerations. Mis-steered beams that come close to collimator apertures experience very large wake kicks, and can be steered into unprotected downstream absorbers. As we will see below, it is necessary to have two stages of IP collimation in the collimation system. The machine protection considerations alluded to will require that the second stage collimation have an aperture that is much larger than the first stage. These issues are discussed in detail in Sections 9.2.4, "Quadrupole and Large Amplitude Wakes of Parallel Plate Collimators", and "Consequences of Quadrupole and Near-Wall Wakes". We assume throughout that the collimators in the first IP stage are protected by spoilers that can withstand the impact of a full pulse train.

Energy Collimation Depth. The required energy collimation depth also depends on the properties of the lattice between the collimator and the final doublet. If an off-energy beam is able to pass through the spoilers, it should not be able to impact any downstream collimator in the collimation system or in the final-focus system. Figure 9-6 shows the result of tracking particles through the beam line from the end of the collimation system to the IP for an early beam-delivery lattice. The initial coordinates are chosen at the collimator edges of $6\,\sigma_x$ and $40\,\sigma_y$, in both the IP and FD phase, and tracked to the location of the horizontal and vertical collimators of the final-focus system. One sees in Figure 9-6 the image of these particles when they are off-energy by various amounts from 0 to -6%. Based on these and similar studies described in Section 9.2.5 we have chosen 4% as the energy collimation depth.

Because of the large β functions in the collimation system, there must be a chromatic correction scheme of sextupoles placed in dispersive regions [Brown 1979]. It is natural to take advantage of this dispersion function to collimate energy at the same locations where the horizontal plane is collimated. Though the magnitude of the dispersion function is somewhat flexible, 4% energy collimation turns out to be a possible and convenient energy depth.

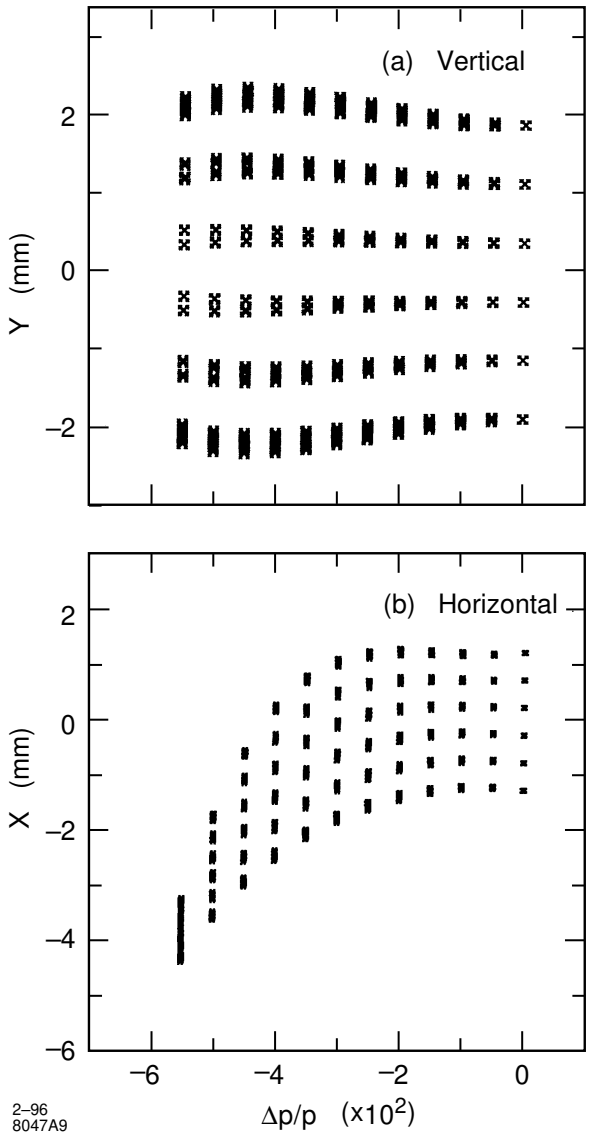

Figure 9-6. *The position of particles at the horizontal collimator in the final-focus system for particles launched in the collimation system on the boundary of the collimation aperture for several energy offsets.*

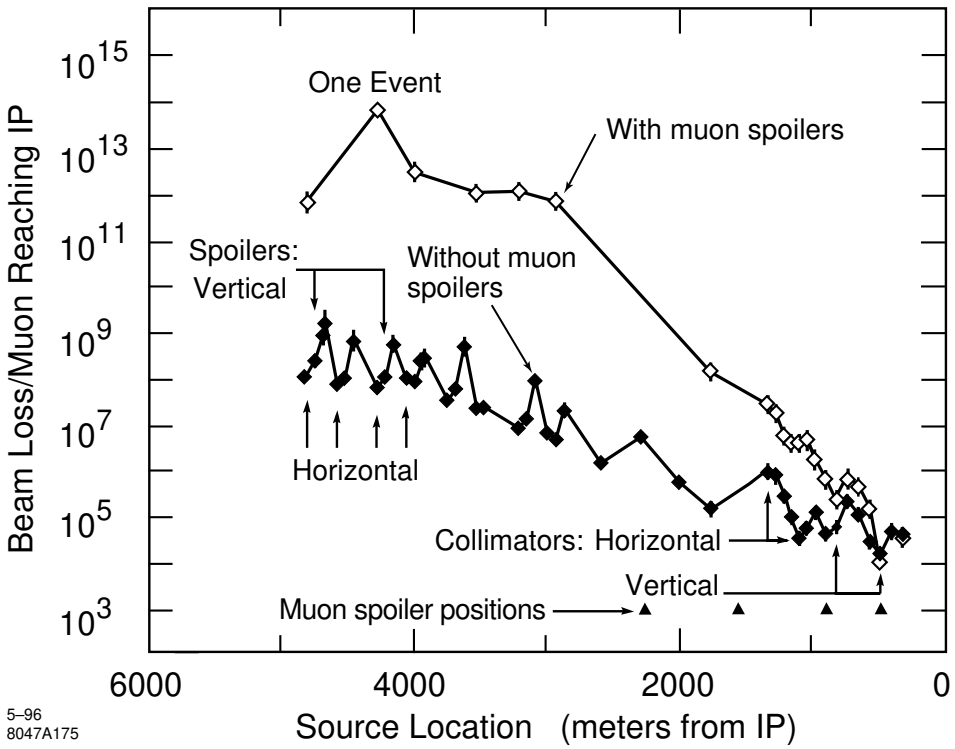

Figure 9-7. *Graph showing electrons that may be collimated if only 1 muon is to reach the detector.*

Limits on Collimation in the Final-focus System

The CCX and CCY chromatic correction sections in the final-focus system provide excellent locations for collimators. However collimation here can create unacceptable muon backgrounds. Figure 9-7 shows the number of particles that may be collimated, and still have just one muon pass through the detector. If muon toroids are placed in the final-focus tunnel, one finds that 10^5 particles may be collimated in the CCY and 10^6 may be collimated in the CCX.

Figures 9-8 and 9-9 show the results of edge scattering within the final-focus system. These studies indicate that less than 1 particle in 10^5 of the particles that re-enter the beam at the collimator edge actually impact the final doublet. This simulation was done assuming the angular and energy edge-scattering profiles presented in Section 9.2.3. In fact no particles in this study impacted the final doublet. Either the particles impacted the beam line between the collimator and the doublet (at the latest in the bend in the final telescope) or they passed through the IP. Particles that are close to full energy will miss the doublet because the collimators are π from the final doublet and have a smaller aperture than the final doublet. About 10% of the particles are in this category. Particles that are off-energy don't make it through the bends. Since only one particle re-enters the beam for every 10 particles per micron incident on the edge of the collimator, this study would say that there is an allowed density of 10^6 particles per micron on these collimators. Since the muon studies conclude that only 10^5 to 10^6 particles may be incident on the whole collimator, the muon studies set the limits on the number of particles that may be collimated in the final-focus system.

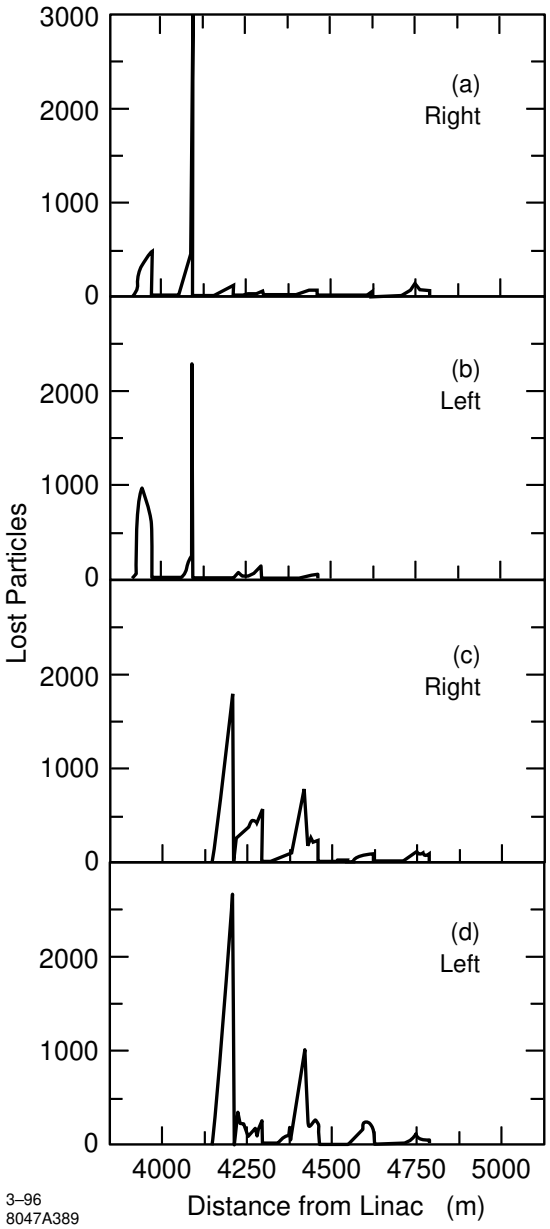

Figure 9-8. *Edge scattering results from the right and left edge of the two horizontal collimators in the CCX section of the final-focus system. In each case 100,000 particles were released from the edge according to angular and energy distributions determined from EGS studies (see Section 9.2.3). The curves give the number of particles which impact elements (or the beam pipe) along the beam line. In both cases no particles impact the final doublet or final-doublet region. About 10% of the particles pass through the IP.*

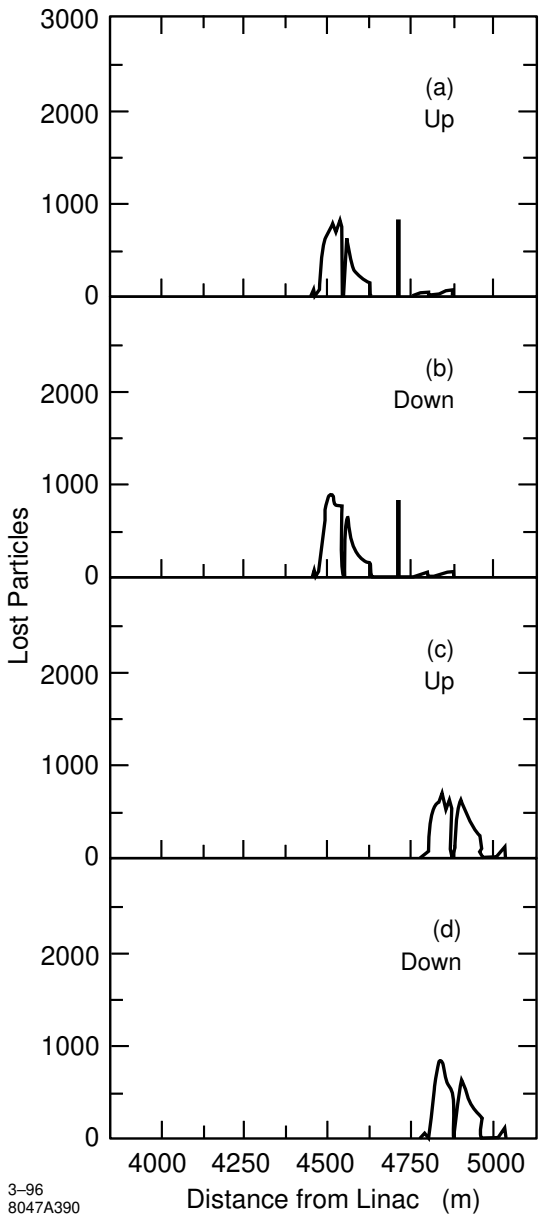

Figure 9-9. *The distribution of impact position for particles edge-scattered from the edge of the vertical collimators at the sextupoles in the CCY region of the final-focus system. A total of 100,000 particles were released from the collimator edge according to the angle and energy distributions shown in Figures 9-19–9-21. None of these particles impact the final doublet. About 10,000 pass through the IP. "Up" and "down" are from the top and bottom edges, respectively.*

Studies described in Chapter 12 indicate that tens of particles can be incident on the final doublet per bunch train without saturating the vertex detector. We conclude that the principal source of such particles will be from scattering on gas particles in the final-focus system. See Section 11.5.5, Eq 11.68 for an estimate of this source.

9.2.2 Materials Considerations

Machine Protection Issues

Single-Bunch Passive Protection. The machine protection strategy (see Chapter 16) consists of a two-level scheme. At level 1 the beam line should be able to passively survive the transport of a single bunch, no matter the state of any device in the beam line. At level 2, which assumes that a single bunch is known to successfully travel through the beam line to a beam dump, the emittance of the single bunch can be reduced and the number of bunches can be increased. It is now the responsibility of the machine protection system to detect any state changes in the system that could lead to the beam not being safely transported to a dump. Upon detection of such a state change it must be possible to turn off the beam before any component is damaged.

For a single bunch, the area of the beam when encountering a copper element must have a radius of about 100 μm (see Table 9-2). Since the divergence angle following a spoiler is about 15 μr (see Figure 9-3), the distance from the spoiler to any copper element must be equal or larger than 7 m or 10 m for a 500 or 750-GeV beam energy, respectively. The beam radius at a spoiler, assuming it is composed of 1/4 r.l. titanium, must satisfy $\sqrt{(\sigma_x \sigma_y)} \geq 10\,\mu$m. Since there are many locations where $\sqrt{(\sigma_x \sigma_y)} < 10\,\mu$m, the single-bunch beam emittance must be enlarged for level 1 beam-line check out. This is accomplished by blowing up the beam emittance in or at the exit of the damping ring.

Level 1 objectives are achieved by placing spoilers throughout the system, so that no matter what the trajectory of the bunch, it impacts a spoiler before any other element. Figure 9-10 shows a possible single-bunch trajectory, assuming a worst-case scenario of a shorted quadrupole with an on-axis field equal the design pole-tip field followed by a quadrupole which is defocusing in the plane of the kick. In this example the distance between quadrupoles is taken to be 30 m, and the focal length of the quadrupoles taken to be 20 m. If a spoiler, with a gap of 3/5 a, is placed 10 m before each element, then assuming that the distance between quadrupoles is $d = 3/2f$, where f is the focal length of the quadrupoles, the worst case trajectory has a displacement of 9/10 a at the second quadrupole and would have a displacement of 3 a at the third quadrupole. Thus if the beam pipe between quadrupoles has a radius greater than 3 a, all beam-line elements are protected at level 1.

We take as a guideline that the aperture at the beam-line elements is 2.5 times the gap of any nearby spoiler or absorber of the collimation system. Since the largest aperture of the spoilers or absorbers in the first collimation stage is 2 mm (see Section 9.2.5), it is consistent with this guideline to assume the element aperture is 5 mm. It follows that the beam-pipe inner radius between beam-line elements must be larger than 15 mm.

Under the conditions envisaged in Figure 9-10, when a bunch passes close to a spoiler edge it can receive a wake-field kick from the spoiler. The magnitude of these kicks is calculated in Section 9.2.4. The maximum kick goes like $1/\sigma^2$ where σ is the largest axis of the beam ellipse at the spoiler. Assuming the smallest major axis within the first stage of the collimation system is 100 μm, this maximum kick is about 150 nr. Between collimation sections, the beam size is much smaller and the kick can be 100 times larger, or 15 μr.

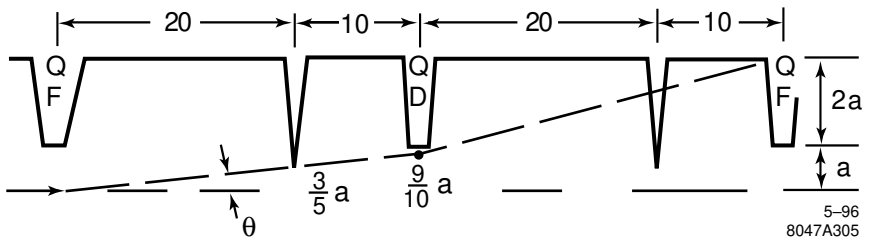

Figure 9-10. *Possible trajectories of a single bunch through a beam line as a result of completely or partially shorted quadrupole legs. Every trajectory encounters a spoiler at least 10 m before reaching the wall or another element. The quadrupoles are assumed to be spaced at 30 m and have a focal length of 20 m in this example.*

This is still much smaller that the kick angles from the quadrupoles, which in Figure 9-10 are as large as 250 mr. Thus these wakefield kicks will not compromise the level 1 protection scheme we have described.

A complete treatment of this problem would involve a study of each beam-line segment for a complete list of assumptions on failure modes. These sections on machine protection are intended as a guide to the nature of a solution, and are not intended to represent a complete study.

Since the machine-protection spoilers have apertures that are not much larger than the system spoilers and absorbers, it will be important that they are tapered to minimize the wakes. (See Section 9.4.5.) The machine-protection spoilers will look very much like the system spoilers. Since the effect of the wakes from a taper go as $\beta/g^{3/2}$, where g is the spoiler gap, only spoilers at large β will have a significant impact. The wake from the largest-β machine-protection spoiler, if constructed according to the above guidelines, would be roughly 0.3 of the wake from the main system spoiler. All machine-protection spoilers taken together can add an estimated additional 10% ($t'/t = 0.07$) to the jitter amplification budget (see Section 9.2.4). This is large enough that it should be reviewed carefully and taken into account when choosing the vertical collimation depth.

Multiple-Bunch Active Protection. For a full bunch train the machine must be turned off before the beams collide with any of the machine protection system (MPS) spoilers, since the full train would easily destroy them. Let us suppose as a worst-case scenario that a quadrupole leg is suddenly shorted. Let us suppose that the on-axis field has reached the fraction ξ of the pole tip field. This will give an angular deflection $\theta = \xi a/f$, where a is the quadrupole aperture and f is its focal length. The beam displacement downstream will be $\Delta x = \theta_x R_{12} \leq \xi R_{12} a/f$. Since the R_{12} values can be the order of $2\ 10^4$ m, for $f = 20$ m we would have $R_{12}/f = 10^3$. This means that the machine must turn off before $\xi = 10^{-3}$. Assuming the fastest rate at which the magnet can change field values is the order of 100 milli-seconds, it could change its value by 10^{-3} in 0.1 ms. Since the pulse-repetition rate is 2 ms, the magnets could change an unacceptable amount between beam pulses. Thus this error must be detected with a magnet-monitoring system, and can not be prevented by a BPM system monitoring the beam trajectory. We will assume such a magnet-monitoring system is in place.

If the magnet-monitoring system were to fail, a spoiler could be destroyed. In that case, the beam would not be sufficiently enlarged upon reaching the next beam-line element to protect it from damage. It may therefore be worthwhile to place sacrificial copper absorbers in the beam line in front of each element whose purpose would be to absorb the impact of the full beam. They would need to be replaced after a protection system failure event, but would limit damage to the system.

Property	Unit	Carbon	Copper	Ti-6Al-4V	Tungsten-Rhenium
Density	(gm/cm^3)	2	8.95	4.5	19.3
Radiation length	(cm)	18.9	1.44	3.77	0.344
Resistivity	(μohm-cm)	1000	1.7	180	5.5
Specific heat	Joules/(gm°C)	0.97	0.385	0.54	0.134
Thermal conductivity	Watt/(cm°C)	2.0/0.025	3.9	0.17	1.26
Stress limit	(°C)	2500	180	770	700
Melting point	(°C)	3600	1080	1800	3100
Vaporization temperature	(°C)	4200	3000	3260	5000

Table 9-1. *Properties of materials considered for spoilers and absorbers.*

Multiple-Bunch Passive Protection for Collimators. There are many upstream system-state changes that could cause the beam in the collimation system to impact the main collimators. Major changes will be handled by upstream machine-protection systems, but because the β functions must be large enough to collimate particles that could impact elements in the final-focus system, the change in orbit will be larger in the collimation system than in any upstream system. And since everything in the final-focus system will be in the shadow of the collimation system, the collimation system will be the most vulnerable and important to protect.

The strategy of relying on monitoring all possible state changes in upstream systems becomes a very complex and potentially unreliable task. It seems unwise to assume the collimation system can be actively protected if collimation is to occur at apertures as small as $5\,\sigma_x$. Thus we have assumed that the collimation system collimators must be passively protected. (This decision needs to be carefully reviewed as the machine protection system becomes more mature. The cost impacts are large.)

Passive protection has major consequences, and implies that whatever the material, it must be able to withstand the full impact of at least one full bunch train. In the system to be described below, this is accomplished by having a sufficiently large linear beam size at the spoiler so that it can withstand this impact. Another scenario, which uses sextupoles to blow up the beam size, is discussed in Section 9.2.8. Other schemes, such as liquid-metal collimators and Compton collimators have been proposed. Though we have discussed such systems, we have not pursued them in great depth, preferring a more conservative solution. Since the system we describe is quite expensive, thorough investigations of alternative systems are encouraged.

Properties of Collimator Materials

For the 1-TeV c.m. parameters, each beam contains an average power of 8.4 MW. If routine collimation of 1% of the beam is adopted as a system specification, the energy intercepted at any phase could be as high as 84 kW. Half of this amount could be incident on a single absorber. Devices capable of absorbing and dispersing such heat loads are most often made from copper because of its high heat conductivity, compatibility with water, reasonable size, and general adaptability. See Table 9-1 for a list of some relevant physical properties for copper and some other materials we have considered for spoilers and absorbers.

Figure 9-11 gives the energy-density deposition in three of these materials from a beam of 10^{12} particles with initial cross-sectional area given by $\sqrt{(\sigma_x \sigma_y)} = 100\,\mu$m.

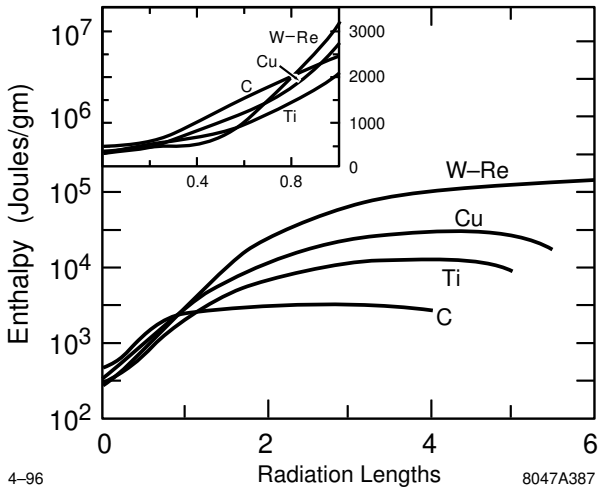

Figure 9-11. *Energy density deposition in four materials for an incident beam of* 10^{12} *particles with cross section given by* $\sqrt{(\sigma_x \sigma_y)} = 100\ \mu$m.

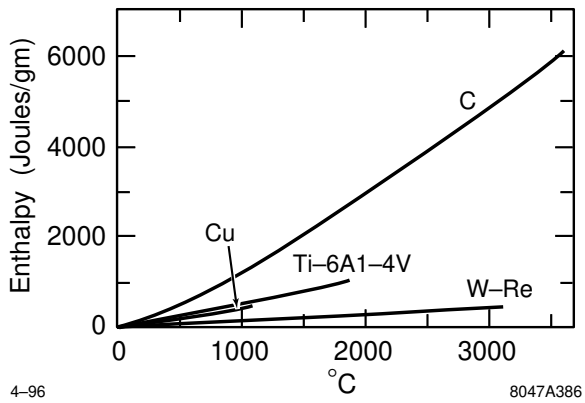

Figure 9-12. *Temperature rise versus enthalpy for four materials.*

For other beam intensities and areas the curves of Figure 9-11 may be scaled by $N/(\sigma_x \sigma_y)$ because in the distances under consideration, showers have little chance to broaden beyond the initial spot size. The multiple-scattering formula (see Eq. 9.8) yields about 30 μr at $E = 500$ GeV and $t = 1$ r.l., so the initial spot size of 30 μm would not significantly change in several radiation lengths.

Since the energy is deposited instantaneously without any opportunity for the volume to change, the energy-density deposition represents a change in enthalpy. Figure 9-12 gives the temperature rise versus enthalpy for the same four materials, incorporating the changes of specific heat with temperature.

For beams in the regime of 1-mm^2 cross section, it has been found experimentally that when a sudden local temperature rise creates local thermal stresses near the surface which exceed the tensile limit of the material, the material will probably fracture. If the temperature of copper rises suddenly by a mere 180°C, the tensile limit is exceeded (see Table 9-1). Hence for a single pulse of 10^{12} particles to give a temperature rise of less than 180°C anywhere within 2 cm of the surface, Figures 9-11 and 9-12 indicate the beam area must satisfy $\sqrt{(\sigma_x \sigma_y)} \geq 2.2$ mm. These limits for the remaining materials in Table 9-1 are shown in Table 9-2

	Fracture 2 cm from a Surface			Melt Anywhere within Volume	
Material	Enthalpy (Joules/ gm)	Incident Surface Minimum Sigma (mm)	Parallel Surface Minimum Sigma (mm)	Enthalpy (Joules/ gm)	Minimum Sigma (mm)
Carbon	3870	0.036	0.090	6000	0.072
Titanium alloy	405	0.14	0.56	960	0.36
Copper	63	1.0	2.2	470	0.82
Tungsten-rhenium	91	4.2	42.	410	2.0

Table 9-2. *Table of minimum $\sqrt{(\sigma_x\sigma_y)}$ to avoid fracture near the surface or melting of a collimator. It is assumed that there are 10^{12} particles per pulse train, and for the melt limit a particle energy of 500 GeV.*

[Walz 1973]. A beam incident on an absorber will always be within 2 cm of the collimation surface, so the temperature of the entire shower within the material must remain less than 180°C. The numbers for the incident surface apply only if the device is a dump. The fracture limit does not depend on beam energy. The melt limit is derived assuming a beam energy of 500 GeV.

To achieve 1-mm beam areas with the contemplated design emittances would require $\sqrt{(\beta_x\beta_y)} > 10^6$ m. Such β functions are impractical, and the usual strategy to achieve passive protection of collimator systems is to have a spoiler followed by an absorber [DeStaebler-Walz].

Properties of Spoilers

Spoiler-Absorber Strategy. The spoiler is fabricated from a thermally-rugged, optically-thin low-Z material so that a full shower does not develop in the material. The requirement is that the temperature rise caused by a full bunch train incident on the spoiler not lead to fracture or melting. The spoiler increases the angular divergence of the incident beam so that down-beam copper absorbers can withstand the impact of one full bunch train. Additionally the absorber must be able to continuously absorb all particles hitting the spoiler even when this is as much as 1% of the beam.

Linear modules may be used to create the large β functions to achieve the required beam sizes at the spoilers, but β enlargement has two limitations: i) creating large β functions takes a long system length, and ii) wakefield kicks from the spoilers become large compared to decreasing angular beam divergences. We show below that because of ii) there is a limit to which a beam may be collimated with a linear β enlargement.

The large β functions create chromaticity which will increase the beam emittance unless locally compensated. This suggests the use of sextupoles in $-I$ configurations in each collimation phase and each transverse plane. Energy must be collimated first, since the bends employed to generate dispersion at the sextupoles could steer an off-energy beam into the wall of the beam pipe.

Single-Train Spoiler Survival. The minimum sigma required for a 0.25 r.l. spoiler are shown in Table 9-3. The best material we have found for use as a spoiler is pyrolytic graphite. However because

Material	Minimum Sigma (μm)
Carbon	50
Copper	280
Titanium	100
Tungsten-Rhenium	225

Table 9-3. *Table of minimum $\sqrt{(\sigma_x\sigma_y)}$ to insure survival of a 1/4 r.l. spoiler for a single pulse of a beam containing 10^{12} particles.*

it is porous and has a high resistivity, it must be plated. Even thin platings will separate from the plated material or melt if the beam size is not larger than the values which are derived from considerations of the energy deposition and temperature rise curves of Figure 9-11 and 9-12.

We have concluded that plated pyrolytic carbon spoilers are a bad idea for three reasons:

i) Carbon has not been used before, and there are questions about its performance under vacuum.

ii) Though it reportedly can be plated, details and experience are scarce.

iii) The plating, even if quite thin, will indeed be damaged unless the entry spot size is large enough to prevent melting and stress damage of the plating material.

From item iii) one concludes one might as well make the spoiler from the materials considered for the plating.

The next best material is titanium. Titanium also has a rather large resistivity when compared to good conductors (the resistivity of pure titanium is 45 $\mu\Omega$-cm, and the usual titanium alloy has a resistivity of 180 $\mu\Omega$-cm, compared to 1.7 $\mu\Omega$-cm for copper), but the wake of an angle-optimized taper goes as the 1/4th power of the resistivity (see Section 9.2.4), so it is not out of the question to use titanium, especially if one uses the alloy plated with the pure titanium. TiN which has a resistivity of 22$\mu\Omega$-cm may also prove useful as a plating material. The flat section of these spoilers will be very short since we want the longest path of particles through the material to be 0.25 r.l. (< 1 cm). In fact, as can be deduced from formulae presented in Section 9.2.4, the wake from one of these titanium spoilers is identical to the wake from a 20 r.l. Cu tapered absorber for a gap of 1 mm.

Because as indicated in Table 9-3, the entry spot size required for titanium must satisfy $\sqrt{(\sigma_x\sigma_y)} \geq 100\,\mu$m, whereas for carbon the requirement was $\sqrt{(\sigma_x\sigma_y)} \geq 50\,\mu$m, the β function product $\sqrt{(\beta_x\beta_y)}$ at the spoilers must be larger by a factor of four. The collimation system length increases by about 500 m for titanium spoilers as compared to carbon.

To keep the path length within a tapered spoiler to 0.25 r.l. radiation length, we propose fabricating it from 50-μm thickness rolled titanium which is then supported by a titanium honeycomb structure. Assuming a taper angle of about 20 mr, the path length in the incoming and outgoing taper will be 2.5 mm each. The rest of the 1-cm 0.25 r.l. thickness in titanium, can be in the honeycomb support structure. The honeycomb should be oriented at 45° to the line-of-flight of the particles.

The longest path length will occur at the tip of the spoiler. If the radius of curvature at the tip is 0.5 m, then the longest path in the titanium will be 1/4 r.l. Edge scattering is not an issue for spoilers, so the radius of curvature can be this small. A sketch of such a spoiler is shown in Figure 9-24(b).

To obtain the required spot size at the spoiler we must have $\sqrt{(\beta_x\beta_y)} \geq 10^{-8}/\sqrt{(\varepsilon_x\varepsilon_y)}$. At 500-GeV c.m., the smallest possible emittance product (see Section 9.2.1) at the end of the linac is $\sqrt{(\varepsilon_x\varepsilon_y)} = 10^{-12}$, and thus we must have $\sqrt{(\beta_x\beta_y)} \geq (100)^2$ m. For 1-TeV c.m., the smallest possible emittance product, $\sqrt{(\varepsilon_x\varepsilon_y)} = 0.5\ 10^{-12}$ m-rad, implies $\sqrt{(\beta_x\beta_y)} \geq (140)^2$ m. For 1.5-TeV c.m., the smallest possible emittance product, $\sqrt{(\varepsilon_x\varepsilon_y)} = 0.33\ 10^{-11}$, implies $\sqrt{(\beta_x\beta_y)} \geq (170)^2$ m.

Spoiler Heating. Each electron passing through the spoiler will deposit an energy of $1.8\,\mathrm{MeV/cm^2}$. For the titanium alloy with a density of $4.5\,\mathrm{g/cm^3}$, this amounts to an energy deposit of 8.1 MeV/ cm per electron. Since the path length of each electron in the titanium is in fact about 1 cm, this is an energy deposit of 8.1 MeV per electron. For 10^{10} electrons per train and 180 trains per second this amounts to 2.3 W. If we assume that the spot hitting the titanium has a cross-section of a semi-circle with a radius of 100 μm, then the surface of the spoiler, if straightened into a plane would be intersected in an area of width 200 μm and length equal to $d = 1\,\mathrm{cm} + 2(100\,\mu\mathrm{m}/\theta) \approx 3\,\mathrm{cm}$, where θ is the taper angle. Heat can flow both directions toward the walls, which we will assume is a heat sink at room temperature about 5-mm away. Since the length of the spot is six times larger than the distance to the sink, we assume a simple one-dimensional parallel heat flow. Using the thermal conductivity for titanium of $0.17\,\mathrm{W/(\,cm\text{-}^\circ C)}$, we find a temperature elevation at the center of 230°C. If the 10^{10} electrons had been distributed between the two jaws, or the semi-circle had a radius of 0.2 mm, the temperature rise would be only 115°C. In any case, these are acceptable temperature rises in titanium.

Spoiler Transmission. Figure 9-13 shows an EGS simulation [Nelson 1993] of the angular distribution for several 1-GeV energy bins of particles that have passed through a 1/4 r.l. spoiler. The angular distributions are remarkably similar for all energies, peaking at about 14 μr. The solid line through the particles with energy in the 499–500-GeV bin is an expected distribution based on multiple scattering theory given by

$$\frac{dP}{d\,\Omega} = \frac{1}{2\pi\theta_0^2} e^{-\frac{\theta^2}{2\theta_0^2}} \qquad \text{with} \qquad \theta_0 = \frac{13.6}{E(\,\mathrm{MeV})}\sqrt{t}\,(1 + 0.038\,\ln[t]) \quad . \tag{9.8}$$

$\theta_0 = 14\,\mu$r is, respectively, 10^3 or 10^4 times larger than the horizontal or vertical angular beam divergence at the spoilers. Therefore in order for particles coming from the spoilers to be incident on the edges of downstream collimators, they must have $\theta \ll \theta_0$.

Figures 9-14 and 9-15 show the energy distribution of exit electrons and exit photons, respectively, from 500-GeV electrons incident on a 1/4 r.l. spoiler. The energy distribution of the photons is fit very well by a 1/k law. The energy distribution of the electron is well fit by a formula based on single-scattering which is [Rossi 1952]

$$\frac{1}{N}\,\frac{dN}{dE} = \frac{1}{E_0\Gamma\left(\frac{t}{\ln 2}\right)}\left[\ln\left(\frac{E_0}{E}\right)\right]^{\left(\frac{t}{\ln 2}-1\right)} \quad . \tag{9.9}$$

The diamonds in Figure 9-14 are calculated using this equation. Figure 9-14 has an insert which is a blow-up of the region from 450 to 500 GeV. The dots in the insert are also calculated with the theoretical formula (Eq. 9.9). For small values of $\delta = \Delta E/E$, Eq. 9.9 becomes

$$\frac{1}{N}\,\frac{dN}{d\delta} \approx \frac{1}{\Gamma(1.44t)}\,\frac{1}{\delta^{1-1.44t}} \quad . \tag{9.10}$$

With the energy and angular distribution known, and the angular distribution independent of energy, it is straightforward to initialize distributions of particles that have passed through spoilers for the purpose of tracking them through the lattice. See Section 9.2.5, Figures 9-39 and 9-41.

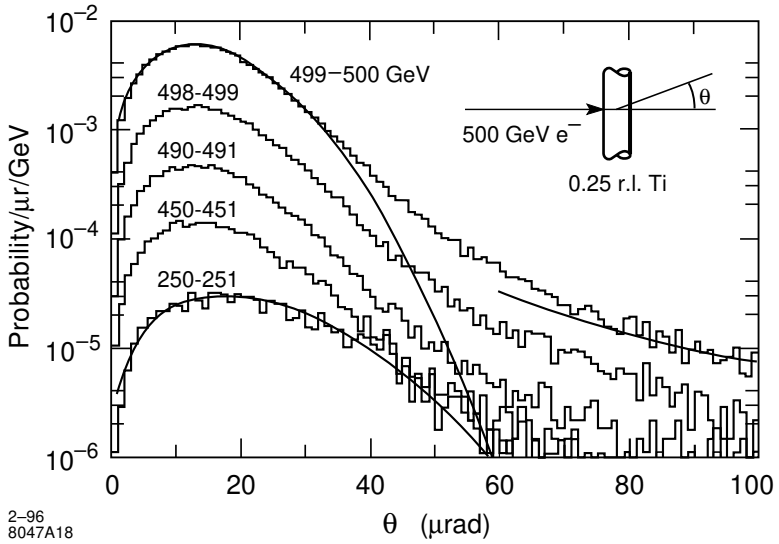

Figure 9-13. *Angular distribution of 500-GeV electrons that have passed through a 0.25 r.l. spoiler. The solid line is the theoretical prediction given in Eq. 9.8.*

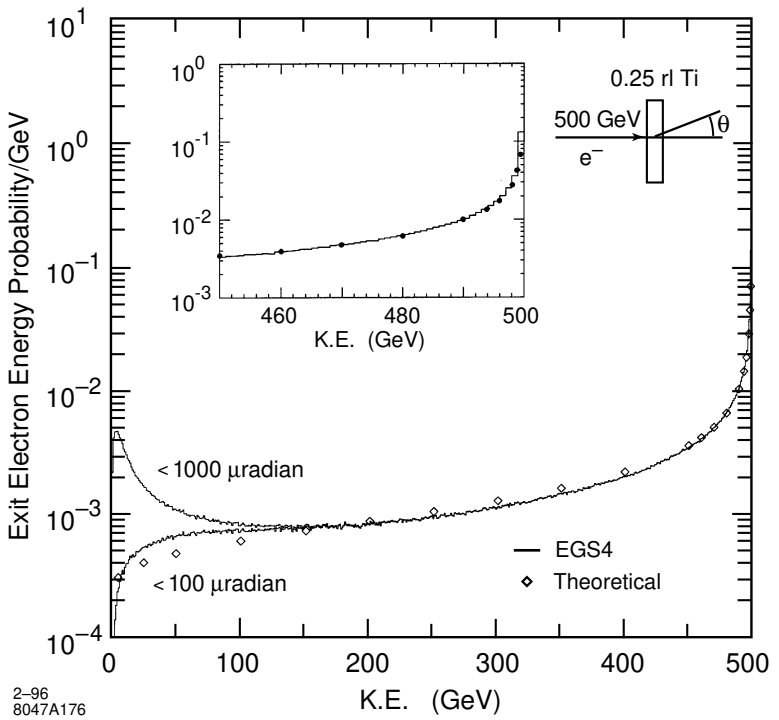

Figure 9-14. *The energy distribution of electrons from a 500-GeV beam that have passed through a 0.25 r.l. spoiler.*

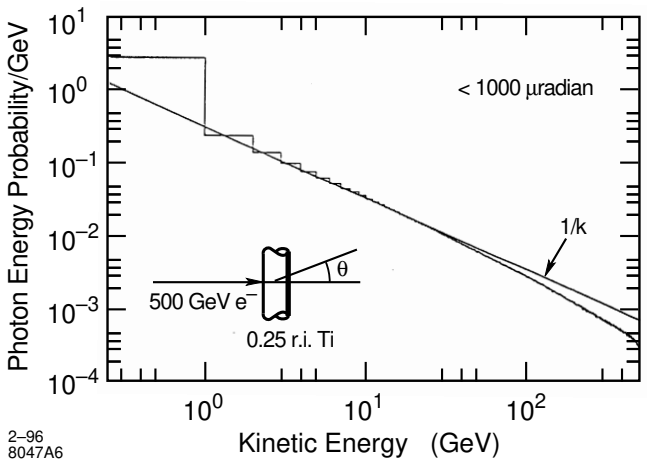

Figure 9-15. *The energy distribution of photons created by a 500-GeV beam of electrons passing through a 0.25 r.l. spoiler.*

Required Spoiler-Absorber Separation

If a beam is completely mis-steered and impacts a spoiler, the beam sigma product at the down-stream copper absorber should, according to the results of Section 9.2.2 and Table 9-2, be greater than $(2.2\,\mathrm{mm})^2$. The shape of the image on a down-beam absorbers of the particles exiting a spoiler will be an ellipse. The horizontal and vertical axes will have Gaussian distributions with rms width equal to $\theta_0 R_{12}$ and $\theta_0 R_{34}$ m, respectively. Thus we have the condition $\theta_0^2 R_{12} R_{34} \geq (2.2\,\mathrm{mm})^2$. For $\theta_0 = 14\,\mu$r we deduce $\sqrt{(R_{12}R_{34})} \geq 160\,\mathrm{m}$.

This criteria can be eased somewhat by realizing that, on the average, the beam has lost one quarter of its energy when passing through the 1/4 r.l. spoiler, so that when passing off-axis through a quadrupole between spoiler and absorber the beam is spread out. This effect is not as large as the average energy loss would indicate since the distribution is peaked at small energy loss. For example, only 25% of the particles have lost more than one-third of their energy. The exact magnitude of this effect will depend on lattice details, but if we assume that 25% of particles are not contributing to the core heating within the absorber, the condition of the last paragraph is modified to $\sqrt{(R_{12}R_{34})} \geq 140\,\mathrm{m}$.

If there is a quadrupole of inverse focal length f at a distance L_1 from the spoiler, followed by a drift of length L_2 to the copper absorber, then the $R_{12}R_{34}$ product is given by

$$R_{12}R_{34} = (L_1 + L_2)^2 - \left(\frac{L_1 L_2}{f}\right)^2 \quad . \tag{9.11}$$

Using Eq. 9.11 the current lattice does not satisfy $\sqrt{(R_{12}R_{34})} \geq 140\,\mathrm{m}$, since this lattice was designed for a lower beam intensity and a less stringent fracture criteria. A next-generation lattice under development does satisfy this condition. We will discuss future research directions in Section 9.2.9.

9.2.3 Tail Re-Population Estimates

Edge Scattering from Absorbers

Edge scattering from a spoiler is not a concern since very few particles will be incident on the edge (which, we will see below, has an effective width of about 1 μm) and, in any case, all the particles which pass through the spoiler are scattered at angles the order of 14 μr, which is similar to edge scattering. However at the absorbers, where one is hoping to clean up the beam, it is the edge scattering which re-populates the beam.

Figure 9-16 shows the results of an EGS simulation [Nelson 1993] to determine the fraction of particles that re-enter the beam as a function of distance form the edge of a flat titanium collimator edge (Note: We are expecting to use copper, but the curve can be readily scaled for all materials as shown in Figure 9-17). Only particles losing less than 4% of their energy have been counted because particles losing more energy will be collimated elsewhere. Later we present distributions with energy loss up to 20%. There is an abrupt edge in penetration at about 0.1 μm (note logarithmic scale) establishing this as the relevant edge-depth scale for titanium. To insure that the surface of an absorber with a length of a several cm be placed parallel to the beam with an accuracy of better than 0.1 μm would require an unlikely angular-placement accuracy of 1 μr. Without this placement accuracy particles in the incident beam would hit only a corner of the absorber and a larger number would be scattered back into the beam.

To avoid this effect, it has been usual to use collimators with curved surfaces [von Holtey]. Figure 9-16 also contains a curve showing the penetration probability for a curved titanium spoiler with a 100-m radius of curvature, which would require an easier 0.2-mr orientation accuracy. The transmission of the 100-m curved surface is increased by about a factor of 7, with a transmission edge at 0.7 μm. A third curve on this graph shows the edge scattering for a surface with a radius of curvature of 20 m, which would require an orientation accuracy of 1 mr. This has a transmission edge at about 3 μm, with a transmission that is a factor of 4 worse than the 100-m curvature. In the SLC collimator radii are about 10 m. The eventual flattening of these transmission curves at large offsets occurs because the EGS study was performed for a 2 r.l. absorber. If it had been thicker the curves would continue to fall.

Figure 9-17 compares the penetration probability of a curved titanium collimator with a curved carbon collimator, with the abscissa now chosen to be micro-radiation lengths (which we will denote by μrl) rather than microns. In terms of micro-radiation lengths the collimators perform identically. Since the radiation length of titanium is 3.77 cm, whereas copper's radiation length is 1.44 cm, the knee for a 100-m curved copper absorber occurs at 0.3 μm. For a 20-m curved copper absorber the knee would be at 1 μm and for a tungsten absorber it would be 0.3 μm. It is interesting to note that one can use the results of Figure 9-17 to take into account the roughness of an absorber by degrading its radiation length [DeStaebler 1994].

Figure 9-18 shows the angular distributions for edge-scattered particles re-entering the beam with energy losses of less than 20%. The angle in this distribution is the cone angle measured from the particle direction. The particles incident on the absorber were uniformly distributed from 0 to 10 μm from the edge of a Cu absorber with a radius of curvature of 100 m. Note the remarkable similarity to the angular distributions from spoiler transmission shown in Figure 9-13. The total number of particles scattered back into the beam (with energy loss less than 20%) is 0.1 times the number of particles incident on the edge per micron. In other words the number re-entering the beam is equal to the number that fall on the edge at a distance of 0.1 microns or less. The theoretical distribution of Eq. 9.8 fits this graph rather well for an rms angle of $\theta_0 = 20\,\mu$r. The effective thickness of the material (using Eq. 9.8) would be $t_{eff} \approx 0.5$ r.l.

Figure 9-19 shows the angular distribution when the angle is chosen to be the angle from a plane of the collimator surface, for the same condition as those in Figure 9-18. This distribution is rather surprising in

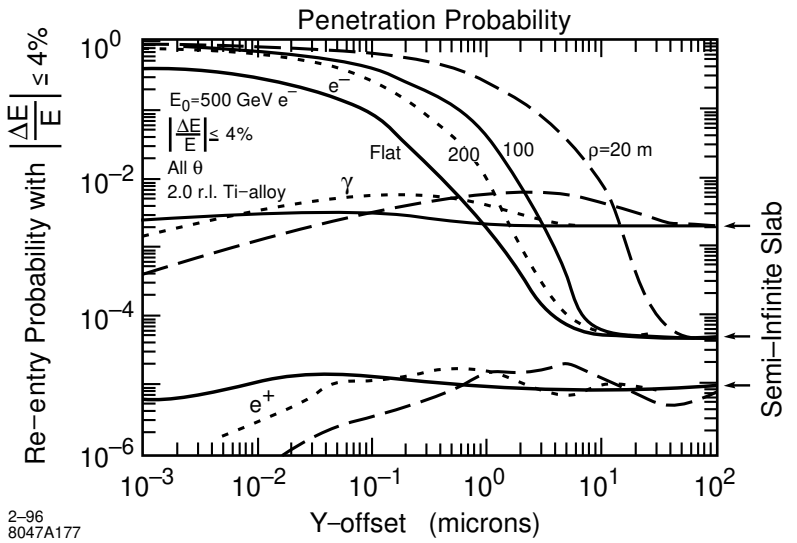

Figure 9-16. *The fraction of particles that re-enter the beam as a function of distance from the edge of a flat and curved (200-m radius of curvature) titanium scraper.*

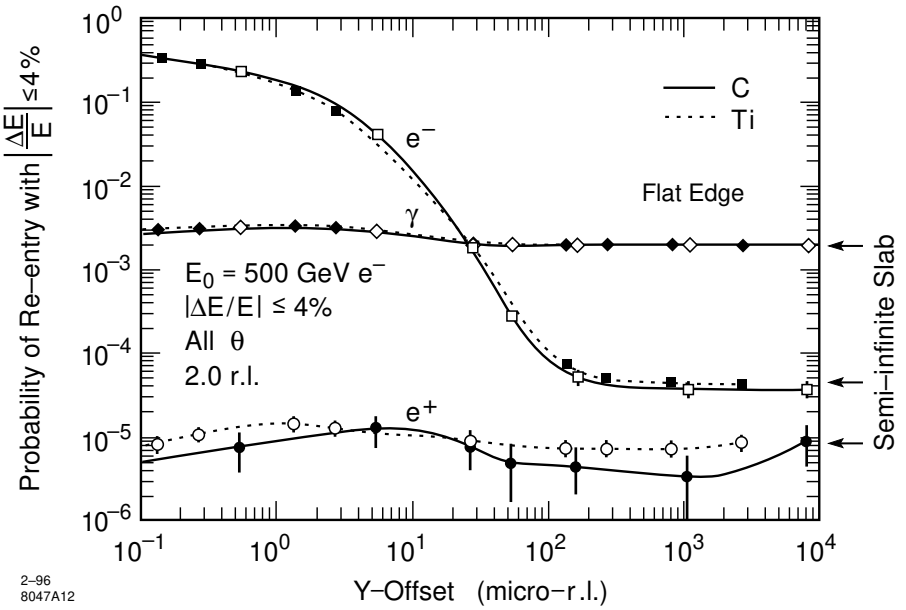

Figure 9-17. *The fraction of particles that re-enter the beam as a function of distance from the edge of a curved (200-m radius of curvature) titanium and carbon collimator. Abscissa is in micro-radiation lengths.*

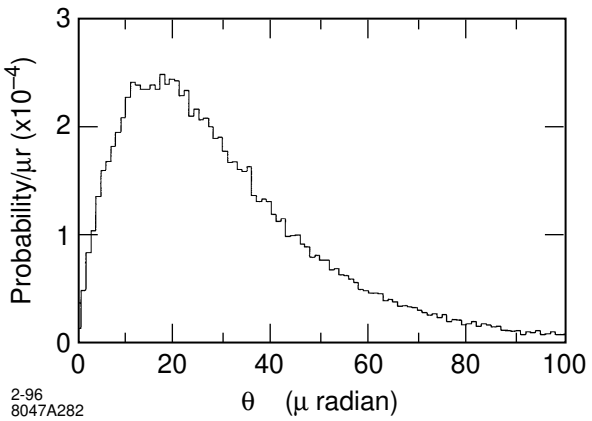

Figure 9-18. *The angular distribution of particles that re-enter the beam (with less than 20% energy loss) for a Cu collimator with a 100-m radius of curvature. The angle is taken to be the cone angle measured from the initial particle direction. The incident beam is uniformly distributed at the edge for 0 to 10 cm.*

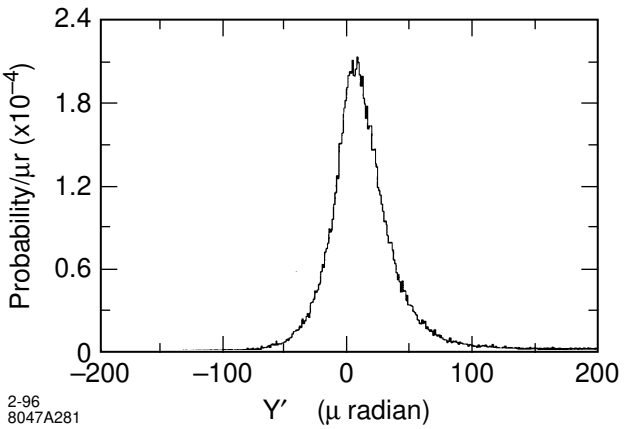

Figure 9-19. *The angular distribution of particles that re-enter the beam (with less than 20% energy loss) for a Cu collimator with a 100-m radius of curvature. The angle is taken to be the angle measured from the plane of the absorber surface. The incident beam is uniformly distributed at the edge for 0 to 10 cm.*

that the shape is still Gaussian. A quick calculation shows that the rms angle of this distribution is achieved in a distance of $20\,\mu\text{r} \times 100\,\text{m} = 2\,\text{mm}$, which is about one fifth of a radiation length for Cu, so indeed the particles can be headed back toward the plane if they are close enough to the edge that they pass through two-fifths of a radiation length or less in the collimator. We note however that there is a mean of this distribution away from the surface of about $12\,\mu\text{r}$.

Figure 9-20 shows the angular distribution when the angle is chosen to be the angle from a plane containing the line of flight of the particles and perpendicular to the surface of the absorber. If the absorber where a vertical collimator, then this angle is the horizontal angle. This distribution should be symmetric because there is no physical way to distinguish left from right.

Figure 9-21 shows the energy distribution for the particles which re-enter the beam. The particles with energy loss less than 4% is similar to Figure 9-14. The distribution for small energy losses fits a power law

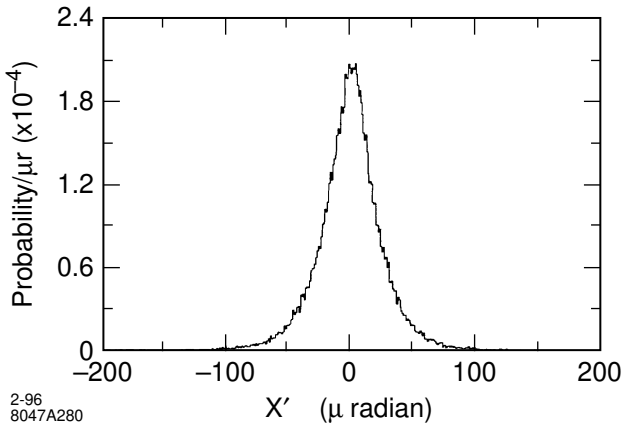

Figure 9-20. *The angular distribution of particles that re-enter the beam (with less than 20% energy loss) for a Cu collimator with a 100-m radius of curvature. The angle is taken to be the angle measured from a plane which is perpendicular to the absorber surface containing the particle line-of-flight. The incident beam is uniformly distributed at the edge for 0 to 10 cm.*

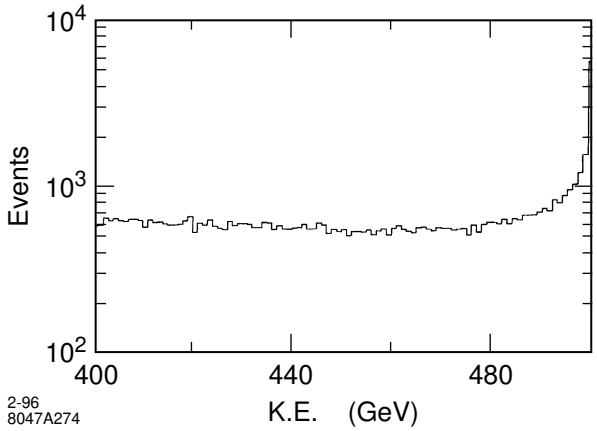

Figure 9-21. *The energy distribution of particles that re-enter the beam (with less than 20% energy loss) for a Cu collimator with a 100-m radius of curvature. The incident beam is uniformly distributed at the edge for 0 to 10 cm.*

as in Eq. 9.9 with $t_{eff} = 0.4$. For energy losses greater than 4% the distribution is quite flat. A number which will be important for us is the total number of particles that re-enter the beam. For a uniform density distribution of 1 particle per micron incident on the edge of this 100-m curved copper absorber there are a total of 0.1 particles re-entering the beam with an energy loss of less than 20%. Of this number 30% (or 0.03 particles) have an energy loss less than 4%, and 0.07 have energy loss between 4% and 20%.

Figure 9-22 shows the distribution of Figure 9-19 for four energy bins: the top 1-GeV bin (0.2%), the next 1-GeV bin, a 1-GeV bin with energy 2% below the maximum energy, and a 1-GeV bin with energy 10% below the maximum. There is a tendency for the larger energy loss particles to have a wider angular distribution. Figure 9-22b contains the same distributions as shown in Figure 9-22a but with a radius of curvature equal to 20 m rather than 100 m.

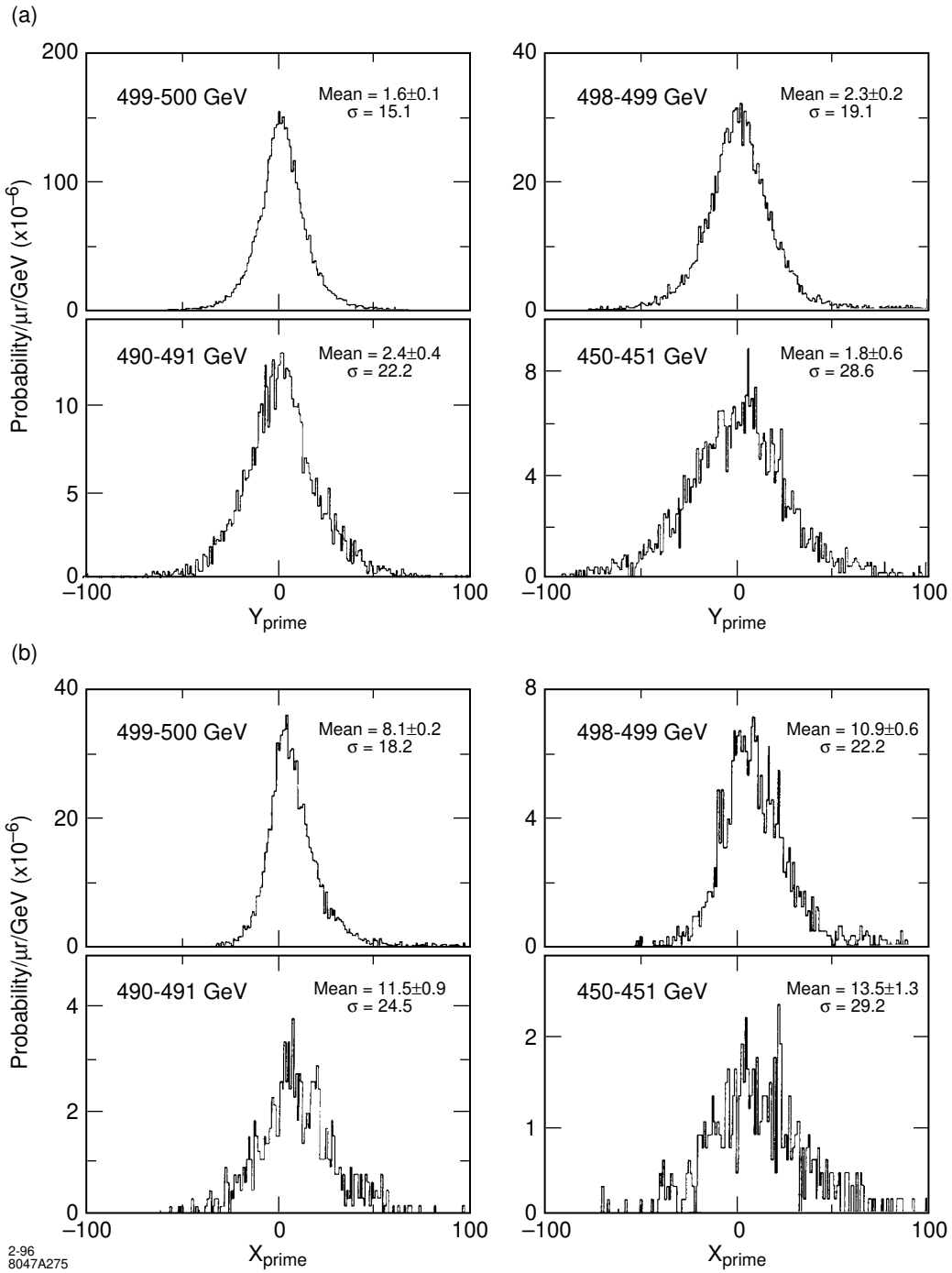

Figure 9-22. a. *The angular distribution of particles that re-enter the beam for four different energy losses for a Cu collimator with a 100-m radius of curvature. The angle is taken to be the angle measured from the plane of the absorber. The incident beam is uniformly distributed at the edge for 0 to 10 cm.* b. *The angular distribution of particles that re-enter the beam for four different energy losses for a Cu collimator with a 20-m radius of curvature. The angle is taken to be the angle measured from the plane of the absorber. The incident beam is uniformly distributed at the edge for 0 to 10 cm.*

From the distributions of this section we can arrive at the following conclusions:

- It is primarily particles very close to the edge ($\leq 0.3\,\mu$m) that are scattered back into the beam, so the distributions will not depend on the incoming particle distribution (as long as it is constant over a 1-μm distance). The total number re-entering the beam will depend only on the number of particles per μm incident on the absorber at its edge.
- The angular distributions are very similar to the angular distribution of particles transmitted through a 0.5 r.l. spoiler. The tails of the distribution will be spread due to low energy particles transmitted with larger angular kicks.
- The energy distribution, for particles with less than 4% energy loss, follows a power law distribution characterized by an effective thickness of 0.4 r.l.
- The total number of particles with energy loss less than 20% that reenter the beam is 0.1 times the number of incident particles per micron. The total number of particles with energy loss less than 4% is 0.03 times the number of incident particles per micron.

These distributions can be used to track re-scattered particles through the beam line, and the results can be used to estimate the number of particles that will be present in the particle tails as the beam travels along the beam line from the end of the linac to the IP.

Same-Section Absorbers. After the spoilers there are absorbers in the beam line to actually absorb the bulk of the energy of the tail particles. One percent of the average beam power at 1-TeV c.m. is 84 kW, so this function is substantial.

We have argued above that we must have $\sqrt{(R_{12}R_{34})} \geq 160$ m (or the equivalent when allowing for energy spread) so that the beam particles that have passed through the spoiler are spread over an area with $\sqrt{(\sigma_x\sigma_y)} \geq 2.2$ mm. This implies that at the edge of the absorber there will be a particle density of about $n_\mu \approx 10^{10}/\,\text{mm} = 10^7/\,\mu\text{m}$.

Since the first spoilers are located at a β maximum, they are adjacent to a quadrupole which is focusing in the plane being collimated. The next quadrupole is invariably defocusing in that plane, so at the absorber, which is located just prior to the second downstream quadrupole, the beam distribution will be elliptical with the major axis in the plane being collimated. In other words, the estimate of $10^7\,/\,\mu$m can be taken as an upper limit.

In the previous section it was determined that the number of particles re-scattered from a copper absorber with energy loss less than 4% is about 0.03 times the number of particles incident per micron at the edge. Using this fact and the above estimate of $n_\mu = 10^7/\,\mu$m we have the estimate for the number re-scattered (with less than 4% energy loss) as $N_{sc} \leq 0.3\,10^6$.

Of the 10^{10} tail particles coming from the spoiler only 1/2 will impact the first absorber, since 1/2 of the particles have an angle away from the collimated plane.

We have established in Section 9.2.2 that the β functions at the spoiler must satisfy $\sqrt{(\beta_x\beta_y)} \geq 100^2$ m. From this we can conclude that the rms angle ($\theta_0 \approx 14\,\mu$r) of particles emerging from the spoiler is much larger than the beam divergence. Indeed we have $\hat{\sigma}_{x'} = \sqrt{(\varepsilon_x/\beta_x)} \leq 25$ nr and $\hat{\sigma}_{y'} = \sqrt{(\varepsilon_y/\beta_y)} \leq 2.5$ nr. [Note: There can be, and often is, a large non-zero $\alpha = -1/2\; d\beta/ds$. The relevant angular spread within the beam is $\sqrt{(\varepsilon/\beta)}$, not the rms of the angular distribution in phase space, $\sigma' = \sqrt{[(1+\alpha^2)(\varepsilon/\beta)]}$. Therefore we have introduced the notation $\hat{\sigma}' = \sqrt{(\varepsilon/\beta)}$]. So $\theta_0/\hat{\sigma}_{x'} \geq 600$ and $\theta_0/\hat{\sigma}_{y'} \geq 6,000$. However, in the transport

system from the collimation system to the IP, the β functions are about 50 m, so that beam-stay-clears are also large, approximately 300 σ_x and 3,000 σ_y. Collimation must be inserted somewhere in this beam line, since 10^9 particles can not be collimated in the final focus. Though they are originally in the IP phase, because of beam-line nonlinearities, chromaticity and high order dispersion, they are sure to migrate to other phases because of their extremely large amplitudes. (See the tracking studies in Section 9.2.5. Actually only 3.5 10^8 particles reach the final focus, but of these 10^8 impact elements in the final-focus system, which is 100 times the acceptable number.)

Suppose collimation is introduced so that only 10^6 particles remain in the tails. In Section 9.2.2 we integrated the distribution to find the number of particles with angles less than some small angle θ_1 to be $\Delta N/N = 1/2(\theta_1/\theta_0)^2$. For this ratio to be 2 10^{-4}, we must have $\theta_1/\theta_0 \leq 2\ 10^{-2}$. Hence we have the estimates $\theta_1/\hat{\sigma}_{x'} \sim 10$ and $\theta_1/\hat{\sigma}_{y'} \sim 100$. We do not have to collimate to apertures that are this small, since these particles are at the IP phase, and such small amplitude particles could be transported through the IP to the dump. However we can conclude that after spoiling (and absorbing) the final-doublet phase, we must collimate the IP phase at least to an amplitude that will be transported safely through the IP. According to the dynamic aperture studies of the final-focus system (see Section 9.2.1 and Figure 9-5) this must be less than 45 σ_x and 200 σ_y.

Considerations of this section lead us to conclude that at a minimum we must either collimate the IP phase at least two times, once before the FD-phase collimation (so that the FD-phase collimation can clean up tail particles generated in the IP-phase collimation) and once after the FD-phase collimation, or collimate the FD phase twice and the IP phase once. The latter option seems attractive because the effect of gas scattering from the end of the collimation system to the FD phase of the final focus is smaller (R_{12} and R_{34} are smaller.) However the gas scattering with the IP phase last is acceptable, and it has the advantage that the last IP phase can have a larger aperture. This turns out to be important when we consider machine protection issues that arise from wake effects on badly mis-steered beams.

Though in this chapter we describe an option in which there is a second FD phase as well as a second IP phase collimation, our present opinion is that the second FD phase is unnecessary.

Next-Phase Absorbers. The R_{12} and R_{34} between phases is given by $R_{12} = \sqrt{(\beta_{x1}\beta_{x2})}$ and $R_{34} = \sqrt{(\beta_{y1}\beta_{y2})}$. Between the first IP-phase and FD-phase collimation (assuming they are collimated to the same depth), we have, from our estimates on the minimum size of the β functions, that both R_{12} and R_{34} are greater than 8 km. This implies that the size of the distribution coming from the first IP-phase spoiler will be about $R\theta_0 \approx 10$ cm when reaching the FD collimators, 100 times larger than the 1-mm size at the absorber immediately following the spoiler.

These estimates can be made more precise by writing the distribution from the spoiler as (see Eq. 9.8)

$$\frac{dN}{N} = \frac{1}{2\pi\theta_0^2} e^{-\frac{\theta_x^2}{2\theta_0^2}}\, e^{-\frac{\theta_y^2}{2\theta_0^2}}\, d\theta_x d\theta_y \quad , \tag{9.12}$$

then integrating over one of the planes to find the distribution in the other plane as

$$\frac{dN}{N} = \frac{1}{\sqrt{2\pi}\,\theta_0} e^{-\frac{\theta_x^2}{2\theta_0^2}}\, d\theta_x \quad . \tag{9.13}$$

For small θ_x the particle density is given by

$$\frac{dN}{N} = \frac{1}{\sqrt{2\pi}}\,\frac{d\theta_x}{\theta_0} \quad . \tag{9.14}$$

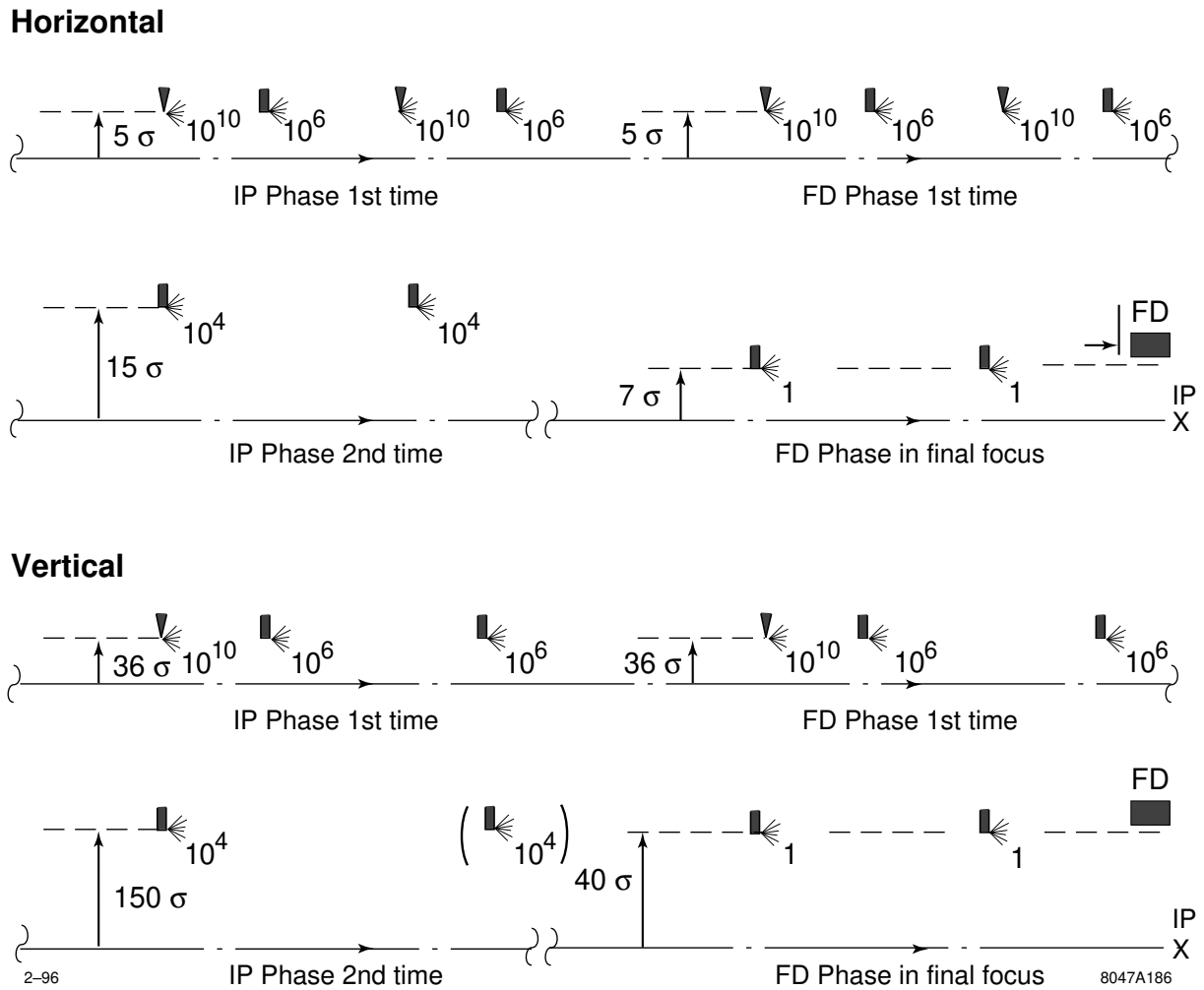

Figure 9-23. *A diagram showing the spoilers and absorbers of a collimation system that contains a single FD phase and two IP phases. The estimated particle numbers emerging from each collimator is shown.*

The distribution of Eq. 9.14 coming from the spoiler implies that the spatial distribution of particles hitting the downstream absorber edge is

$$\frac{dN}{N} = \frac{1}{\sqrt{2\pi}}\,\frac{dx}{R_{12}\theta_0} = \frac{1}{\sqrt{2\pi}}\,\frac{n_{1,x}n_{2,x}}{g_1 g_2}\,\frac{\varepsilon_x}{\theta_0}\,dx \quad . \tag{9.15}$$

We have put the expression in this form because, if the later phases are collimated at a different beam aperture, still the gaps g will be mostly between 1 or 2 mm, whereas β-functions are varied to achieve the appropriate collimator size. If the beam aperture (number of sigma) of the second stage is larger, we see that the estimate for the number of particles at the edge increases linearly with the aperture.

Figure 9-23 shows the spoilers and absorbers of a collimation system having two IP stages and a single FD stage and indicates the re-scattering that is expected at each stage.

Tail Re-population From Gas Scattering

Gas scattering must also be considered as a potential source of particles that will hit downstream collimators. The cross section for Coulomb scattering is given by

$$d\sigma = \left(\frac{e^2 Z}{2\pi\varepsilon_0 c}\right)^2 d\phi \frac{dq}{q^3} \quad . \tag{9.16}$$

Depending on the nature of the downstream aperture, one can find an expression for the minimum transverse momentum $q_{\min}$ which an electron must receive in order to impact that aperture. If the aperture is round the expression is given by

$$\frac{q_{\min}(s,\phi)}{p_0}\left(R_{12}(s)^2\cos^2\phi + R_{34}(s)^2\sin^2\phi\right)^{\frac{1}{2}} = a \tag{9.17}$$

where p_0 is the beam momentum, a is the aperture radius, and ϕ is the azimuthal angle at which the particle is scattered. If the aperture is a pair of horizontal planes, with half gap g, the expression for $q_{\min}$ will be

$$\frac{q_{\min}(s,\phi)}{p_0} R_{12}(s)\cos\phi = g \quad . \tag{9.18}$$

The cross section for a scattered particle to hit the final doublet is

$$\begin{aligned}
\frac{d\sigma}{d\phi} &= \left(\frac{e^2 Z}{2\pi\varepsilon_0 c}\right)^2 \int_{q_{\min}(s,\phi)}^{\infty} \frac{dq}{q^3} = \frac{1}{2}\left(\frac{e^2 Z}{2\pi\varepsilon_0 c}\right)^2 \frac{1}{q_{\min}^2(s,\phi)} \\
&= 2\left(\frac{r_e Z}{\gamma a}\right)^2 \left(R_{12}(s)^2\cos^2\phi + R_{34}(s)^2\sin^2\phi\right) \quad , \quad \text{circular aperture, or} \\
&= 2\left(\frac{r_e Z}{\gamma g}\right)^2 R_{12}(s)^2\cos^2\phi \quad \text{for a flat aperture.}
\end{aligned} \tag{9.19}$$

This may now be integrated over ϕ. The probability of a scatter in distance ds is given by $\rho\sigma ds$. Thus the number scattered along the beam line which will exceed the aperture limit is given by

$$\begin{aligned}
\frac{\Delta N}{N} &= 2\pi\rho_N\left(\frac{r_e Z}{\gamma a}\right)^2 \int ds \left(R_{12}(s)^2 + R_{34}(s)^2\right) \quad , \quad \text{or} \\
&= 2\pi\rho_N\left(\frac{r_e Z}{\gamma g}\right)^2 \int ds R_{12}(s)^2 \quad .
\end{aligned} \tag{9.20}$$

If we assume that the major composition of gas within the beam pipe is a diatomic molecule like N_2, the number of nuclei per unit volume is approximately $\rho_N \approx 6\ 10^{22} P_G m^{-3}$ where P_G is the pressure measured in Torr. If we assume a value of $Z = 7$ and a gas pressure of 10^{-8} Torr, these equations become (for 1-TeV-c.m. energies)

$$\begin{aligned}
\frac{\Delta N}{N} &= 1.5\ 10^{-24}\frac{1}{a^2}\int ds \left(R_{12}(s)^2 + R_{34}(s)^2\right) \quad , \quad \text{or} \\
&= 1.5\ 10^{-24}\frac{1}{g^2}\int ds R_{12}(s)^2 \quad .
\end{aligned} \tag{9.21}$$

Also of interest is the number density at the edge. This is given by

$$\begin{aligned} \frac{dN}{da} &= 3\,10^{-12}\frac{1}{a^3}\int ds\left(R_{12}(s)^2+R_{34}(s)^2\right) \quad , \qquad \text{or} \\ \frac{dN}{dg} &= 3\,10^{-12}\frac{1}{g^3}\int ds R_{12}(s)^2 \end{aligned} \tag{9.22}$$

where we have set $N = 10^{12}$.

First we can make an estimate of how many particles will hit the absorber in the first FD phase from gas scattered particles in the first IP phase. Since the two beam-line sections are separated by $\pi/2$ in phase we can set $R_{12}^2(s) = \beta_{x1}(s)\beta_{x2}$. We get the estimate

$$\frac{dN}{dg} = 3\,10^{-12}\,\frac{\beta_{x,2}}{g^3}\int ds\beta_{x,1}(s) = 3\,10^{-12}\,\frac{\beta_{x,2}}{g^3}L\,\langle\beta_{x,1}\rangle \tag{9.23}$$

where L is the length of the first phase collimation section. If we take $L = 400\,\text{m}$ (see the lattices in Section 9.2.5), $<\beta>= 1/2\,\beta_{\max}$, and $g = 2\,\text{mm}$, we get $dN/dg = 5\,10^6$. The number per micron would be $n_\mu = 5$, and hence negligible. The total number hitting the collimator is estimated to be $N \approx 2\,10^4$. These numbers are small compared to other backgrounds within the first stage of the collimation system.

The same approach can be used to find an estimate for number of particles that are gas-scattered in the last IP phase of the collimation system (assuming it is an IP phase) that are incident on the collimators of the final-focus system. The $\beta_{x2} = 4\,10^4$ is larger by a factor of about 2, but g is larger by a factor of about 3. Thus estimates are $dN/dg \approx 3\,10^6 (n_\mu = 3)$ and $N \approx 6\,10^3$. These numbers are now not negligible, but they are safely within the number of particles that can be collimated there.

There are two other important estimates to make: the number of tail particles gas scattered in the entire beam line from the collimation system to the final-focus system, and the number of particles incident on the final doublet from particles that are gas scattered within the final telescope of the final-focus system.

To estimate the number from the beam line, we will assume the value of $\sin^2\phi_{12}(s)$ can be taken to be 1/2. This should be true since the phase advances of these beam-line modules are not locked into the final-focus system phases. We can thus use the same formula derived for the IP-to-FD phase multiplying by a factor of 1/2. Now $L = 1.3\,\text{km}$, and $<\beta_{1,max}>\approx 40\,\text{m}$. Taking $\beta_{x,2} = 4\,10^4$ and $g = 4\,\text{mm}$, we get the estimates $dN/dg \approx 5\,10^4 (n_\mu = .05)$ and $N \approx 10^2$. These are much smaller than the particles from the last collimation section.

Within the final telescope it is important to use the correct R_{12} function and the round aperture formula. The numbers are still quite acceptable. See Chapter 11, Eq. 11.68.

9.2.4 Wakefield Considerations

Wakefields of Tapered Collimators

The wakefield kick from a spoiler or absorber consists of a geometrical part and a resistive-wall part. To reduce the geometrical wakefield, the spoiler and/or absorber may be tapered as shown in Figure 9-24.

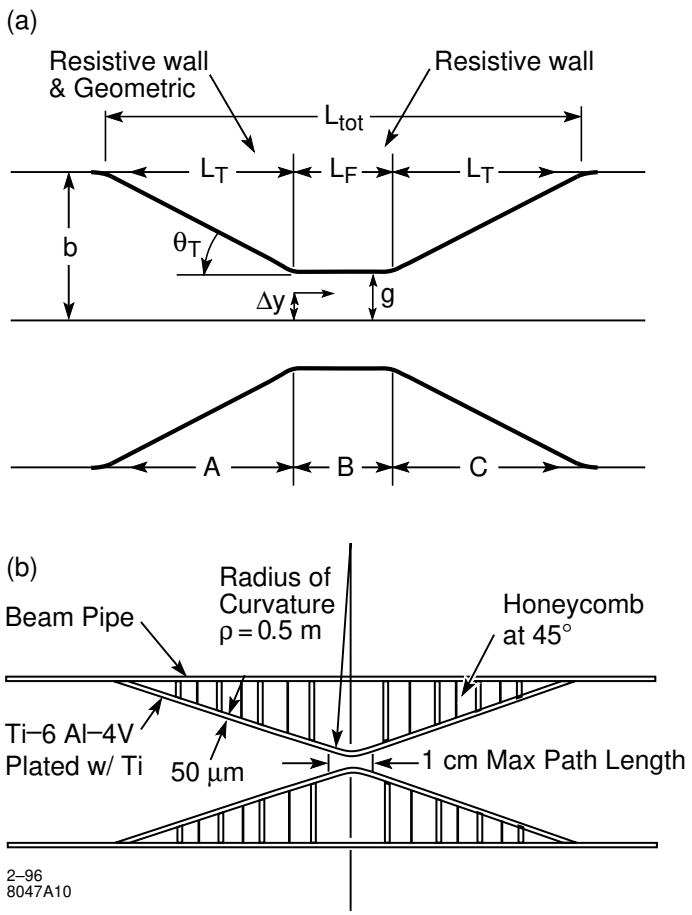

Figure 9-24. *a. Cross-sectional profile of a tapered absorber. b. Cross-sectional profile of a tapered spoiler.*

The geometric wake from a tapered spoiler was first studied by K. Yokoya for a cylindrical beam pipe geometry [Yokoya 1988]. The resulting formula may be written as

$$\Delta y'^{T}_{G} = A\,[2 I_1 y_0] \quad \text{where} \quad A = \frac{N r_e}{\gamma \sigma_z} f_G(\tau)\,, \quad I_1 = \int \frac{b'^2}{b^2} ds\,, \quad \tau = \frac{z}{\sigma_z} \quad , \quad \text{and} \quad f_G(\tau) = \frac{1}{\sqrt{2\pi}} e^{-\frac{\tau^2}{2}} \quad . \tag{9.24}$$

Here $b(s)$ is the half-height of the beam pipe as a function of longitudinal position s. y_0 is the displacement of the source particle from the axis. There is no dependence on the position of the test particle for small displacements. The integral I_1 is especially easy to evaluate for a constant b', by taking one factor of b' outside the integral and writing $b'ds = db$ inside the integral. The integral evaluates to $(1/g - 1/b)$, where b is the maximum half-height and g is the collimator half-gap.

The geometric wake for a parallel-plate taper has been studied by G. Stupakov [Stupakov 1996]. The initial result, which is the formula used in many of the computations in this chapter, was

$$\Delta y'^{T}_{G} = A\,[1.85\; I_1 y_0 + 1.43\; I_1 y] \tag{9.25}$$

where there is now a dependence on y, the position of the test particle. This term is called the quadrupole wake which is present even for on-axis $y_0 = 0$ source particles. For $y = y_0$ this wake is 64% larger than the cylindrical geometry wake.

The current theoretical result, which was deduced by Stupakov as this text was going to press, may be written

$$\Delta y'^T_G = A\left[(2\pi\, w\, I_2 - 2\, I_1)\, y_0 + 2\, I_1\, y\right] \quad \text{where} \quad I_2 = \int \frac{b'^2}{b^3} ds \quad . \tag{9.26}$$

Now a dependence on w, the width of the collimator, is present. For a constant b', the integral I_2 evaluates to $1/2(1/g^2 - 1/b^2)$. For $y = y_0$ the I_1 terms cancel, and the dependence on gap width changes to $1/g^2$. The resulting wake is larger than the one used in this chapter by a factor of $(\pi/3.82)(w/g)$, which for $w = 5g$ is about 4.

Since the result of the last paragraph is new and requires confirmation, we have decided to use a modified cylindrical collimator wake in the following sections. For the near-wall and quadrupole-wake effects we will use the original parallel-plate results. This is unfinished and somewhat unsatisfactory, but is a compromise which allows us to illustrate the range of physical effects that are important.

Evaluating the integral I_1 and inserting $b' = (b-g)/L_T$ where L_T is the length of the taper, the taper will have the wake equation

$$\Delta y'^T_G(\tau) = \alpha_G \frac{N r_e}{\gamma \sigma_z} \frac{2(b-g)^2}{bgL_T} f_G(\tau) \Delta y \qquad \text{where}$$
$$\tau = \frac{z}{\sigma_z} \qquad \text{and} \qquad f_G(\tau) = \frac{1}{\sqrt{2\pi}} e^{-\frac{\tau^2}{2}} \quad . \tag{9.27}$$

α_G is a geometric factor that is unity for a cylindrical beam pipe (Eq. 9.24), equal $3.28/2 = 1.64$ for parallel plate geometry if Eq. 9.25 is valid, and under conditions where w was assumed to scale with g (large g case), would be $(\pi/2)\, w/g$ where Eq. 9.26 holds.

To get the resistive-wall kick from a taper we have integrated parallel-plate resistive-wall wake formula [Chao 1992].

$$\Delta y'^T_R(\tau) \;=\; \alpha_R \frac{N r_e}{\gamma \sigma_z} \frac{2}{r^3(s)} ds \sqrt{\lambda \sigma_z} f_R(\tau) \Delta y \qquad \text{where}$$
$$\tau = \frac{z}{\sigma_z} \qquad \text{and} \qquad f_R(\tau) = \frac{\sqrt{2}}{\pi} \int_0^\infty \frac{d\tau'}{\sqrt{\tau'}} e^{-\frac{(\tau'+\tau)^2}{2}} \quad . \tag{9.28}$$

The result is

$$\Delta y'^T_R(\tau) = \alpha_R \frac{N r_e}{\gamma \sigma_z} \frac{(b+g)}{b^2 g^2} L_T \sqrt{\lambda \sigma_z} f_R(\tau) \Delta y \quad . \tag{9.29}$$

The function f_R is shown in Figure 9-25. α_R is a geometric factor that is 1 for a cylindrical beam pipe and equals $\pi^2/8$ for parallel plate geometry. Note: This formula is also somewhat uncertain, and SLC measurements are indicating a larger wake [SLC].

$\lambda \equiv \rho/(120\pi)$ is referred to as the resistive depth (ρ is the resistivity in Ω-m). This formula can be taken as valid over the entire bunch if $\sqrt{(\sigma_z \lambda)} \ll g \ll (\sigma_z/\lambda)\sqrt{(\sigma_z \lambda)}$. These inequalities are true for all combinations of λ, σ_z, and g we will consider. For Cu, with $\lambda = 0.045$ nm, this translates to $.08\,\mu\text{m} \ll g \ll 0.2$ m, and for Ti, with $\lambda = 1.2$ nm, this becomes $4\,\mu\text{m} \ll g \ll 0.4$ m.

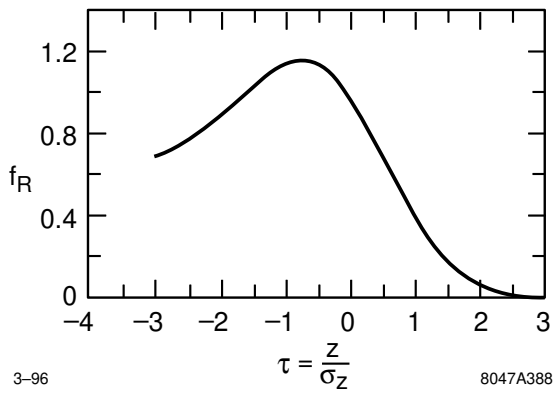

Figure 9-25. *The resistive-wall wake strength as a function of longitudinal position within the bunch.*

We will need averages over the bunch length of f_R, f_R^2, f_G, f_G^2, and $f_G f_R$, whereby the average of any function, h, over the bunch length we mean

$$\langle h \rangle \equiv \frac{1}{\sqrt{2\pi}} \int_{-\infty}^{\infty} d\tau' \; e^{-\frac{\tau'^2}{2}} h(\tau') \tag{9.30}$$

These averages are $< f_G >= .282$, $< f_G^2 >= .092$, $\sigma_{f_G} = .111$, $< f_R >= .816$, $< f_R^2 >= .774$, $\sigma_{f_R} = .330$, and $< f_G f_R >= .25$ where by σ_h is meant: $\sigma_h \equiv \sqrt{(< h^2 > - < h >^2)}$. Note that both for f_G and f_R, $\sigma_f / < f > \approx 0.4$. This suggests that emittance growth effects will be smaller than centroid change effects. We also note for later reference that for both f_R and f_G the maximum values $f_{\max} = 1.4 < f >$.

To find the taper length L_T for which the total kick to the centroid is a minimum we must find the minimum of

$$\frac{A \langle f_G \rangle}{L_T} + B \langle f_R \rangle L_T \tag{9.31}$$

which occurs at $L_T = \sqrt{(A < f_G > /(B < f_R >))} = .58\sqrt{(A/B)}$ where both kicks are equal, and the total centroid kick is $< \Delta y'^T >= 2\sqrt{(< f_G >< f_R > AB)} \approx \sqrt{(AB)}$. Plugging in the expressions for A and B we have a minimum kick equal to (now for both incoming and outgoing taper)

$$\begin{aligned} \Delta y'^T &= 2\sqrt{\alpha_G \alpha_R}\, \frac{N r_e}{\gamma \sigma_z} \left[2 \langle f_G \rangle \langle f_R \rangle \frac{(b^2 - g^2)(b-g)}{b^3} \right]^{\frac{1}{2}} \left(\frac{\lambda \sigma_z}{g^6} \right)^{\frac{1}{4}} \Delta y \\ &\approx 2\sqrt{2}\, \sqrt{\alpha_G \alpha_R}\, \frac{N r_e}{\gamma \sigma_z} \left(\frac{\lambda \sigma_z}{g^6} \right)^{\frac{1}{4}} \Delta y \qquad \text{for} \qquad g \ll b \end{aligned} \tag{9.32}$$

and

$$\begin{aligned} L_T^{opt} &= (b-g) \left(\frac{2b \langle f_G \rangle}{(b+g) \langle f_R \rangle} \right)^{\frac{1}{2}} \left(\frac{g^2}{\lambda \sigma_z} \right)^{\frac{1}{4}} \sqrt{\frac{\alpha_G}{\alpha_R}} \\ &\approx 0.8(b-g) \left(\frac{g^2}{\lambda \sigma_z} \right)^{\frac{1}{4}} \sqrt{\frac{\alpha_G}{\alpha_R}} \qquad \text{for} \qquad g \ll b \quad . \end{aligned} \tag{9.33}$$

For the usual case where $g \ll b$ the optimum taper angle is given by

$$\Theta_T^{opt} \approx 1.1 \left(\frac{\lambda \sigma_z}{g^2} \right)^{\frac{1}{4}} \sqrt{\frac{\alpha_G}{\alpha_R}} \tag{9.34}$$

Taking $g = 1\,\mathrm{mm}$, $\sigma_z = 100\,\mu\mathrm{m}$, $\alpha_G = \alpha_R$ and $\lambda = \{0.045, 0.15, 1.2\}\,\mathrm{nm}$ for {Cu, W, Ti} respectively yields $\Theta_T^{opt} = \{9, 12, 21\}\,\mathrm{mr}$. For $b = 5\,\mathrm{mm}$ $L_T^{opt} = \{55, 42, 24\}\,\mathrm{cm}$. The tungsten-rhenium alloy referred to here can be plated with copper to improve its surface conductivity. The titanium, because it will be used as a spoiler, cannot be plated, except with a material that has survival characteristics as good or better than itself.

The emittance of the beam is also enlarged by the kicks. Since these kicks are in one direction in phase space, they cause the normalized phase-space distribution to depart from a circle into something resembling an ellipse. We will introduce the notation that the IP- and FD-phase axis lengths of this ellipse are $r_{y,\mathrm{IP}}$ and $r_{y,\mathrm{FD}}$. For kicks that are small compared to the original radius of this distribution we would have the estimate for the final radius: $\tilde{r}_{y,\mathrm{IP}}^2 = r_{y,\mathrm{IP}}^2 + \left\langle \Delta r_{y,\mathrm{IP}}{}^2 \right\rangle$, or equivalently

$$\tilde{r}_{y,\mathrm{IP}} \approx r_{y,\mathrm{IP}} \left(1 + \frac{1}{2} \frac{\left\langle \Delta r_{y,\mathrm{IP}}{}^2 \right\rangle}{r_{y,\mathrm{IP}}^2} \right) \quad . \tag{9.35}$$

The ratio in the parenthesis way be determined from

$$\frac{\left\langle \Delta r_{y,\mathrm{IP}}{}^2 \right\rangle}{r_{y,\mathrm{IP}}^2} = \frac{\left\langle \Delta y'^2 \right\rangle - \left\langle \Delta y' \right\rangle^2}{\hat{\sigma}_{y'}^2} \quad . \tag{9.36}$$

Hence to minimize the emittance growth we must minimize

$$\begin{aligned} &\left\langle \left(\frac{A f_G}{L_T} + B f_R L_T \right)^2 \right\rangle - \left\langle \left(\frac{A f_G}{L_T} + B f_R L_T \right) \right\rangle^2 \\ &= \frac{A^2 \sigma_{fG}^2}{L_T^2} + B^2 \sigma_{fR}^2 L_T^2 + 2AB \left(\langle f_G f_R \rangle - \langle f_G \rangle \langle f_R \rangle \right) \end{aligned} \tag{9.37}$$

The minimum emittance growth occurs at $L_T = \sqrt{(A\sigma_{fG}/(B\sigma_{fR}))} \approx 0.53\sqrt{(A/B)}$, (compare $0.58\sqrt{(A/B)}$ for the minimum centroid kick), and the emittance growth at this minimum is given by

$$\frac{\left\langle \Delta r_{y,\mathrm{IP}}^2 \right\rangle}{r_{y,\mathrm{IP}}^2} = 2 \left(\sigma_{f_g} \sigma_{f_R} + \langle f_G f_R \rangle - \langle f_G \rangle \langle f_R \rangle \right) \frac{AB}{\sigma_{y'}^2} = 0.11 \frac{AB}{\sigma_{y'}^2} \approx 0.11 \frac{\langle \Delta y_T' \rangle^2}{\sigma_{y'}^2} \quad . \tag{9.38}$$

For a resistive-wall kick or geometric kick alone we would have

$$\frac{\left\langle \Delta r_{y,\mathrm{IP}}{}^2 \right\rangle}{r_{y,\mathrm{IP}}^2} = \frac{\sigma_{\Delta y_R'}^2}{\sigma_{y'}^2} = 0.16 \frac{\langle \Delta y_T' \rangle^2}{\sigma_{y'}^2} \quad . \tag{9.39}$$

Since $\frac{\Delta\sigma_{\mathrm{IP}}}{\sigma_{\mathrm{IP}}} = \frac{\Delta r_{y,\mathrm{IP}}}{r_{y,\mathrm{IP}}} = \frac{1}{2} \frac{\left\langle \Delta r_{y,\mathrm{IP}}^2 \right\rangle}{r_{y,\mathrm{IP}}^2}$, the luminosity loss from the taper emittance growth is

$$\frac{\Delta L}{L} = -\frac{\Delta\sigma_{\mathrm{IP}}}{\sigma_{\mathrm{IP}}} = 0.055 \frac{\langle \Delta y_T' \rangle^2}{\sigma_{y'}^2} \quad . \tag{9.40}$$

The luminosity loss from centroid kicks can be derived from the expression $(\Delta y_R - \Delta y_L)^2/(4\sigma^2)$. Taking the right and left kick to be statistically independent, this becomes $\Delta y_R^2/(2\sigma^2)$. Disruption, even at 1/2 design current, allows for twice the mis-steering for the same luminosity loss. Hence with disruption we have the estimate:

$$\frac{\Delta L}{L} = -\frac{1}{8} \frac{\Delta y_R^2}{\sigma_{\mathrm{IP}}^2} = -\frac{1}{8} \frac{\langle \Delta y_T' \rangle^2}{\sigma_{y'}^2} \quad . \tag{9.41}$$

We see that for an optimized taper the emittance growth effect is 2.3 times smaller than the centroid kick effect, even when including disruption. In the horizontal plane, without disruption, it is 9.2 times smaller.

We are expecting an incoming vertical jitter from the linac of 0.2 σ. If we assume an $\frac{\langle \Delta y'_T \rangle}{\sigma_{y'}} \leq 0.7$ for the kicks from both the collimation and final-focus system, the luminosity loss from additional jitter would be about $(1/8)[(0.2)(0.7)]^2 = 0.25\%$, and the luminosity loss due to emittance growth would be 0.1%.

System Wake Equation

If the beam-centroid displacement Δy is due to beam jitter, then the wakefield $\Delta y'$ contributes to beam jitter 90° out of phase from and proportional to the source. The kick from the collimator 'i' will give a kick to the beam, which measured in terms of $\hat{\sigma}_{y'} = \sqrt{\varepsilon_y/\beta_y}$ is

$$t'_i = \frac{\Delta y_i'^T + \Delta y_i'^F}{\hat{\sigma}_{y',i}} = 2\alpha_R \frac{N r_e}{\gamma \sigma_z} \left[\sqrt{2} \frac{(\lambda_i \sigma_z)^{1/4}}{g_i^{3/2}} \sqrt{\frac{\alpha_G}{\alpha_R}} + \langle f_R \rangle \frac{L_{F,i} \, (\lambda_i \sigma_z)^{1/2}}{g_i^3} \right] \frac{\Delta y_i}{\hat{\sigma}_{y',i}} \quad . \tag{9.42}$$

If we write the incoming jitter $\Delta y_i = t_i \sigma_{y,i}$ and use $\beta_{y,i} = \sigma_{y,i}/\hat{\sigma}_{y',i}$ then the above equation contains a dependence on the β function at the collimator, the collimator gap, and two parameters which depend on the material and dimensions of the collimator, λ and L_F. The β function can be written in terms of the gap and the number of σ collimated, through $\beta_y = g^2/(\varepsilon_y n_y^2)$, to obtain

$$\frac{t'_i}{t_i} = 2\alpha_R \frac{N r_e}{\varepsilon_y^N \sigma_z} \left[\sqrt{2} \, g_i^{1/2} (\lambda_i \sigma_z)^{1/4} \sqrt{\frac{\alpha_G}{\alpha_R}} + \langle f_R \rangle \frac{L_{F,i} \, (\lambda_i \sigma_z)^{1/2}}{g_i} \right] \frac{1}{n_{y,i}^2} \quad . \tag{9.43}$$

There is an optimal gap, $g = g_0$, which minimizes the bracket in the above equation,

$$g_{0i} = 0.54 \, (\lambda_i \sigma_z)^{1/6} \, L_{F,i}^{2/3} \, (\alpha_R/\alpha_G)^{1/3} \tag{9.44}$$

which depends only on σ_z and the collimator parameters. If the gap is taken to be optimal, then $t'_i = (\overline{n}_i/n_i)^2 t_i$ where $\overline{n}_i$ is equal to

$$\overline{n}_{y,i}^2 \equiv 2\alpha_R \frac{N r_e}{\varepsilon_y^N \sigma_z} [\ldots]_{opt} \approx 3.2 \frac{N r_e}{\varepsilon_y^N} \frac{(\lambda_i L_{F,i})^{1/3}}{\sigma_z^{2/3}} \alpha_G^{1/3} \alpha_R^{2/3} \tag{9.45}$$

When the collimation aperture is set to $n_i = \overline{n}_i$ and g is chosen optimally, then the ratio $t'/t = 1$. In terms of the parameters g_{0i} and $\overline{n}_i$, Eq. 9.43 can be written

$$\frac{t'_i}{t_i} = \frac{\overline{n}_{y,i}^2}{n_{y,i}^2} \left[\frac{2}{3} \sqrt{\frac{g_i}{g_{oi}}} + \frac{1}{3} \left(\frac{g_{oi}}{g_i} \right) \right] = \frac{\overline{n}_{y,i}^2}{n_{y,i}^2} \phi_i \tag{9.46}$$

For convenience we have introduced the function

$$\phi(x) \equiv \frac{1}{3} \left(2\sqrt{x} + \frac{1}{x} \right) \quad \text{and defined} \quad \phi_i \equiv \phi \left(\frac{g}{g_{0i}} \right) \quad . \tag{9.47}$$

It has the values $\phi(1) = 1$, $\phi(2) = 1.1$, $\phi(4) = 1.42$, $\phi(8) = 1.93$. We see that g can be a factor of 8 larger than g_0 before the kick from a collimator has doubled.

Equation 9.46 has the advantage that the parameters have an intuitive meaning and in addition the dependence on g will be quite weak if it is chosen near g_{0i}. The optimal gaps g_{0i} and the $\overline{n}_i$ parameters

Attribute	Symbol	Titanium Plated Titanium Alloy Spoiler (1/4 r.l.)	Copper Absorber (20 r.l.)	Copper-plated Tungsten-Rhenium Absorber (20 r.l.)
Resistive Depth	$\lambda = \rho/(120\pi)$ (nm)	1.2	0.045	0.045
Flat length	L_F (cm)	1.0	30.	7.0
Optimum gap	g_o (mm)	0.23	1.3	0.5
Horizontal $\overline{n}$	$\overline{n}_x$	1.42	1.45	1.14
Vertical $\overline{n}$	$\overline{n}_y$	11.2	11.5	9.0

Table 9-4. *Important parameters for spoilers and absorbers. The parameter depends on the emittance, bunch length and particle number of a bunch. This table uses the values* $\alpha_R = \alpha_G = \pi 2/8$. π *varies as* $\alpha_G^{1/6}$.

for the three types of collimators we will use are shown in Table 9-4. For the titanium spoiler, we take the length of the curved section at its apex ($L_F = 1$ cm) to be the appropriate length of the flat section.

The half-gaps, g, cannot be too large, or else the apertures of nearby beam-line elements become uncomfortably large, and they can not be too small, or else the collimator becomes impossible to control, align and adjust. It is remarkable that the optimum g, depending only on properties of materials and the bunch length, are actually reasonable values for collimator gaps.

Now we can write the equation for a system of collimators. The kicks from each collimator at any particular phase will add monotonically. If we assume that throughout the system the jitter in the phase being collimated does not increase appreciably, then setting $t' = \Sigma t'_i$ and all $t_i = t$ we have the result

$$\frac{t^i}{t} = \sum_i \left(\frac{t'_i}{t_i}\right) = \sum_i \left(\frac{\overline{n}_i}{n_{y,i}}\right)^2 \phi_i \quad , \tag{9.48}$$

where $n_{y,i}$ is the setting of the ith collimator. Because of machine protection and off-axis wake requirements to be discussed below, the collimator apertures $n_{y,i}$ will increase through the system. Since the resultant jitter is perpendicular in phase to the source jitter, statistically jitter from the collimation system will add in quadrature to the incoming jitter. A ratio of $t'/t = 0.7$, which would statistically produce a 25% increase in average beam jitter, is taken as an upper limit on acceptable jitter amplification.

Equation 9.48 must be solved iteratively for the required $n_{y,i}$ because the β functions may not be chosen freely to optimize the gap. The first iteration consists of making a list of all collimators that are planned for the system, taking $g = 1$ mm for all gaps, and assuming all $n_{y,i}$ are equal. Equation 9.48 can then be solved for a first guess n_y. With this value of n_y and an estimate of the β functions required at each collimator, a table of estimated gap sizes can be calculated. Any anticipated growth in n_y through the system can also be included. Now Eq. 9.48 can be used to obtain the values of t'/t for this n_y estimate. An iteration in the $n_{y,i}$ may be required to exactly meet the system amplification (t'/t) budget. This procedure is carried out in Section 9.2.5, and the results are listed in Table 9-5.

Quadrupole and Large Amplitude Wakes of Parallel Plate Collimators

Large Amplitude Resistive-Wall Wakes. The potential for the resistive-wall wake of parallel-plate collimators is given by [Piwinski]

$$V(x,y;x_0,y_0) = -\kappa f_R(\tau)\left[\frac{-x_-\sinh x_- + y_+\sin y_+}{\cosh x_- + \cos y_+} + \frac{x_-\sinh x_- + y_-\sin y_-}{\cosh x_- + \cos y_-}\right]$$
$$\text{where}\quad y_+ = \frac{\pi}{2g}(y+y_0), \qquad y_- = \frac{\pi}{2g}(y-y_0), \qquad x_- = \frac{\pi}{2g}(x-x_0), \tag{9.49}$$
$$\text{and}\quad \kappa = \frac{1}{2}\,\frac{Nr_e}{\gamma\sigma_z}\,\frac{L}{g}\,\sqrt{\lambda\sigma_x}\quad .$$

Here x and y are the horizontal and vertical position of the particle experiencing the wake, and x_0 and y_0 are the coordinates of the source of the wake. The collimator planes are set to collimate in y, and are separated by $2g$.

There are several limits of interest. One important limit ignores the difference between the horizontal position of the source and the test particles. If we are only interested in the vertical kicks we can set $x_- = 0$. Then

$$V(x_0,y;x_0,y_0) = -\kappa f_R(\tau)\left[\frac{y_+\sin y_+}{1+\cos y_+} + \frac{y_-\sin y_-}{1-\cos y_-}\right] \quad . \tag{9.50}$$

We can take the derivative of this equation to get the kick anywhere in the beam pipe

$$\Delta y' = \frac{\pi}{2}\,\frac{\kappa f_R}{g}\left[\frac{y_+ + \sin y_+}{1+\cos y_+} - \frac{y_- - \sin y_-}{1-\cos y_-}\right] \tag{9.51}$$

The kick received by particles in the core of the beam can be found by setting $y = y_0$ in Eq. 9.51.

$$\Delta y' = \frac{\pi}{2}\,\frac{\kappa f_R}{g}\left[\frac{\sin\hat{y}+\hat{y}}{1+\cos\hat{y}}\right] \qquad \text{where} \qquad \hat{y} = \pi\frac{y_0}{g} \tag{9.52}$$

The wake kick for a mis-steered beam corresponding to Eq. 9.52 is shown in Figure 9-26b.

For small y and y_0 we can expand V in a power series

$$V(x_0,y;x_0,y_0) \approx -\frac{\pi^2}{3}\,\frac{\kappa f_R}{g^2}\left[y_0 y + \frac{1}{4}y^2 + \ldots\right] \quad , \tag{9.53}$$

which produces the kick

$$\Delta y' \approx \frac{\pi^2}{3}\,\frac{\kappa f_R}{g^2}\left[y_0 + \frac{1}{2}y + \ldots\right] \quad . \tag{9.54}$$

For particles ($y = y_0$ in the beam)

$$\Delta y' \approx \frac{\pi^2}{2}\,\frac{\kappa f_R}{g}\,\frac{y}{g} \quad . \tag{9.55}$$

The coefficient of y/g in this equation would be the extrapolation to the wall of the small amplitude kick. We define this kick at the wall to be

$$\Delta y'_{ref} \equiv \frac{\pi^2}{2}\,\frac{\kappa f_R}{g} \tag{9.56}$$

For the flat part of a 20 r.l. Cu absorber with $g = 1.8\,\text{mm}$, $N = 10^{10}$, $\sigma_z = 125\,\mu\text{m}$, and $\gamma = 10^6$, $< \Delta y'_{ref} >= 11$ nr. For the flat part of a 20 r.l. copper -plated tungsten-rhenium absorber, $< \Delta y'_{ref} >= 2.6$ nr.

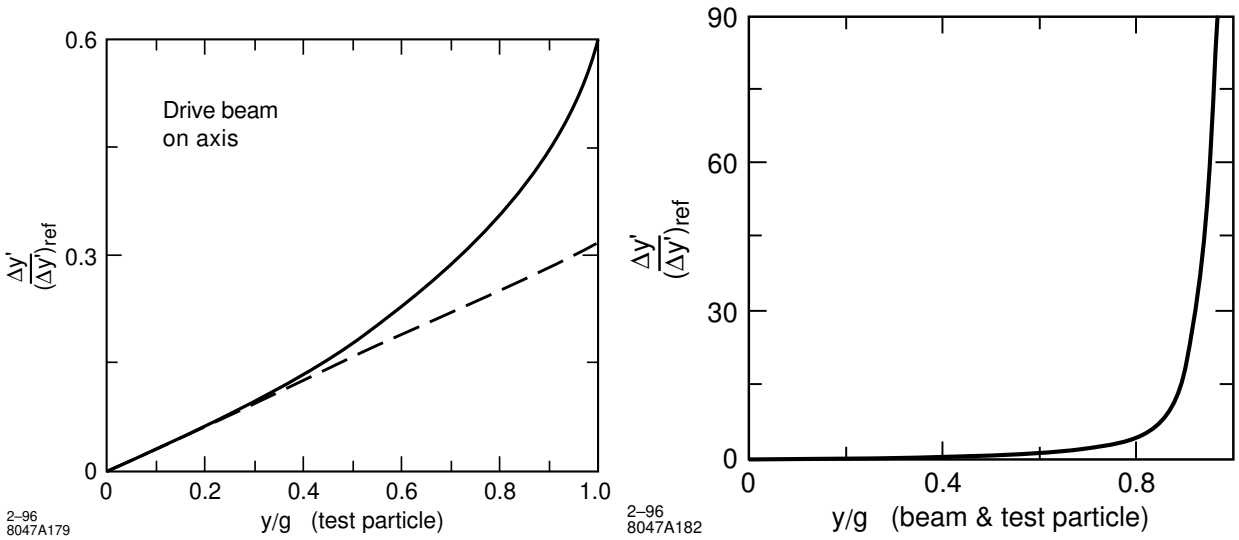

Figure 9-26. *(a) The resistive-wall wake from parallel plate collimators for an on-axis beam. (b) The resistive-wall wake from parallel plate collimators for a mis-steered beam. The wake-kick diverges as the beam approaches the collimator edge.*

Another limit of interest are wakes for on-axis beams. Keeping $x_- = 0$ and setting $y_0 = 0$, we have

$$V(x_0, y; x_0, 0) = \kappa f_R \left[\frac{2\tilde{y}}{\sin\tilde{y}}\right] \quad \text{where} \quad \tilde{y} = \frac{\pi}{2}\,\frac{y}{g} \quad . \tag{9.57}$$

Taking the derivative of this equation we get the kick

$$\Delta y'_{y_0=0} = \pi \frac{\kappa f_R}{g}\left[\frac{\sin\tilde{y} - \tilde{y}\cos\tilde{y}}{\sin^2\tilde{y}}\right] \quad . \tag{9.58}$$

As $y \to g$, $\tilde{y} \to \pi/2$, hence $\Delta y'_{y_0=0} \to \pi\kappa f_R/g$. The quadrupole term in the multipole expansion of Eq. 9.54 extrapolated to the wall would have given a kick $\Delta y' \to 1/3\Delta y'_{ref}$, which is smaller than the value of $\Delta y'_{y_0=0}$ at the wall by a factor of $\pi/6 \approx 1.9$. Figure 9-26(a) is a graph of the wake for an on-axis beam (Eq. 9.58) from $y = 0$ to $y = g$.

A third limit of interest is when both y and y_0 are close to g. Here it is useful to introduce the variable $\Delta_+ = \pi - y_+$ into Eq. 9.50 to obtain

$$V(x_0, y; x_0, y_0) = -\kappa f_R \left[\frac{\pi\sin\Delta_+}{1-\cos\Delta_+} - \frac{\Delta_+\sin\Delta_+}{1-\cos\Delta_+} + \frac{y_-\sin y_-}{1-\cos 6_-}\right] \xrightarrow{\Delta_+\to 0} -2\pi\frac{\kappa f_R}{\Delta_+} \quad . \tag{9.59}$$

As $y_0 \to g$ we have the result that

$$\Delta y' \approx \kappa g f_R \frac{1}{(g-y_0)^2} \quad . \tag{9.60}$$

When the entire beam passes near the edge of a collimator the wake kick can be very large. However, as a beam approaches the wall, when $g - y_0 \le \sigma_x$, the singularity of the potential found in Eq. 9.53 becomes modified by the fact that $x_- \neq 0$. We must return to Eq. 9.49 and expand in x_- , Δ_+, and y_-. The result is

$$V(x, y; x_0, y_0) \quad = \quad -\kappa f_R \left[\frac{\pi\sin\Delta_+}{\frac{x_-^2}{2} + (1-\cos\Delta_+)} - \frac{x_-^2 + \Delta_+\sin\Delta_+}{\frac{x_-^2}{2} + (1-\cos\Delta_+)} + \frac{x_-^2 + y_-\sin y_-}{\frac{x_-^2}{2} + (1-\cos y_-)}\right]$$

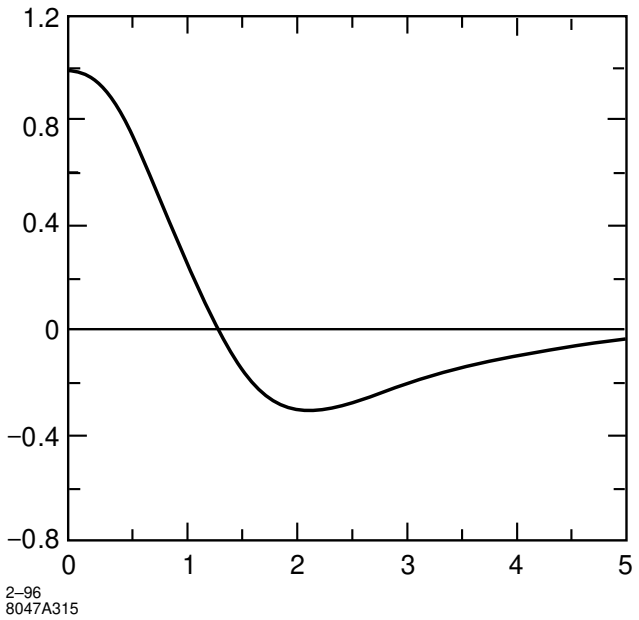

Figure 9-27. *The coefficient of the first power of λ in Eq. 9.65.*

$$\xrightarrow[\Delta_+\to 0]{} -2\pi\kappa f_R \frac{\Delta_+}{(x_-^2+\Delta_+^2)} \tag{9.61}$$

It is an interesting feature of this potential that for $\Delta_+ > x_-$ the force is toward the wall, while for $\Delta_+ < x_-$, the force is away from the wall. For $x_- = 0$ the force is always toward the wall (positive), and indeed the potential diverges as $1/\Delta_+$ as in Eq. 9.59.

Assuming the beam has a Gaussian shape, we can integrate Eq. 9.61 over the horizontal distribution. We have the result [Stupakov 1995].

$$\lim_{\Delta_+\to 0}\frac{1}{\sqrt{2\pi}}\int_{-\infty}^{\infty}\frac{dx_0}{\sigma_{x_0}}e^{-\frac{x_0^2}{2\sigma_{x_0}^2}}V(x,y;x_0,y_0) = -\frac{\sqrt{2\pi}\kappa f_R}{\sigma_{x_-}}\left[\pi e^{-\frac{\xi^2}{2}} - \frac{\Delta_+}{\sigma_{x_-}}\sqrt{2\pi}\,h_1(\xi)\right]$$
$$\text{where}\quad \sigma_{x_-} = \frac{\pi}{2g}\sigma_{x_0}\,,\quad \text{and}\quad \xi = \frac{x}{\sigma_{x_0}}\quad . \tag{9.62}$$

A plot of $h_1(\xi)$ is shown in Figure 9-27. From Eq. 9.62 we may obtain the horizontal and vertical kicks:

$$\begin{aligned}\Delta y'(x,y',y_0) &\approx \frac{4\kappa g f_R}{\sigma_{x_0}^2}h_1(\xi)\\ \Delta x'(x,y',y_0) &\approx -\sqrt{\frac{\pi}{2}}\frac{4\kappa g f_R}{\sigma_{x_0}^2}\xi e^{-\frac{\xi^2}{2}}\quad .\end{aligned} \tag{9.63}$$

Note that these kicks do not depend on the distance to the wall of either the source or the test particle, as would be expected for a plane geometry. Comparing Eq. 9.63 with 9.60 we see, for $\xi = 0$, the kick from Eq. 9.60 limits out at $g - y_0 = \sigma_{x0}/2$.

Geometric Wake Formulae. For the quadrupole term from the geometric wake we will use Eq. 9.24.

When the beam is close enough to the wall that it is appropriate to neglect the contribution of the opposite wall, the expression for the wake is [Stupakov 1996]

$$\Delta y'^{T}_{G}(\tau) = 4A \int \frac{a'^2}{a} ds = 4A\theta \ln\left[\frac{0.4g}{a_g}\right] \tag{9.64}$$

where a is the distance from the beam to the wall as a function of s, and a_g is the nearest approach of the beam to the taper.

If the beam is very close to the wall, the dimension of the beam parallel to the wall be comes important. Then the appropriate formula is

$$\Delta y'^{T}_{G} = 4A \int \frac{aa'^2}{x_2 + a^2} ds = 2A\theta \ln\left[\frac{x^2 + (0.4g)^2}{x^2 + a_g^2}\right] \tag{9.65}$$

where $\theta = b - g/L_T$.

This must now be integrated over the horizontal distribution. This can be performed in the limit of $a_g < \sigma_x$ to give (independent of the exact value of a_g)

$$\Delta y'^{T}_{G} = 2A\theta \ln\left[1.9\left(\frac{0.4g}{\sigma_x}\right)^2\right] \tag{9.66}$$

A table of numerical results for the collimators of the beam delivery lattice is given in Section 9.2.5.

If the Equation 9.26 is valid, the dipole term will be longer than this term, and is the current near-wall limit.

Consequences of Quadrupole and Near-Wall Wakes

Quadrupole-Wake Focusing. We see in Eq. 9.54 that for the resistive-wall wake the quadrupole term is 1/3 of the total wake kick. If the quadrupole wake were written as $\Delta y' = k_R \Delta y$, then $\Delta y'/\hat{\sigma}_{y'} = (k_R\beta)\Delta y/\sigma_y$. Hence we have

$$\text{“}k_{R,i}\beta_i\text{”} = 0.4\,\frac{1}{3}\left(\frac{t'_i}{t_i}\right)\left[\frac{\sqrt{\frac{g_i}{g_{0i}}} + \frac{g_{0i}}{g_i}}{2\sqrt{\frac{g_i}{g_{0i}}} + \frac{g_{0i}}{g_i}}\right] \quad . \tag{9.67}$$

The factor of 1/3 comes from the fact that, for the resistive-wall wake, 1/3rd of the wake comes from the quadrupole wake. t'_i/t_i is the number of σ' from a 1-σ displacement at the ith collimator. The bracket gives the fraction of the wake that is a resistive-wall wake. One-half of the taper wake is resistive-wall. At $g_i = g_{0i}$ the second bracket has the value 2/3 which is just the fraction of the total wake that is resistive-wall at the optimum gap. The value of the bracket lies between 1/2 and 1.

The initial factor of 0.4 comes from the fact that $\sigma_{fR}/ < f > \approx 0.4$. The average quadrupole effect of the wakes will be tuned out when the waist is tuned. It is the spread in focusing that occurs longitudinally along the bunch that is untunable, and will result in a luminosity loss.

As we have seen above in Eq. 9.65, the geometric parallel plate wakefield also has a quadrupole term. In other words, even for on-axis beams there will be a wakefield kick for off-axis particles. For the geometric wake the fraction of the total wake that is a quadrupole wake is 1.43/3.28 = .44. This is somewhat larger than for the resistive-wall wake where this fraction is equal to 0.33. Multiplying this result together with

the fraction of the wake from a collimator that is geometric we have

$$\text{“}k_G\beta_i\text{”} = 0.4\left(\frac{t_i'}{t_i}\right)\left[\frac{.16\sqrt{\frac{g_i}{g_{0i}}}}{2\sqrt{\frac{g_i}{g_{0i}}}+\frac{g_0 iu}{g_i}}\right] \quad . \tag{9.68}$$

The bracket has a value less than 1/2. Adding the resistive-wall and geometric together we have

$$\text{“}k_{R+G,i}\beta_i\text{”} = 0.4\left(\frac{t_i'}{t_i}\right)\left[\frac{0.77\sqrt{\frac{g_i}{g_{0i}}}+0.33\frac{g_0 i}{g_i}}{2\sqrt{\frac{g_i}{g_{0i}}}+\frac{g_{0i}}{g_i}}\right] \tag{9.69}$$

The value of the bracket lies between 0.39 and 0.33.

We can sum Eq. 9.69 over all collimators, taking the worst case of 0.39 for the bracket to get

$$\text{“}k_{R+G}\beta''_{\text{Total}} \leq (0.4)\left(\frac{t'}{t}\right)[0.39] \leq 0.11 \tag{9.70}$$

The luminosity is decreased by 2% when $k_Q\beta = 0.2$, hence the luminosity loss expected from the quadrupole focusing of collimators is less than 0.5%.

Near-Wall Wakes for On-Axis Beams. For parallel-plate collimators there is a wakefield even when the beam is on-axis. This raises the concern that particles passing near the collimator could be deflected into the tails and cause a problem downstream [Yokoya 1995].

We have shown above that for the resistive-wall wake the value of the wake at the wall for an on-axis beam is 1.9 times the linear extrapolation of the quadrupole wake of the on-axis beam. It is possible, by integrating the resistive-wall wake over the taper, to calculate the wake for a particle passing at the taper minimum. One finds the wake at the taper minimum is 1.4 times the linear extrapolation of the quadrupole wake. Putting these results together we get the following expression for the kick at the wall from the resistive-wall part of the wake:

$$\frac{\Delta y'_{RWX}}{\sigma_{y'}} = \frac{1}{3}n_{y,i}\left(\frac{t_i'}{t_i}\right)\left[\frac{1.4\sqrt{\frac{g_i}{g_{0i}}}+1.9\frac{g_{0i}}{g_i}}{2\sqrt{\frac{g_i}{g_{0i}}}+\frac{g_{0i}}{g_i}}\right] \quad . \tag{9.71}$$

For the geometric wake we have not formally found an answer, but will assume that it is a factor of 2 times the linear extrapolation of the quadrupole wake. Hence

$$\frac{\Delta y'_{GWX}}{\sigma_{y'}} \cong (0.44)n_{y,i}\left(\frac{t_i'}{t_i}\right)\left[\frac{2\sqrt{\frac{g_i}{g_{0i}}}}{2\sqrt{\frac{g_i}{g_{0i}}}+\frac{g_{0i}}{g_i}}\right] \quad . \tag{9.72}$$

Adding Eq. 9.71 and 9.72 we obtain

$$\frac{\Delta y'_{R+G,WX}}{\sigma_{y'}} = n_{y,i}\left(\frac{t_i'}{t_i}\right)\left[\frac{1.34\sqrt{\frac{g_i}{g_{0i}}}+0.63\frac{g_{0i}}{g_i}}{2\sqrt{\frac{g_i}{g_{0i}}}+\frac{g_{0i}}{g_i}}\right] \quad . \tag{9.73}$$

The bracket has a value between 0.67 and 0.63. When we sum over i, it should be over the upstream collimators only. Let us assume that 3/5 of the collimation budget for t'/t is in the first stage. Then Eq. 9.73

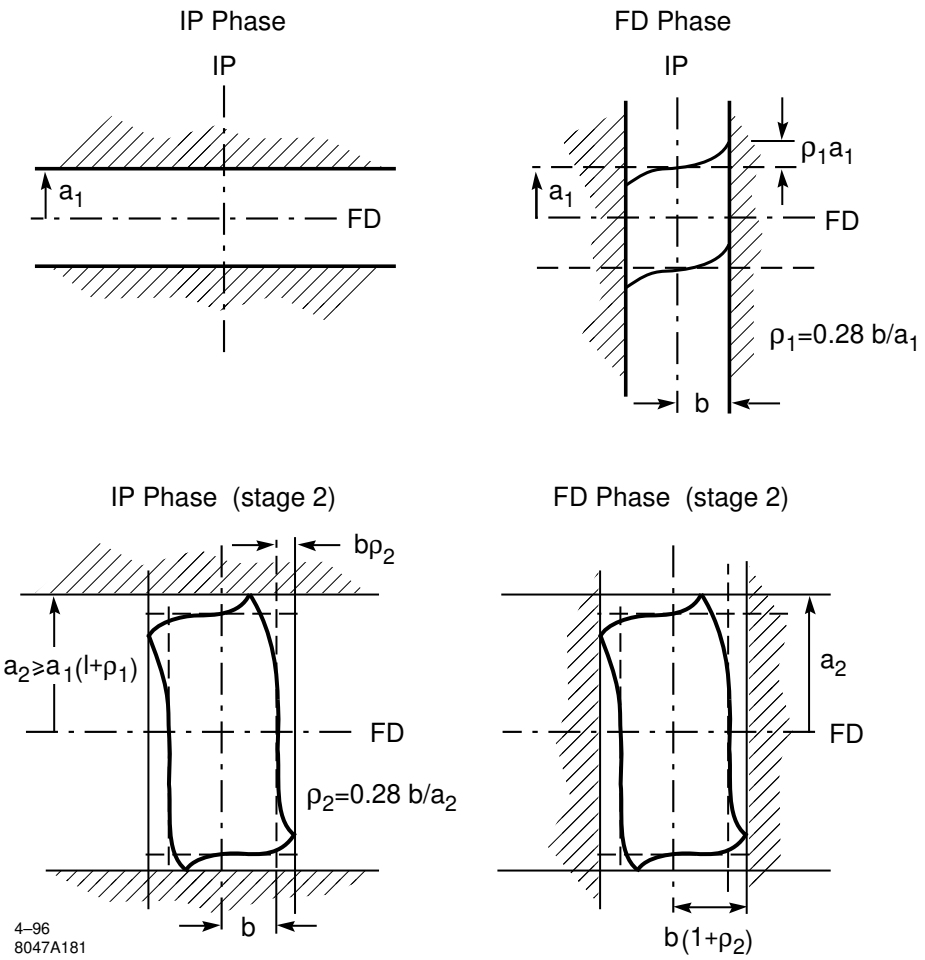

Figure 9-28. *When phase #2 is collimated, the on-axis beam wake which is present for parallel plate collimators, moves particles into a phase space region that was previously collimated in phase #1.*

gives

$$\left.\frac{\Delta y'_{R+G,WX}}{\sigma_{y'}}\right|_{stage1} \leq \frac{3}{5} n_{y1} \left(\frac{t'}{t}\right) [0.67] \leq 0.28\ n_{y1} \tag{9.74}$$

The consequences of near-wall wakes for on-axis beams can be clarified by considering the particle motion in a sequence of normalized phase-space diagrams. See Figure 9-28. Let us suppose that the IP phase is first collimated to some aperture "$a_1\sigma$" and then the FD phase is collimated to an aperture "$b\sigma$". Because of the wake at the wall, the IP boundary will be distorted, as shown in Figure 9-26a, and particles will extend into the previously collimated region by an amount $0.28b\sigma$ (see Eq. 9.74). When the IP phase is collimated again, at a larger aperture "$a_2\sigma$" the distortion will be $0.28a_2(b/a_2)^2\sigma = (0.28b/a_2)b\sigma$. The factor $(b/a_2)^2$ arises from the assumption that b was the appropriate aperture for 3/5 of the 0.7 jitter amplification budget, and the effect of $a_2 > b$ can be determined by using the fact that the kick scales as the aperture squared. In Figure 9-28 we have set $\rho_2 = 0.28\ b/a_2$.

Because of near-wall wake for mis-steered beam, to be discussed in the next section, $a_2/b \approx 3.5$, hence $\rho_2 = 0.28b/a_2 = 0.08$. The stage-2 FD aperture must be enlarged by only 8%: from 36 to 39 in the vertical plane, from 5 to 5.4 in the horizontal plane.

Near-Wall Wakes for Mis-steered Beams. We would like to estimate the near-wall kick. The limit from the resistive-wall part is $(\kappa f_R/g)(2g/\sigma_x)^2 < h_1 > \approx 1/\pi^2 \Delta y'_{ref}(2g/\sigma_x)^2$. Hence we have

$$\frac{\Delta y'_{RWW}}{\sigma_{y'}} = \frac{4}{\pi^2}\left(\frac{g}{\sigma_x}\right)^2 n_{y,i}\left(\frac{t'_i}{t_i}\right)\left[\frac{\frac{g_{0i}}{g_i}}{2\sqrt{\frac{g_i}{g_{0i}}}+\frac{g_{0i}}{g_i}}\right] \quad . \tag{9.75}$$

The geometric-wake limit can be found from Eq. 9.66, putting $A\theta$ as the extrapolation of the small-amplitude wake to the wall:

$$\frac{\Delta y'_{GWW}}{\sigma_{y'}} = 2\ln\left[1.9\left(\frac{0.4g}{\sigma_x}\right)^2\right] n_{y,i}\left(\frac{t'_i}{t_i}\right)\left[\frac{\sqrt{\frac{g_i}{g_{0i}}}}{2\sqrt{\frac{g_i}{g_{0i}}}+\frac{g_{0i}}{g_i}}\right] \quad . \tag{9.76}$$

We have not included any term for the resistive-wall part of the taper. Let us assume that only that length of taper contributes for which the surface is still within $\sigma_x/2$ of the taper minimum, since the wake falls off very sharply beyond that distance. When we integrate the resistive-wall-wake formula over this distance we find that the contribution to the small-amplitude wake for this region as compared to the whole taper is the fraction σ_x/g. Thus we have the result

$$\frac{\Delta y'_{RWW}}{\sigma_{y'}} = \frac{4}{\pi^2}\left(\frac{g}{\sigma_x}\right)^2 n_{y,i}\left(\frac{t'_i}{t_i}\right)\left[\frac{\sqrt{\frac{g_i}{g_{0i}}}}{2\sqrt{\frac{g_i}{g_{01}}}+\frac{g_{0i}}{g_i}}\right] \quad . \tag{9.77}$$

Combining these results we get (setting $g/\sigma_x = 10$)

$$\frac{\Delta y'_{R+GWW}}{\sigma_{y'}} = n_{y,i}\left(\frac{t'_i}{t_i}\right)\left[\frac{7.4\sqrt{\frac{g_i}{g_{0i}}}+40\frac{g_{0i}}{g_i}}{2\sqrt{\frac{g_i}{g_{01}}}+\frac{g_{0i}}{g_i}}\right] \quad . \tag{9.78}$$

The bracket lies between 1.9 and 40. The resistive-wall contribution is much larger than the taper. If we assume g/g_{0i} is about 2, we get a value for the bracket of about 10. This gives an estimate for the first stage of

$$\left.\frac{\Delta y'_{R+G,WW}}{\sigma_{y'}}\right|_{stage1} \leq \frac{3}{5}\, n_{y1}\left(\frac{t'}{t}\right) 10 \leq 4.2\, n_{y1} \tag{9.79}$$

For $n = 36$ this gives the estimate for the near-wall kick of $150\sigma'$. The detailed calculation with the exact apertures of the lattice gives $118\sigma'$. A plot of this kick with distance from the wall is shown in Figure 9-29(a). Only the resistive-wall terms, adding up to $90\sigma'$ are included.

While these kicks are large, they are still in the beam pipe and smaller than the dynamic aperture of the final-focus system. Also because of the τ dependence, the spread of these kick is at least $0.4(120)\sigma_{y'} = 48\sigma_{y'}$. Additionally, there is a dependence on x, making the spread about equal to the magnitude of the kick. This can be deduced from the following relationships:

$$< \Delta y' > \;=\; \frac{4\kappa g}{\sigma_{x_0}^2}\langle f_R\rangle\langle h_1(\xi)\rangle = 0.41\frac{4\kappa g}{\sigma_{x_0}^2}$$

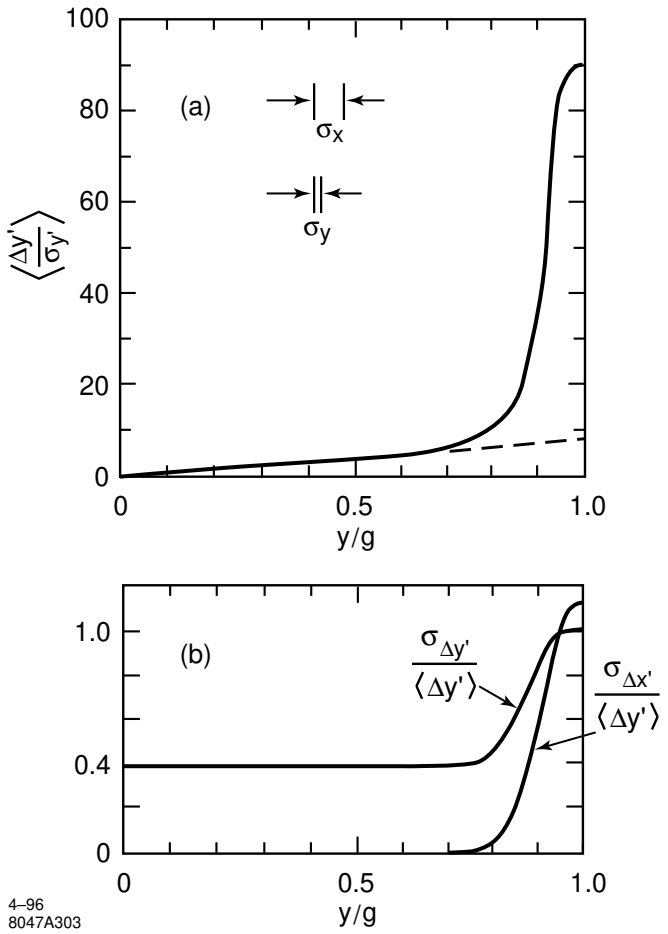

Figure 9-29. *(a) The wake kick as a function of distance to the wall showing the cut-off at the wall when the distance approaches the width of the bunch. (b) An estimate for the variation of the σ of the wake-kicks of (a).*

$$\begin{aligned}
\sigma_{\Delta y'} &= \frac{4\kappa g}{\sigma_{x_0}^2}\sqrt{\langle f_R^2\rangle\langle h_1(\xi)^2\rangle - \langle f_R\rangle^2\langle h_1(\xi)\rangle^2} = 0.44\,\frac{4\kappa g f_R}{\sigma_{x_0}^2} \\
\langle \Delta x'\rangle &= 0 \qquad (9.80)\\
\sigma_{\Delta x'} &= \sqrt{\frac{\pi}{2}}\,\frac{4\kappa g}{\sigma_{x_0}^2}\sqrt{\langle f_R^2\rangle\langle h_2(\xi)^2\rangle - \langle f_R\rangle^2\langle h_2(\xi)\rangle^2} = 0.49\,\frac{4\kappa g f_R}{\sigma_{x_0}^2}
\end{aligned}$$

where $h_2(\xi) \cong \xi e^{-\frac{\xi^2}{2}}$, $\left\langle h_2(\xi)^2\right\rangle = 3^{-3/2}$, $\langle h_1(\xi)\rangle = 0.5$, and $\left\langle h_1(\xi)^2\right\rangle = 0.44$.

It is remarkable that both the sigmas of the horizontal and vertical kick are a bit larger than the average vertical kick. An estimate for the variation of these σ with amplitude is shown in Figure 9-29(b).

We have gone in to some detail here because these kicks are large. Since there can be no spoiler in the second stage of the IP collimation, either the collimators at the next stage need to be set back this far, or it could be that the beam is blown up by the kicks and has a sufficiently large area that it is permissible for it to hit the collimator. As mentioned above, the sigma of the kick near the wall is very close to the magnitude of

the kick itself. And both the vertical and horizontal beam sizes are blown up. However the beam size must be very large for copper. We shall see that a kick of 135σ is required to blow up the beam so that the area of the beam is larger than the mandatory $(2.2\,\mathrm{mm})^2$.

To get an estimate for the enlarged horizontal σ we use the product

$$\begin{aligned} \text{“}\sigma_{y_2}\text{”} &= R_{34}\sigma_{\Delta y_1'} = \frac{\sigma_{\Delta y_1'}}{\langle \Delta y_1' \rangle}\frac{\langle \Delta y_1' \rangle}{\sigma_{y_1'}} R_{34}\sigma_{y_1'} = \frac{\sigma_{\Delta y_1'}}{\langle \Delta y_1' \rangle} n_{y_1'}\sigma_{y_2} \\ \text{“}\sigma_{x_2}\text{”} &= R_{12}\sigma_{\Delta x_1'} = \left\langle \frac{R_{12}}{R_{34}} \right\rangle \frac{\sigma_{\Delta x_1'}}{\langle \Delta y_1' \rangle} n_{y_1'}\sigma_{y_2} \\ \text{“}\sigma_{x_2}\text{”}\text{“}\sigma_{y_2}\text{”} &= \left\langle \frac{R_{12}}{R_{34}} \right\rangle \frac{\sigma_{\Delta x_1'}}{\langle \Delta y_1' \rangle}\frac{\sigma_{\Delta y_1'}}{\langle \Delta y_1' \rangle} n_{y_1'}^2\sigma_{y_2}^2 \end{aligned} \tag{9.81}$$

The average $< R_{12}/R_{34} >$ is an rms average weighted by the relative importance of the three collimators in stage 1. For the lattice described in Section 9.2.5 it has a value of about 1/2. Also for this lattice $\sigma_{y2} = 23\,\mu$m. To get the sigma product to be $4.8\,\mathrm{mm}^2$ we will need $n_{y'} = 135$. This is larger than the 118-$\sigma_{y'}$ maximum kick, and will not occur. Figure 9-30 shows the phase space distortions due to these large kicks when the beam is off-axis.

We might conclude that the aperture of vertical IP stage 2 collimation must be (118+35) $\sigma_{y'} = 153\sigma_{y'}$ because the beam could start out near the collimator edge. But if the beam was already out at 35 σ before receiving the wake kick, it would have gotten a rather large kick in the first stage of the IP collimation. That implies that all of the beam could not have been be near the edge. This effect dies off rapidly though, and by an amplitude of 30 σ the kick was 15 σ' with a spread of about 9 σ'. For an amplitude of 28 σ, the spread is 4.5 σ'. The conclusion is that the required aperture is about $(118 + 30)\sigma_{y'} \approx 150\sigma_{y'}$, not much less.

Fortunately the dynamic aperture of the final-focus system is large enough to accommodate these large amplitude particles. See Figure 9-5.

9.2.5 Lattice Description and Analysis

Collimation System Schematic

Figure 9-31 is a schematic layout of the collimation-system spoilers and absorbers according to the guidelines arrived at in the preceding sections. In this system we have added a second stage for the FD-phase collimation. This is not necessary according to our estimates. The inclusion of a second FD-phase collimation section should be considered tentative. In the diagram of Figure 9-31 we have let a spike represent a titanium spoiler and a rectangular block represent a copper absorber. Further,

- $x + \eta\delta$ indicates collimation outside of the lines $x + \eta\delta = \pm n_x\sigma$ in an (x, δ) plane, with x at the IP phase,
- $x' + \eta\delta$ indicates collimation outside of $x' + \eta\delta = \pm n_x\sigma$ in an (x', δ) plane, with x' at the FD phase, and
- y and y' indicate collimation at $\pm n_y\sigma$ in the IP and FD phase, respectively.

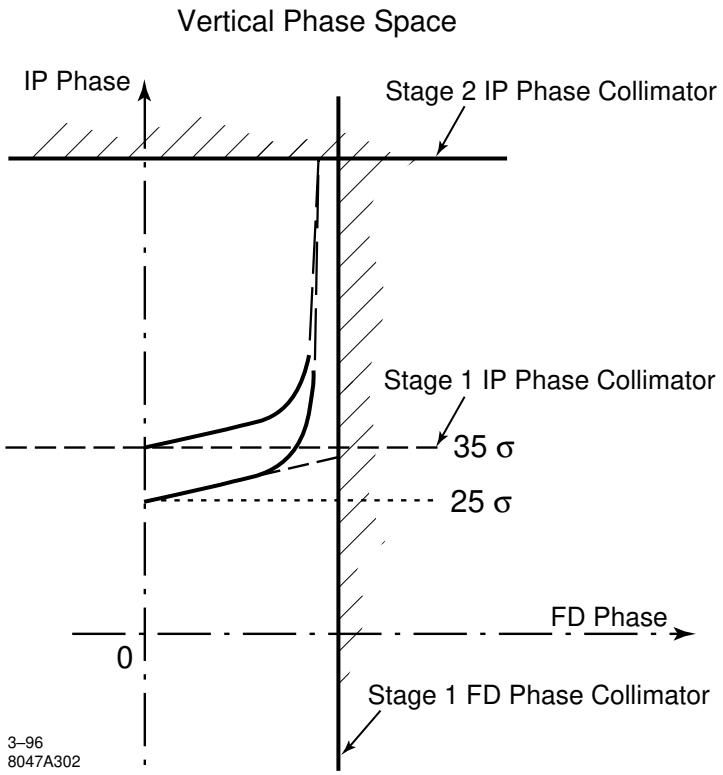

Figure 9-30. *This figure illustrates the enlargement of the aperture that is necessary to avoid impact of a mis-steered beam which narrowly misses upstream spoilers.*

Figure 9-32 shows the volume in (x, x', δ) space collimated by this arrangement. The horizontal and vertical collimation can be interleaved since on the one hand we need large βs in both planes to achieve sufficient spot area, and on the other hand, the chromaticity can be compensated by interleaved sextupoles without problems arising from octupole aberrations.

Each element in the first spoiler and absorber set is located at $-I$ from a corresponding element in the second set. Absorbers with lesser absorption requirements, that will be located downstream of spoilers and absorbers to protect various components and absorb remaining scatter, have not been specifically indicated.

The Lattice

Lattice Functions. Lattice functions for an optical system which satisfies the requirements we have outlined are shown in Figure 9-33 [Helm]. Sextupoles are located at each of the maximum β points.

System Bandpass. Figure 9-34 shows the exit spot size as a function of incident energy for the 1-TeV-c.m. collimation system. At $\delta = \pm 0.5\%$ the spot size has grown by about 4%. This is satisfactory, when one considers that the net result for a beam will be an average over the energy distribution.

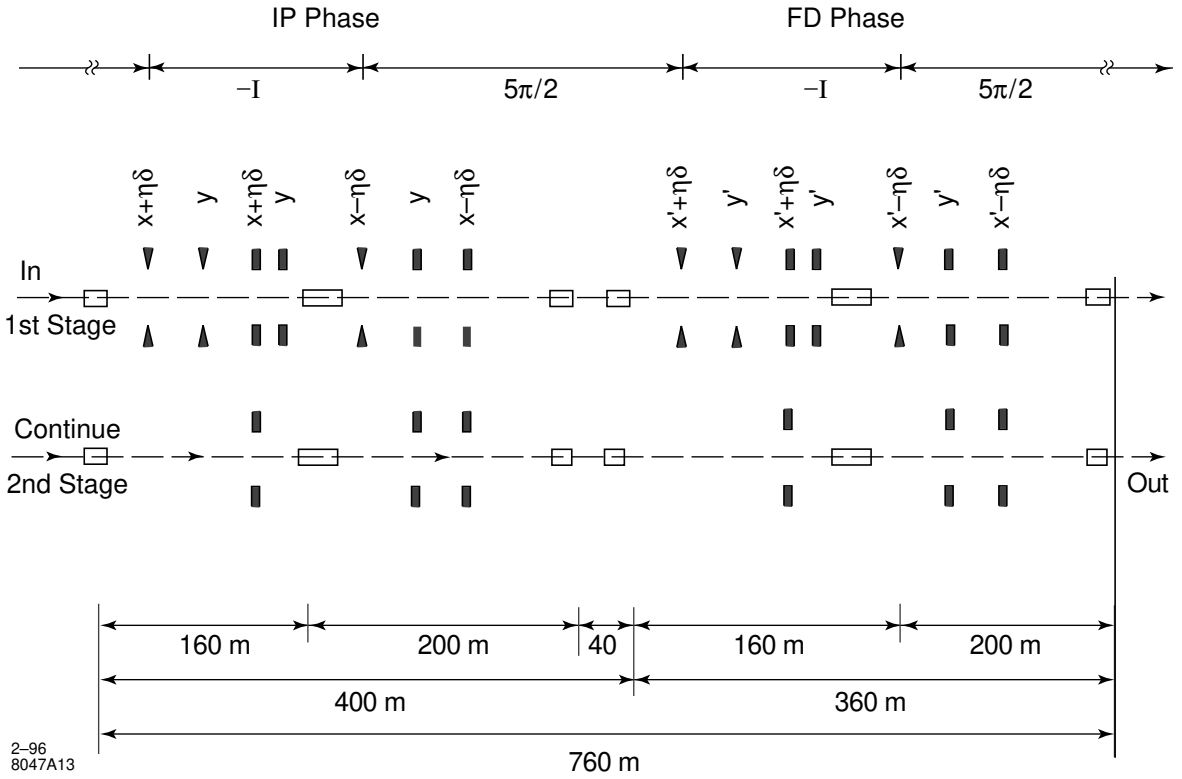

Figure 9-31. *Schematic of the collimation system spoilers and absorbers.*

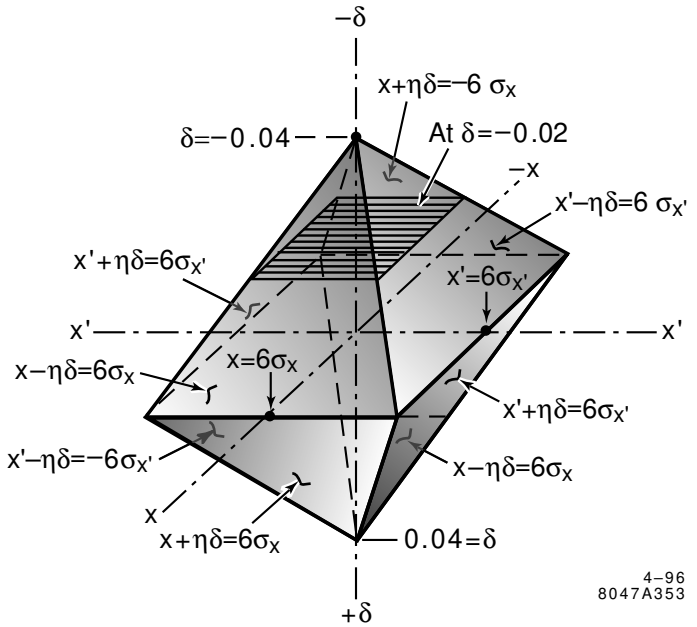

Figure 9-32. *The 3-D volume in x, x', δ space that remains after the beam passes through the spoilers of the collimation system defined in Figure 9-31.*

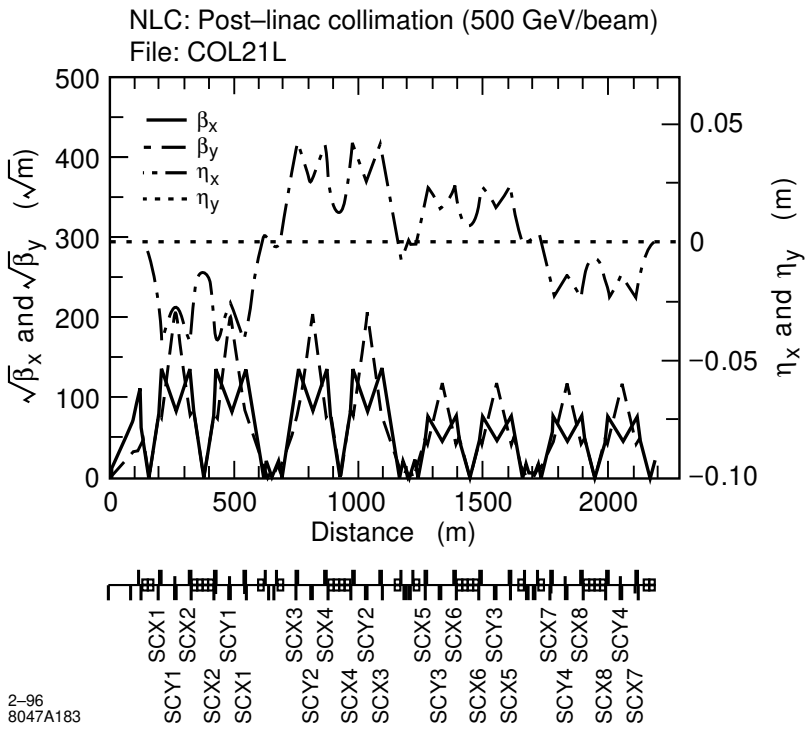

Figure 9-33. *The 1-TeV-c.m. collimation system lattice functions.*

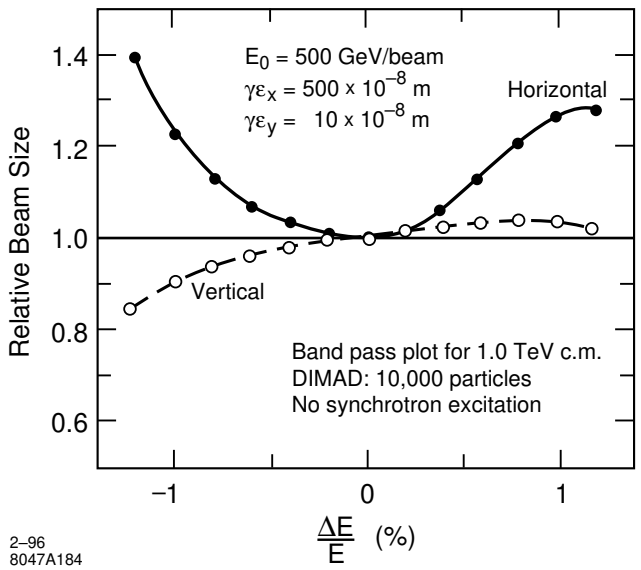

Figure 9-34. *The spot size increase in the 1-TeV-c.m. collimation system as a function of mono-energetic energy offset.*

Collimator Apertures and Wakes

Collimator Apertures and Small Amplitude Wakes. We will now turn to calculating the minimum values of n_x and n_y that may be collimated. The results are presented in Table 9-5.

For this discussion we will concentrate on the FD phase, and assume that the system consists of two stages, one in the collimation system denoted in Table 9-5 by FD_V_1 and FD_H_1 for the vertical and horizontal plane, respectively, and one in the final-focus system, labeled FD_V_3 and FD_H_3. The data on the second stage of FD collimation is also included but the results are not summed into the totals. In the vertical plane we assume there are one Ti spoiler and one Cu absorber in the first stage and two copper-plated W-Re absorbers in the second stage. In the horizontal plane we will assume there are two Ti spoilers and two Cu absorbers in the first stage and two copper-plated W-Re absorbers in the second stage. The spoilers and absorbers are doubled in the first stage of the horizontal plane because energy is also collimated in this plane.

The n_i have been chosen to produce a t'/t value less than 0.7. They have been expanded one stage to the next to allow for near-wall wake effects and alignment inaccuracies.

In the final-focus system the gaps are determined by a complicated set of relationships that determine optimum βs required for minimizing higher order aberrations, tolerances and system length. At 1-TeV c.m. we have (for the 1.5-TeV design operated at 1.0 TeV, see Figure 11-12) $\beta_{x,max} = 10^5$ and $\beta_{y,max} = 3\ 10^5$. βs are a factor of three smaller for the 0.5-TeV-c.m. design, Figure 11-8. They can be taken to scale approximately linearly with energy. Hence we have chosen the worst-case 1.5-TeV-c.m. β values in Table 9-5.

In the first stage the gaps are determined by the requirements that the βs be large enough so that the impact of a full beam train will not destroy the spoiler. For $\varepsilon_x = 5\ 10^{-12}$ m-rad and $\varepsilon_y = 8\ 10^{-14}$ m-rad, we have the condition that at the spoilers, $\sqrt{(\beta_x\beta_y)} \geq 1.6\ 10^4$, where we used the condition from Table 9-3 that $\sqrt{(\sigma_x\sigma_y)} \geq 100\,\mu$m. For Table 9-5 we have used the values from the lattice of Figure 9-33. Because the parameters have changed during the course of design, this does not quite meet the beta-product specification at the horizontal spoilers. For this lattice $\sqrt{(\beta_x\beta_y)} = 1.1\ 10^4$ at the horizontal spoilers and $\sqrt{(\beta_x\beta_y)} = 1.7\ 10^4$ at the vertical spoilers . The $\sqrt{\beta}$s must be 25% larger at the horizontal spoilers. Another change in this lattice must be made to increase the R_{12} and R_{34} between spoiler and absorber. See Section 9.2.2. On the other hand the second stage of FD collimation can be omitted altogether. Present system length will remain adequate.

In Table 9-5 we see that within the collimation system gaps run between a comfortable 0.8 mm and 2.0 mm. The ratio of the wake kick to the kick of the same collimator with an optimum gap, denoted by ϕ_i, has a maximum value of 2.4.

All absorbers have a length of 20 r.l. If necessary this could be reduced to 10 r.l. In this sense we feel there is some margin in the aperture limits derived.

Collimator Focusing and Near-Wall Kick Strengths. Table 9-6 presents the results from calculating the focusing strengths and near-wall kick strengths of all collimators. The focusing totals agree with the estimations of Section 9.2.4 and, because of a waist location at the IP that varies longitudinally within the bunch, will add 0.5% to the luminosity loss.

The near-wall kick strengths for on-axis beams for the 1st vertical FD stage (FD_V_1) add up to 9.8 σ'. The estimate of Eq. 9.79 equal to 0.28 n_y has the value 10 σ'. Because the second-stage IP collimators must be opened up to 150 σ to insure passive protection from mis-steered beams, the 10 σ plays little role here. And because the second-stage collimators are set this wide, the wake effects on the second (or third) stage FD collimators is tiny total of 0.4 σ.

Location	Sect.	Collimator	$\sqrt{\beta}$ ($\sqrt{m}$)	n_i	g_i (mm)	g_i/g_{0i}	ϕ_i	$t_i'/t_i = (\overline{n}_i/n_i)^2\phi_i$
FD_V_1	1	Ti Spoiler	200	36	2.0	11.1	2.3	0.22
		Cu Absorber	40		0.8	0.8	1.0	0.10
	2	W Absorber	200		1.4	3.7	1.4	0.09
FD_V_2	2	W Absorber	140	40	0.9	2.3	1.2	(0.06)
FD_V_3	1	W Absorber	550	42	6.5	17.0	2.8	0.13
	2	W Absorber	550		6.5	17.0	2.8	0.13
Totals:		**6 Collimators**						**0.66**
FD_H_1	1	Ti Spoiler	140	5	1.6	8.6	2.0	0.16
		Cu Absorber	140		1.6	1.7	1.0	0.09
	2	Ti Spoiler	140		1.6	8.6	2.0	0.16
		Cu Absorber	140		1.6	1.7	1.0	0.09
FD_H_2	1	W Absorber	80	6	1.0	2.8	1.2	(0.04)
	2	W Absorber	80		1.0	2.8	1.2	(0.04)
FD_H_3	1	W Absorber	300	7	4.7	12.1	2.4	0.06
	2	W Absorber	300		4.7	12.1	2.4	0.06
Totals:		**8 Collimators**						**0.63**
IP_V_1	1	Ti Spoiler	200	36	2.0	11.1	2.3	0.22
		Cu Absorber	40		0.8	0.8	1.0	0.10
	2	W Absorber	200		1.4	3.7	1.4	0.09
IP_V_2	2	W Absorber	140	150	3.3	3.3	1.3	0.01
Totals:		**4 Collimators**						**0.42**
IP_H_1	1	Ti Spoiler	140	5	1.6	8.6	2.0	0.16
		Cu Absorber	140		1.6	1.5	1.0	0.09
	2	Ti Spoiler	140		1.6	8.6	2.0	0.16
		Cu Absorber	140		1.6	1.5	1.0	0.09
IP_H_2	1	W Absorber	75	15	2.7	2.6	1.2	0.01
	2	W Absorber	75		2.7	2.6	1.2	0.01
Totals:		**6 Collimators**						**0.52**

Table 9-5. *A list of all the collimators in the collimation and final-focus system showing the number of σ collimated at each and the contribution to the total collimation budget. The β functions from the lattice shown in Figure 9-33 have been used to calculate beam sizes at each collimator. The second stage of the FD collimation is optional and has not been included in totals. The large second-stage IP apertures are dictated by machine protection requirements. Calculations are based on $\alpha_G = \alpha_R = \pi^2/8$.*

Location	Sect	Collim.	Quad "$k\beta$" Strength for On-Axis Bm.		Near Wall Kick for On-Axis Bm.		Near Wall Kick for Near Wall Beam			
			RW	G	RW (σ')	G (σ')	RW nr	RW (σ')	G nr	G (σ')
FD_V_1	1	Ti Spoil	0.01	0.02	1.9	3.4	48	34	24	17.0
		Cu Abs.	0.01	0.01	1.4	1.0	124	37	16	5.0
	2	W Abs.	0.01	0.01	0.8	1.3	40	20	12	6.0
FD_V_2	2	W Abs.	0.00	0.00	0.7	0.9	64	18	16	4.0
FD_V_3	1	W Abs.	0.01	0.01	1.3	2.3	53	102	6	11.0
	2	W Abs.	0.01	0.01	1.3	2.3	53	102	6	11
Totals:		**6 Coll.**	**0.05**	**0.06**	**7.4**	**11.2**				
FD_H_1	1	Ti Spoil	0.01	0.01	0.2	0.3	110	0.7	25	1.5
		Cu Abs.	0.01	0.00	0.1	0.1	270	1.7	11	0.7
	2	Ti Spoil	0.01	0.01	0.2	0.3	180	0.7	25	1.5
		Cu Abs.	0.01	0.00	0.1	0.1	270	1.7	11	0.7
FD_H_2	1	W Abs.	0.00	0.00	0.1	0.1	240	0.9	13	0.5
	2	W Abs.	0.00	0.00	0.1	0.1	240	0.9	13	0.5
FD_H_3	1	W Abs.	0.00	0.00	0.1	0.2	6	0.8	6	0.9
	2	W Abs.	0.00	0.00	0.1	0.2	6	0.8	6	0.9
Totals:		**8 Coll.**	**0.04**	**0.02**	**0.9**	**1.4**				
IP_V_1	1	Ti Spoil	0.01	0.02	1.9	3.4	48	34.0	24	17
		Cu Abs.	0.01	0.01	1.4	1.0	120	37.0	16	5
	2	W Abs.	0.01	0.01	0.8	1.3	40	20.0	12	6
IP_V_2	2	W Abs.	0.000	0.00	0.5	0.6	240	69.0	10	3
Totals:		**4 Coll.**	**0.03**	**0.04**	**4.6**	**6.3**				
IP_H_1	1	Ti Spoil	0.01	0.01	0.2	0.3	18	1.1	25	1.5
		Cu Abs.	0.005	0.00	0.1	0.1	27	1.7	11	0.7
	2	Ti Spoil	0.01	0.01	0.2	0.3	18	1.1	25	1.5
		Cu Abs.	0.005	0.00	0.1	0.1	27	1.7	11	0.7
IP_H_2	1	W Abs.	0.00	0.00	0.1	0.1	76	2.7	10	0.4
	2	W Abs.	0.00	0.00	0.1	0.1	76	2.7	10	0.4
Totals:		**6 Coll.**	**0.03**	**0.02**	**0.8**	**1.0**				

Table 9-6. *A list of all the collimators in the collimation and final-focus system showing the number of σ collimated at each and the contribution to the total collimation budget. The β functions from the lattice shown in Figure 9-33 have been used to calculate beam sizes at each collimator. Geometric wake numbers should be considered to be tentative for parallel-plate tapers.*

The second-stage collimators must be opened up because of the large near-wall wakes for mis-steered beams. The total for the resistive-wall and geometric wakes in the second-stage vertical FD phase is 119 σ'. To this we must consider that the beam could have already been at 30 σ in the IP phase without having been too distorted, hence the aperture must be 150 σ. As we have argued in Section 9.2.4, a kick of 135 σ' would imply a beam sigma product of 4.8 mm^2, which would also insure the survival of the collimator from an impact of a full train. In the horizontal plane the 1st stage total is 9.2 σ'. The aperture has been opened to 15 σ to account for the fact that the beam could already have been close to 5 σ. There is no danger of the beam ending up near these apertures and being steered into collimators in the final-focus system.

Tolerances

The lattice has large β functions and some very large R_{12} and R_{34} values which will lead to important tolerances on quadrupole strength and position stability and on sextupole position stability. Since we are designing near the limit allowed by wakefield intensities, we can also expect important tolerances on collimator jaw stability.

There are four important time domains for tolerance specification:

- capture tolerances,
- long term stability,
- short term stability, and
- jitter tolerances.

Capture tolerances are the absolute alignment or strength tolerances required at start-up so that the system can be aligned and tuned using beam-based techniques.

Long term stability tolerances are those limits that when exceeded would require re-execution of these beam-based alignment strategies.

Several tuning knobs will be activated perhaps every hour at the IP to adjust sensitive aberrations affecting the IP beam spot size. Change in waist and skew aberrations can also be observed in the skew correction system (SCS). Short-term stability tolerances are the tolerances that must be held until tuning knobs are reset or aberrations are rechecked and corrected. We estimate that the SCS scans occur ten times per hour, if required, since this process can be non-invasive.

The beam centroid is stabilized with feedback systems based on orbit measurements and a rule of thumb estimate is that they are effective for times longer than or equal to 15 beam pulses, or about 1/10th of a second. Jitter tolerances refer to requirements on the stability of the system for times shorter than this time.

Except for initial collimator jaw alignment, this section discusses only the stability tolerances associated with the last two time scales.

Tolerance Budgets. The alignment of the beam collision at the IP is maintained with a fast feedback system. As noted above, the jitter tolerances refer to beam-line changes on time scales which can not be corrected by this feedback system.

Machine Section	Steering Budget (H/V) σ	Accumulated Jitter (H/V) σ	Luminosity Loss (H/V) %
To end of linac	0.1 / 0.25	0.10 / 0.25	0.5 / 0.8
Collimation system	0.1 / 0.2	0.14 / 0.32	1.0 / 1.3
w/ amplification		0.18 / 0.40	1.6 / 2.0
Big bend	0.05 / 0.1	0.19 / 0.41	1.8 / 2.1
Final focus	0.1 / 0.2	0.21 / 0.46	2.2 / 2.6
Final doublet	0.1 / 0.2	0.23 / 0.50	2.7 / 3.1

Table 9-7. *A proposal for a jitter budget.*

In addition to limiting luminosity loss, a budget is necessary because with a large beam jitter it becomes difficult to carry out beam-based alignment, wakefield effects are enhanced, and synchrotron radiation in the final doublet is increased. (See Section 11.7). Table 9-7 is a proposal for a jitter budget.

There are many aberrations which must be tuned in the final-focus system using the spot size at the IP as the diagnostic tool (see Table 11-9). Once the aberrations are tuned, changes in the beam line can cause an increase in aberration strength, and that aberration must be re-tuned, or compensated based on an SCS measurement. Several of these aberrations can result from changes in the collimation beam line. These are: horizontal and vertical waist, horizontal and vertical dispersion, and one skew aberration. The collimation system has been allotted 0.5% luminosity change for each of these seven aberrations.

Quadrupole Strength Stability. Each FD-phase section has four quadrupoles at particularly large values of the vertical β function, about 30 km. A small change in the strength of any of these quads would cause a shift of the waist at the IP. On the assumption that changes in the beam size can be measured with a relative resolution of 10%, it follows that each independent aberration can be adjusted so as to leave a residual increase in beam size of only 2%. SLC experience indicates this may be less than 0.5%. The waist position is one of these aberrations, thus a waist-stability budget of 2% must be apportioned to the various modules of the collider. Let us assume that 1/2 of this is assigned to the collimator system, and of that is divided further into 1/2 for quadrupole-strength stability and 1/2 for sextupole-position stability. Hence the quadrupole-stability budget is 1/2%. Assuming that the majority of this can be assigned to the sixteen quadrupoles at large vertical β, and that they are on independent power supplies, it can be estimated that

$$\frac{dk}{k} \leq \frac{1}{60}\,\frac{1}{k\beta} \tag{9.82}$$

For our lattice $k\beta = 1,200$ hence $dk/k < 1.3\ 10^{-5}$.

Based on sensitivity calculations for each element, Table 9-8 assigns strength stability tolerances to all collimation system quadrupoles so that the collimation system meets the allotted 0.5% horizontal and vertical waist budget. We have conservatively included both phases in the list of Table 9-8, hence there are in fact 32 quadrupoles that have been assigned a tolerance of $dk/k < 1\ 10^{-5}$. This could be reduced to 16 with a tolerance of $1.8\ 10^{-5}$.

Sextupole Position. The results of this section are summarized in Table 9-9.

Quad name	Strength Sensitivity (10^{-3})	Sensitivity Tolerance (10^{-3})	Vertical Vibration Sensitivity (10^{-7} m)	Vertical Vibration Tolerance (10^{-7} m)	Horizontal Vibration Sensitivity (10^{-7} m)	Horizontal Vibration Tolerance (10^{-7} m)
Q703	17.00	1.00	1.900	0.100	11.00	0.5
Q704	15.00	1.00	0.810	0.050	113.00	1.0
Q704	15.00	1.00	0.820	0.050	12.00	0.5
Q705	18.00	1.00	16.000	1.000	2.90	0.2
Q705	18.00	1.00	58.000	1.000	2.90	0.2
Q706	11.00	1.00	0.710	0.050	25.00	0.5
Q706	11.00	1.00	0.720	0.050	32.00	0.5
Q707	9.50	1.00	2.800	0.100	5.40	0.5
Q707	9.80	1.00	2.900	0.100	5.40	0.5
Q708	10.00	1.00	4.800	0.300	19.00	1.0
Q708	10.00	1.00	4.700	0.300	19.00	1.0
Q709	6.90	1.00	4.100	0.300	23.00	1.0
Q709	6.90	1.00	3.900	0.300	24.00	1.0
Q710	20.00	1.00	2.200	0.100	76.00	1.0
Q710	20.00	1.00	2.200	0.100	66.00	1.0
QCL1	94.00	1.00	13.000	1.000	230.00	1.0
QCL2	12.00	1.00	16.000	1.000	13.00	0.5
QCL3	0.15	0.01	10.000	1.000	140.00	1.0
QCL4	0.54	0.03	14.000	1.000	34.00	0.5
QCX1	0.18	0.03	16.000	1.000	130.00	1.0
QCX2	0.13	0.01	41.000	1.000	210.00	1.0
QCX2	0.12	0.01	45.000	1.000	220.00	1.0
QCX3	0.11	0.01	310.000	1.000	360.00	1.0
QCX3	0.11	0.01	370.000	1.000	310.00	1.0
QCX2	0.12	0.01	56.000	1.000	42.00	0.5
QCX2	0.14	0.01	49.000	1.000	43.00	0.5
QCX1	0.18	0.01	19.000	1.000	37.00	0.5
QCX1	0.18	0.01	16.000	1.000	130.00	1.0
QCX2	0.13	0.01	41.000	1.000	210.00	1.0
QCX2	0.12	0.01	45.000	1.000	220.00	1.0
QCX3	0.11	0.01	310.000	1.000	360.00	1.0
QCX3	0.11	0.01	370.000	1.000	310.00	1.0
QCX2	0.12	0.01	56.000	1.000	42.00	0.5
QCM1	0.16	0.01	57.000	1.000	50.00	0.5
QCM2	0.23	0.03	24.000	1.000	45.00	0.5
QCM3	5.60	0.10	10.000	1.000	75.00	0.5
QCM4	98.00	1.00	5.600	0.300	37.00	0.5
QCM4	108.00	1.00	6.300	0.300	29.00	0.5
QCM3	7.30	0.10	0.850	0.050	2.00	0.2
QCM2	0.22	0.03	0.120	0.025	0.42	0.05
QCM1	0.15	0.01	0.210	0.030	0.43	0.05

Table 9-8. *The vibration and strength stability sensitivities and tolerances of all the quadrupoles in the collimation system. The sensitivities are calculated as if the one quadrupole was assigned the entire budget of the section. There are about 100 quadrupoles, so in general the tolerance is 1/10th of the sensitivity. Continued ...*

Quad name	Strength Sensitivity (10^{-3})	Sensitivity Tolerance (10^{-3})	Vertical Vibration Sensitivity (10^{-7} m)	Vertical Vibration Tolerance (10^{-7} m)	Horizontal Vibration Sensitivity (10^{-7} m)	Horizontal Vibration Tolerance (10^{-7} m)
QCX2	0.12	0.01	0.170	0.030	0.36	0.05
QCX3	0.11	0.01	0.140	0.025	1.20	0.10
QCX3	0.11	0.01	0.140	0.025	1.20	0.10
QCX2	0.12	0.01	0.180	0.030	0.36	0.05
QCX2	0.14	0.01	0.180	0.030	0.38	0.05
QCX1	0.18	0.01	0.097	0.025	0.36	0.05
QCX1	0.18	0.01	0.097	0.025	0.36	0.05
QCX2	0.13	0.01	0.180	0.030	0.38	0.05
QCX2	0.12	0.01	0.180	0.030	0.36	0.05
QCX3	0.11	0.01	0.140	0.025	1.20	0.10
QCX3	0.11	0.01	0.140	0.025	1.20	0.10
QCX2	0.12	0.01	0.180	0.030	0.36	0.05
QCM1	0.15	0.01	0.210	0.030	0.45	0.05
QCM2	0.23	0.03	0.130	0.025	0.44	0.05
QCM3	5.60	0.10	1.100	0.100	1.80	0.20
QCM4	98.00	1.00	5.800	0.300	35.00	0.50
QCN4	98.00	1.00	4.900	0.300	51.00	0.50
QCN3	11.00	1.00	8.800	0.300	43.00	0.50
QCN2	0.72	0.03	11.000	1.000	44.00	0.50
QCN1	0.47	0.03	24.000	1.000	52.00	0.50
QCX2	0.38	0.03	24.000	1.000	46.00	0.50
QCX3	0.33	0.03	100.000	1.000	1300.00	1.00
QCX3	0.34	0.03	110.000	1.000	710.00	1.00
QCX2	0.38	0.03	35.000	1.000	35.00	0.50
QCX2	0.42	0.03	30.000	1.000	36.00	0.50
QCX1	0.57	0.03	11.000	1.000	29.00	0.50
QCX1	0.57	0.03	8.700	0.300	36.00	0.50
QCX2	0.42	0.03	22.000	1.000	46.00	0.50
QCX2	0.38	0.03	24.000	1.000	46.00	0.50
QCX3	0.33	0.03	100.000	1.000	1300.00	1.00
QCX3	0.34	0.03	110.000	1.000	710.00	1.00
QCX2	0.38	0.03	35.000	1.000	35.00	0.50
QCP1	0.48	0.03	34.000	1.000	40.00	0.50
QCP2	0.75	0.03	14.000	1.000	36.00	0.50
QCP3	9.40	0.10	8.800	0.300	61.00	0.50
QCP4	73.00	1.00	5.800	0.300	47.00	0.50
QCP4	78.00	1.00	6.200	0.300	38.00	0.50
QCP3	11.00	1.00	1.900	0.100	3.10	0.20
QCP2	0.72	0.03	0.220	0.030	0.78	0.10
QCP1	0.47	0.03	0.370	0.030	0.76	0.10

Table 9-8. *Cont.*

Quad name	Strength Sensitivity (10^{-3})	Sensitivity Tolerance (10^{-3})	Vertical Vibration Sensitivity (10^{-7} m)	Vertical Vibration Tolerance (10^{-7} m)	Horizontal Vibration Sensitivity (10^{-7} m)	Horizontal Vibration Tolerance (10^{-7} m)
QCX2	0.38	0.03	0.320	0.010	0.64	0.10
QCX3	0.33	0.03	0.240	0.030	2.10	0.20
QCX3	0.34	0.03	0.240	0.030	2.10	0.20
QCX2	0.38	0.03	0.320	0.030	0.64	0.10
QCX2	0.43	0.03	0.320	0.030	0.68	0.10
QCX1	0.57	0.03	0.170	0.030	0.64	0.10
QCX1	0.57	0.03	0.170	0.030	0.63	0.10
QCX2	0.41	0.03	0.330	0.030	0.67	0.10
QCX2	0.38	0.03	0.320	0.010	0.65	0.10
QCX3	0.33	0.03	0.240	0.030	2.10	0.20
QCX3	0.34	0.03	0.240	0.030	2.10	0.20
QCX2	0.38	0.03	0.320	0.030	0.65	0.10
QCX2	0.43	0.03	0.330	0.030	0.68	0.10
QCX1	0.57	0.03	0.170	0.030	0.65	0.10
QMD1	3.00	0.10	0.490	0.050	1.70	0.20
QMD1	2.20	0.10	0.520	0.050	1.40	0.20
QMD2	0.98	0.10	0.570	0.050	0.90	0.10
QMD2	0.99	0.10	0.560	0.050	0.90	0.10
QMD3	3.60	0.10	0.740	0.050	6.80	0.20
QMD3	3.80	0.10	0.760	0.050	7.50	0.20
QMD4	25.00	1.00	1.100	0.100	5.90	0.20
QMD4	26.00	1.00	1.100	0.100	5.70	0.20

Table 9-8. *Cont.*

- Horizontal Sextupole Position—The calculation of the preceding section can be used to estimate the horizontal position stability of the sextupole since any sextupole motion adds a quadrupole field to the beam line of magnitude $k_S dx$. For a 0.5% contribution to spot size increase the displacement would be limited by the relationship (valid for the FD-phase sextupoles only)

$$k_s dx \leq \frac{1}{10}\,\frac{1}{\beta_y} \tag{9.83}$$

depending on whether one is looking at the vertical waist or horizontal waist.

For the sextupoles of the stage 1 of the FD phase at large $\beta_x = 1.7\ 10^4$ where $k_S = 1.16\,\mathrm{m}^{-2}$, Eq. 9.83 implies $dx \leq 5\,\mu$m. For the sextupoles of the stage 2 of the FD phase at large $\beta_x = 5.3\ 10^3$ where $k_S = 2.6\,\mathrm{m}^{-2}$, Eq. 9.83 implies $dx \leq 7.5\,\mu$m. These four pairs sextupoles contribute to the horizontal waist aberration. Since the quadrupole stability tolerances are mandated by vertical waist considerations, the entire 1/2% horizontal waist aberration budget may be allocated to these four sextupole pairs. If we require the same tolerance for all pairs, the result is $dx < 3\,\mu$m.

For the sextupoles of stage 1 of the FD phase at large, $\beta_y = 4\ 10^4$ where $k_S = 1.5\,\mathrm{m}^{-2}$, Eq. 9.83 implies $dx \leq 1.6\,\mu$m. For the sextupoles of stage 2 of the FD phase at large $\beta_y = 1.3\ 10^4$ where $k_S = 2.8\,\mathrm{m}^{-2}$, Eq. 9.83 implies $dx \leq 2.7\,\mu$m. These sensitivities are based on the vertical waist aberration, for which we have budgets 0.5% for both pairs. If the tolerance of both pairs is taken to be identical, the result is $dx \leq 1.4\,\mu$m.

Beam-line Location	Sextupole Name	Horizontal Sensitivity (μm)	Horizontal Tolerance (μm)	Vertical Sensitivity (μm)	Vertical Tolerance (μm)
V_FD_1	SCY1	1.6	1.4	0.5	0.3
H_FD_1 (2)	SCX1&2	5.0	3.0	1.2	0.4
V_FD_2	SCY4	2.7	1.4	0.8	0.4
H_FD_2 (2)	SCX7&8	7.5	3.0	1.6	0.5

Table 9-9. *Stability sensitivities and tolerances for collimation system sextupole positions.*

The exact meaning of these sextupole-position tolerances must be stated with some care. A change in the position of any quadrupole between large-β_y paired sextupoles that would cause a displacement of the beam at the second sextupole by $1.4\,\mu$m would give rise to the vertical waist aberration. Thus one sees that it is not the absolute position of the sextupole that is of concern, but its position with respect to the sextupole with which it is paired, and the position of this sextupole pair with respect to the beam line as defined by the quadrupoles. For details on stabilization strategies see Section 9.2.6 below.

- Vertical Sextupole Position—A change in the vertical sextupole position gives rise to a skew quad aberration of strength $k_S dy$. For a 0.5% spot size increase we have, for FD-phase sextupoles, the condition

$$k_s dy \leq \frac{1}{10}\sqrt{\frac{\varepsilon_y}{\varepsilon_x}}\,\frac{1}{\sqrt{\beta_x\beta_y}} \tag{9.84}$$

At the $\beta_{y,\max}$ in stage 1 we have $\sqrt{(\beta_x\beta_y)} = 1.710^4$. The resulting 0.5% sensitivity, for $k_s = 1.5\,\mathrm{m}^{-2}$, is $dy \leq 0.5\,\mu$m. At the $\beta_{x,\max}$ in stage 1 we have $\sqrt{(\beta_x\beta_y)} = 0.95\ 10^4$ and $k_s = 1.1m^{-2}$, with a sensitivity $dy \leq 1.2\,\mu$m.

If the 1/2 percent budget is divided with 1/6% going to each of the $\beta_{x,\max}$ sextupoles and 1/3% going to the $\beta_{y,\max}$, we obtain tolerances of $dy \leq 0.7\,\mu$m and $dy \leq 0.4\,\mu$m, respectively.

At the $\beta_{y,\max}$ in stage 2 we have $\sqrt{(\beta_x\beta_y)} = 5.3\ 10^3$. The resulting sensitivity, for $k_s = 2.8\,\mathrm{m}^{-2}$, is $dy \leq 0.8\,\mu$m. At the $\beta_{x,\max}$ in stage 2 we have $\sqrt{(\beta_x\beta_y)} = 3.1\ 10^3$ and $k_s = 2.6\,\mathrm{m}^{-2}$, with a sensitivity $dy \leq 1.6\,\mu$m.

If the 0.5% budget of the collimation system for the principal skew aberration is divided amongst these six sextupole pairs, one possible assignment are the tolerances listed in Table 9-9. We note that the vertical sextupole position tolerance has the same meaning as the horizontal tolerances discussed in the previous section. See Section 9.2.6 for stabilization strategies.

Energy Jitter Considerations. Variations in bunch intensity give rise to variations in energy through beam-loading effects in the linac, hence the energy can vary bunch-to-bunch within a bunch train, and also bunch-train to bunch-train. This variation can be no larger than the band width of the final-focus system, about $\pm 0.4\%$, but we consider here whether such variations give rise to wakes in the collimation system. This jitter is about 1/10th of 4% and hence is 1/10th of the collimation aperture.

By designing the collimation system with a symmetric dispersion function and in such a way that the transverse wake is the same magnitude at the horizontal spoiler and/or absorber at each end of the $-I$s, the energy jitter will produce the same $\Delta x'$ at the second collimator as the first. However because of the $-I$ transform between these locations, the kicks cancel. Thus a properly designed collimation system can be insensitive to energy jitter.

Quadrupole Position. Several quadrupoles between sextupoles have $k_Q R_{12}$ multipliers to the sextupole of 2.2. Thus the tolerances in Table 9-9 must be divided by 2.2 to get the stability tolerance for such quadrupoles.

Jitter of a quadrupole in the FD phase will cause beam jitter at the IP. Using 1/2% of the jitter budget for the collimation system, and assuming that the 8 quadrupoles located at $\beta_{\max}$ points are moving independently, the tolerance on the quadrupole jitter is given by

$$\Delta y < \frac{1}{5}\,\frac{1}{\sqrt{8}}\,\frac{\sigma_{y'}}{k_Q} = \frac{1}{5}\,\frac{1}{\sqrt{8}}\,\frac{\sigma_y}{k_Q \beta_y} \tag{9.85}$$

Since $\sigma_y = 40\,\mu$m, and $k\beta_y = 1,200$, the tolerance on jitter is $\Delta y < 2\,$nm. A similar consideration of the quadrupoles at the β_x maximum leads to a horizontal jitter tolerance of $\Delta x < 2\,$nm. The $k\beta$ is smaller, but there are twice as many quadrupoles and there is no help from disruption. See Table 9-8 for a list of vibration tolerance for all quadrupoles in the collimation system. These vibration tolerances are chosen so that the contribution from all quadrupoles in the collimation system adds up to at most a 0.5% spot size increase.

Note that these vibration tolerances do not apply to seismic ground motion. They can be taken to be the tolerance of the quadrupole vibration with respect to ground beneath it, or to high frequency cultural noise. In the FFTB the vibration between the quadrupole and the ground beneath it is the order of 1 nm, hence the stands and vibration from cooling water in the FFTB meet the requirements of the vibration tolerances of Table 9-8.

The seismic motion, although larger than the tolerances calculated above, is very correlated at low frequencies (smaller than 5 Hz) and the spectrum is small for frequencies above 5 Hz in tunnels below the ground surface. See Appendix C for details on ground motion. Because of the correlation, one must calculate a lattice response function to see the net effect on the IP beam positions. Figure 9-35 shows this lattice response function for the collimator section for the vertical plane. The response function is also discussed in Appendix C. and its application to the final-focus lattice is discussed in Section 11.5.5.

The lattice response function gives the square of the displacement at the IP for a unit amplitude wave of wave number k in the collimation section. At $k > 0.1$ (corresponding to $\lambda < 60\,$m, or with a velocity of 600 m/s at frequencies $f > 10\,$Hz) the response function average is about 0.04. This means if we adopt the IP position requirement as 0.5 nm, the tolerance in the collimation system is 2.5 nm. This number is larger than quiet ground conditions in this frequency region, but care must be taken not to introduce noise of this magnitude. At lower k the tolerance drops off abruptly. At $k = 0.01$ (corresponding to $\lambda < 600\,$m, or with a velocity of 600 m/s a frequency of $f > 1\,$Hz) the response function $G(k)$ is 10^{-5}, corresponding to a tolerance of 160 nm. The integrated ground motion to this frequency is only a few nm, so is well within this limit.

One can fold the quiet spectrum ground motion together with the lattice response function to calculate the relative beam motion at the IP due to the entire spectrum of seismic noise. The result is a beam displacement at the IP that is the order of 0.1 nm for seismic motion in the collimation system.

Dipole Strength Stability. The tightest tolerance on dipoles occurs for dipoles between the vertical spoiler and vertical absorber of stage 1 of the FD-phase collimation. Since the dispersion function at these sextupoles is $\eta = .026\,$m, we may deduce that $\Sigma\theta_i R_{12,i} = 2\eta = 0.052\,$m, where the sum is over the bends between the sextupoles. The tolerance condition may be written as $\Sigma\Delta\theta_i R_{12,i} \leq 1.4\,\mu$m. Since all θ_i are equal, these two relations can be combined to conclude that $\Delta\theta/\theta \leq 2.7\ 10^{-5}$. Using the relation for the two sextupole pairs at the horizontal spoilers and absorbers we have $\Sigma\theta_i R_{12,i} = 0.08\,$m and $\Sigma\Delta\theta_i R_{12,i} \leq 3\,\mu$m, we conclude $\Delta\theta/\theta \leq 3.8\ 10^{-5}$. Since these are different aberrations, the smallest of the two estimates prevails.

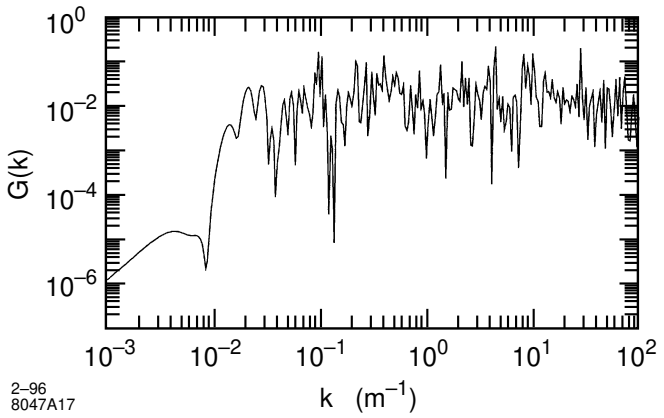

Figure 9-35. *The vertical lattice response function for the 1-TeV-c.m. collimation system.*

Beam Line Location	Dipole Name	$\Sigma\theta_i R_{12,i}$ (cm)	0.02 σ (mm)	Jitter Sens. (10^{-5})	Jitter Toler. (10^{-5})	Stab. Toler. (10^{-5})
Angle Adjust	B2M (2)					N/A
Match In	BCA1 (2)	4	6	15	5	N/A
IP_1	BCA1 (4)	8	6	8	5	N/A
IP→FD	BCM1&2	4/4	6/6	15/15	5	N/A
FD_1	BCA2 (4)	8	6	8	2.7	2.7
FD→IP	BCN1&2	4/2	6/4	15/20	5	N/A
IP_2	BCB1 (4)	4	4	10	5	N/A
IP→FD	BCP1&2	2/2	4/4	20/20	5	N/A
FD_2	BCB2 (4)	4	4	10	4.8	4.8
Match Out	BCB2 (2)	2	4	20	5	N/A

Table 9-10. *Tolerances for the dipoles in the collimation system.*

For comparison, the tolerance for the dipoles of the stage 2 FD phase are $\Delta\theta/\theta \leq 4.8\ 10^{-5}$, the vertical pair ($\Sigma\theta_i R_{12,i} = 0.029$ m, $\Sigma\Delta\theta_i R_{12,i} \leq 1.4$ mm), and $\Delta\theta/\theta \leq 6.7\ 10^{-5}$ for the horizontal pairs ($\Sigma\theta_i R_{12,i} = 0.045$ m, $\Sigma\Delta\theta_i R_{12,i} \leq 3$ mm). The smallest of these will prevail.

The tolerances calculated in the previous two paragraphs are stability tolerances. Beam spray and change of centroid due to beam loss at collimators, would make it very difficult to use beam-based techniques in FD_1. Since these tolerances relate to conditions at the IP, and do not affect collimation system function, they may be monitored and compensated in the skew correction system. Also, see Section 9.2.6.

There are no similar stability implications for the remaining dipoles, and tolerances can be considered as jitter tolerances. The dipoles of the match in and match out would give jitter in the FD phase. The transition-region dipoles between IP and FD can cause jitter in both planes. The dipoles within a stage, can cause jitter at the phase of that stage. The change in position due to a change in angle can be found from the dispersion function change created by the bends. These are listed in column 3 of Table 9-10.

To calculate the tolerances for the remaining dipoles we use the condition that the dipoles should not give rise to detectable beam jitter. Quantitatively we will require that the contribution to jitter by all collimation system dipoles should be less than 0.02 σ (this should be chosen to be negligible compared to expected jitter values). This number, at the location where the dispersion was measured, is given in column 4 of Table 9-10. The sensitivities are the ratios of the dispersion function to the 0.02 σ numbers. These are given in column 5 of Table 9-10.

The sensitivities are equally divided between the two phases. Assuming that the bends in each location listed in Table 9-10 are on the same power supply, and that the errors in the bends at different locations are independent, we arrive at the tolerances listed in column 5.

Collimator Jaw Stability. In this section we investigate the effect of the wake from the two horizontal collimators between the vertical sextupoles on the offset of the beam at the downstream sextupole. Pulse-to-pulse displacement at the downstream sextupole from the wakefield kick must be smaller than the sextupole position tolerance of $dx = 0.3\,\mu$m.

The horizontal collimators are almost π apart in x-phase, hence the beam jitter at the horizontal collimators will give rise to a wake kick of opposite sign. But since the R_{12}s to the vertical sextupoles are the same sign, the net displacement at the vertical sextupole will be zero. In this regard it is important that the two collimators have the same wakefield kick strength.

If one of the jaws moves there will be a net kick of course. Since the wake kick from a 1-σ jitter is less than 0.7 σ' for the sum of all spoilers or absorbers at a given phase, the wakefield from a single collimator for a 1-σ motion will give a kick of about $0.7/4\ \sigma' \approx 0.2\sigma'$. Since 1σ at the horizontal collimators is about 180 μm, the kick will be less than 0.2 (17 nr)=3.4 nr. The displacement at the downstream "vertical" sextupole will be about 0.17 μm.

This consideration also yields the stability tolerance on the collimator jaw of about 320 μm. This is very loose, and corresponds to the absolute alignment tolerance for the jaws which will be calculated next.

If these considerations had been carried out for the vertical collimators the tolerance would be about 1σ, which for the vertical collimation is about 40 μm.

Collimator Jaw Alignment. If the beam passes off-center through a collimator the centroid receives a kick, and also the beam emittance grows slightly. These effects were calculated in Section 9.2.4. For an optimized taper it was shown that the luminosity loss due to emittance growth was 2.3 times smaller than the luminosity loss due to the centroid kicks. When kicks arise because of beam jitter, they all have the same sign, and the luminosity loss goes as the number of collimators squared. When the collimator jaws are misaligned, the kicks will have a random sign, and thus the luminosity loss will grow linearly with the number of collimators. So we can calculate the luminosity loss due to each collimator and then add the effects.

Suppose we assume a 1-σ collimator jaw misalignment. Then the t-ratio for that collimator gives the kick magnitude (in numbers of σ'). The luminosity loss, from emittance growth, due to that collimator will be $0.055(t/t')^2$ (see Eq. 9.40). So the luminosity loss for all collimators at a given phase will be $0.055\Sigma(t/t')_i^2$. For the vertical final-doublet phase (FD_V) this sum is 0.1. Hence a random displacement of the vertical collimators by 1σ would result in a luminosity loss of 1/2%. (Note that the emittance growth which occurs in the IP phase does not effect the luminosity. The growth occurring in this phase effects the angular distribution at the IP.) The horizontal sum is 0.05 so the luminosity loss from a random 1σ horizontal collimator displacement would be 1/8%.

Thus the tolerances on the collimator jaw alignment can be taken to be about 1σ. This would result in a total luminosity loss of 3/4%. See Section 9.2.6 for a discussion of how to achieve this alignment. Also see Section 11.5.5 in Chapter 11.

Particle Tracking and Mapping Studies

Tracking Between Collimator Apertures. In order to insure the passive protection of the collimation system absorbers and the final-focus system collimators, it is essential that they lie in the shadow of the initial collimation system spoilers. Our concern is that the presence of uncompensated sextupoles and chromaticity within the system could lead to unexpected beam offsets at the absorbers and collimators. To check this we have traced particles through the system.

The clearest method we have found to verify this functionality and diagnose any failures is to initialize particles uniformly in an x-x' or y-y' (or both simultaneously) phase space for a fixed energy offset δ. In practice one need consider only negative values of δ, since large positive values of δ can not occur. Figure 9-36 shows the result of such an exercise for the horizontal phase space for an energy off-set of $\delta = -0.02$. The profile is shown at four important horizontal absorbers in the collimation system, and for the first collimator in the final-focus system. Two horizontal absorbers not shown have very large apertures and two are in the stage-2 FD-phase section which we have argued is unnecessary.

We first note that the distributions of Figure 9-36 look like straight lines since the x' range arising from even small α functions is much larger than the internal spread of x' within the bunch. Secondly we note that except for the profile at the final-focus collimator, the distributions fall within the collimated aperture, or in the few exceptions, the apertures can be enlarged to accommodate. The apertures of the absorbers in IP_1 and FD_1 can be enlarged to accommodate the slight beam offsets. They must be set back somewhat to avoid beam that could pass near the spoilers and be deflected into the absorbers. The apertures of FD_2 are not crucial, and can be enlarged, since this phase of collimation could be omitted altogether.

The large offset of the profile at the collimator in the final-focus system was a surprise to us because the profiles tracked in an earlier lattice, that were shown above in Figure 9-6, were not a problem. The analysis of this situation is described in the following paragraph.

Mapping between Collimator System and IP. The results of tracking described in the previous section show that there is a problem with the beam displacement at the first collimator in the final-focus section. The changes between this lattice and an earlier lattice that did not have this problem are: i) a modified big bend without chromatic correction, ii) the addition of a 400-m skew correction section, iii) a new angle adjustment module at the entry to the final-focus system, and iv) an enlarged beta match to the final focus which includes a phase adjustment capability.

To pinpoint the source of the position offset, we created maps [Yan] of each section of the transport line from the collimation system to the final-focus system. Analysis of these maps showed that linear chromaticity and δ^2 dispersion must be corrected. When these terms are corrected, the image falls within the aperture. Figure 9-37 shows the maps for each section and the complete beam line before the chromatic corrections are introduced, and Figure 9-38 shows the situation afterward. The pictures are drawn in a normalized phase space with the IP phase horizontal and the FD phase vertical.

As pointed out, the stage-2 FD-phase collimation is redundant, and can be removed. Then the IP-phase stage-2 collimation will be located between the last FD-phase collimation and the final-focus system and could be used for chromatic correction.

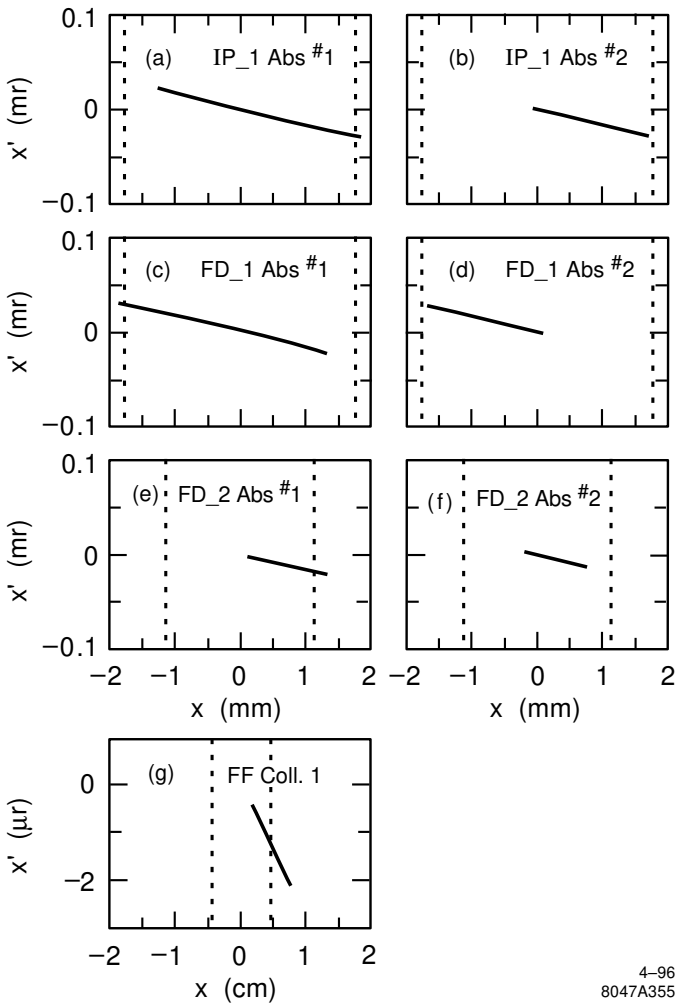

Figure 9-36. *This figure shows the downstream image of particles released at the entrance to the collimation system at $\delta = -0.02$ and on a 6σ square in $x - x'$ phase space. The four pictures are the image at all absorbers in the collimation system and at the collimators in the final-focus system.*

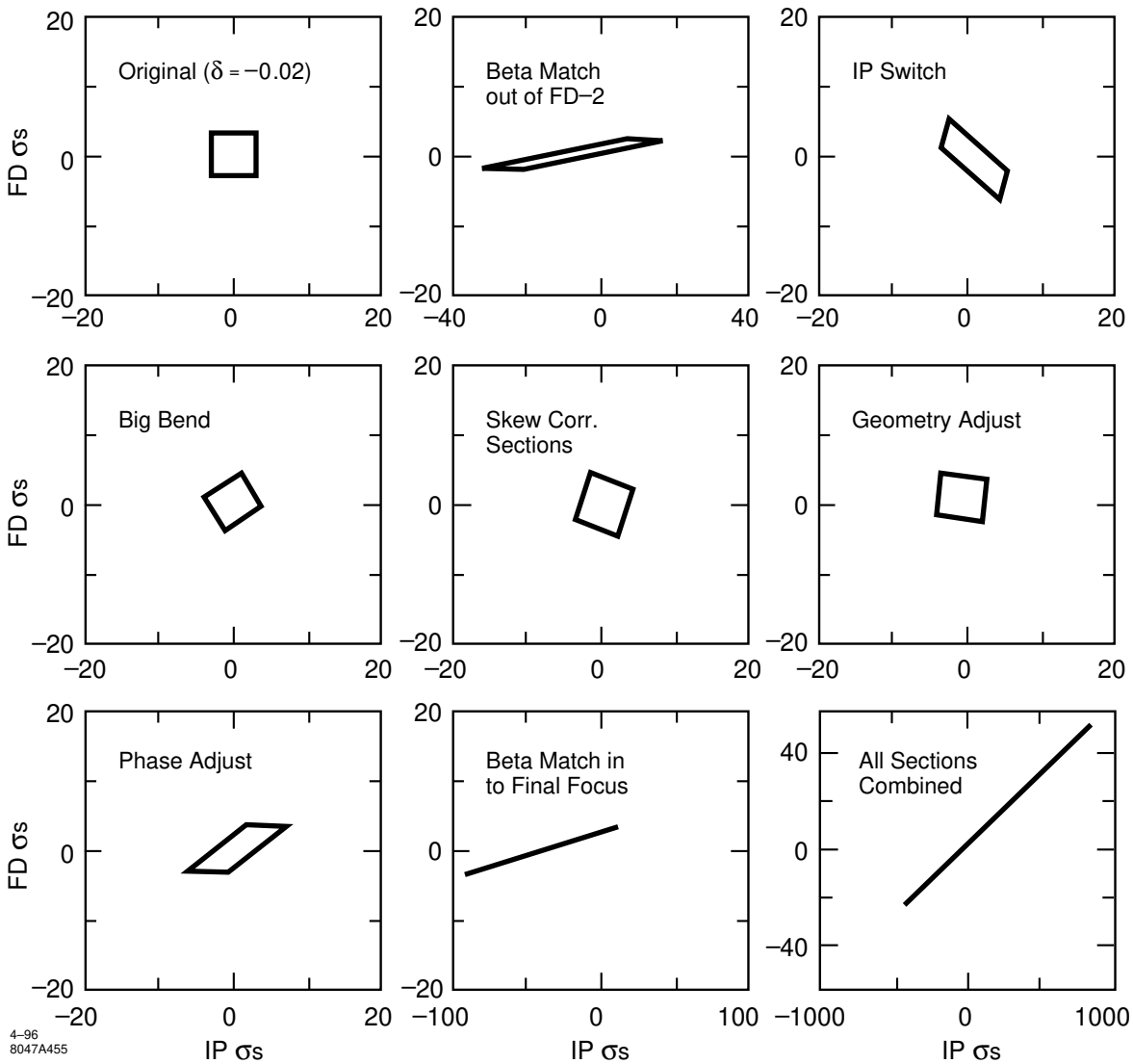

Figure 9-37. *This figure shows a sequence of maps for sections of the beam delivery system. Each picture corresponds to the image of a $3\sigma \times 3\sigma'$ piece of phase space with $\delta = -0.02$. The map is the composition of a linear map from IP to section entrance, then through the section, then a linear map back to the IP. The last picture is a map through all sections.*

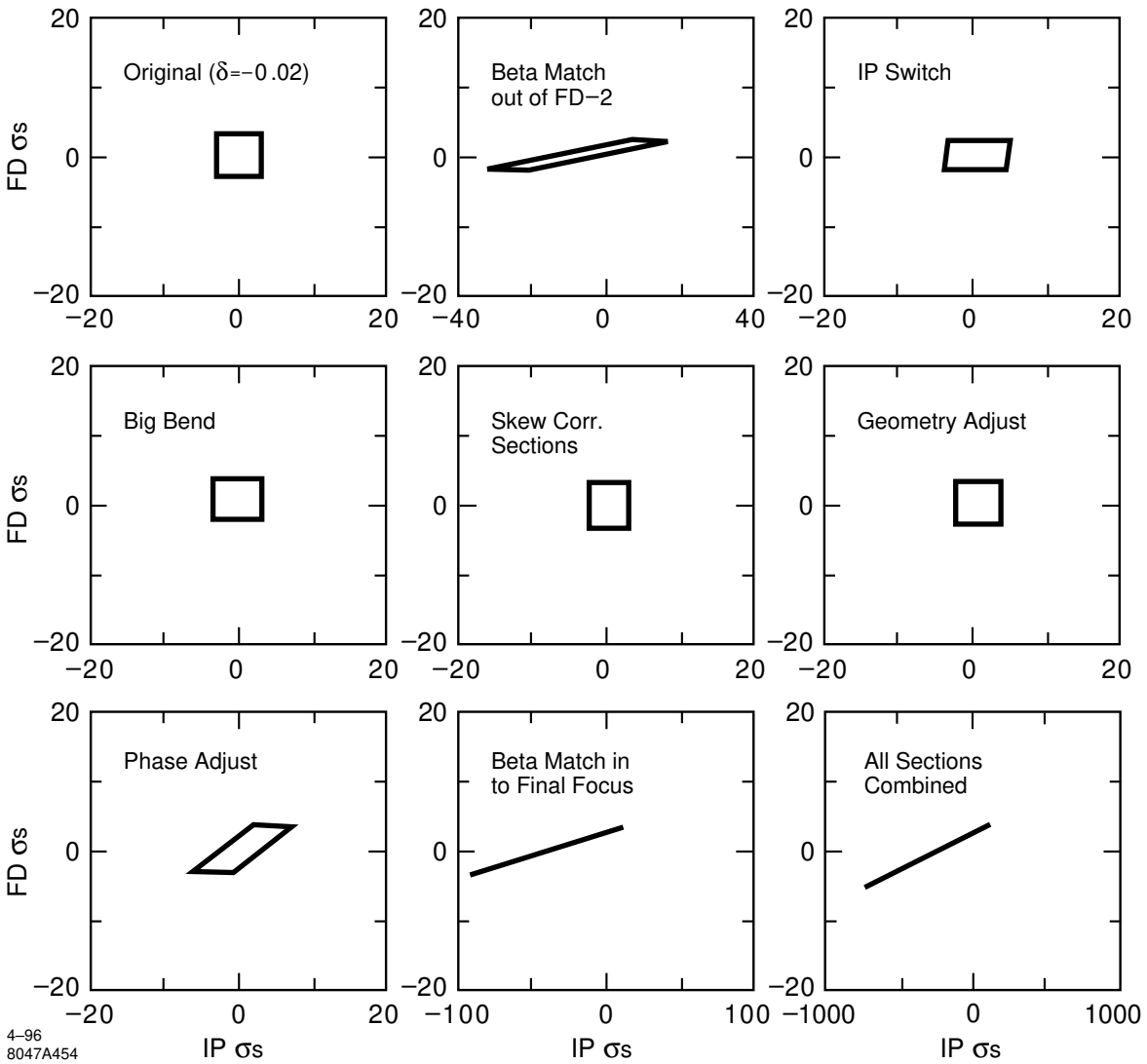

Figure 9-38. *This set of maps is the same as Figure 9-37 with the additional feature that the linear chromaticity and 2nd-order dispersion have been locally corrected. Note the dramatic change in the final map through all sections. (The scale has changed.) The FD phase is now less than 5σ and will pass through the collimator.*

Next-generation lattice. Following up on the mapping studies described in the previous paragraph, we have developed a next-generation lattice that incorporates the following features:

- Removes the FD stage-2 collimation section,
- Inserts sextupoles into the big bend to chromatically fix the big bend,
- Uses the big-bend sextupoles to also compensate the chromaticity of the skew-correction system and the final-focus angle-adjustment module,
- Uses the IP stage 2 sextupoles to compensate the chromaticity of the IP switch,
- Fixes the phase of modules with second-order dispersion so that the dispersion is always in the IP phase,
- Compensate the effects of interleaved sextupoles in the collimation-system modules with octupoles.

This lattice has been tracked and mapped, and has achieved the behavior described in Figure 9-38.

Power Deposition from Spoilers. Figure 9-39 shows the result of tracking particles initialized at the edge of the last spoiler in stage 1 with the angular and energy distributions of Section 9.2.2 [Cai]. We have carried out similar studies for all of the spoilers, and both edges of each. The results of this study show that about 1% of the particles survive to the first section of stage 2, and none hit the beam line after that [Drozhdin 1996].

A study of an earlier but similar beam line is shown in Figure 9-40 [Keller]. This figure shows a section of the beam line corresponding to the first half of one phase of one of the $-I$s in the collimation lattice indicating the placement of absorbers and spoilers. Note the horizontal and vertical scale. The beam pipe aperture is a small slit along the bottom of the frame. The horizontal and vertical spoiler are indicated by h/e and v, respectively, and the corresponding absorbers by H/E and V. Following the first h/e spoiler is a drift length $L = 37\,\mathrm{m}$, then a quadrupole pair with total $k_Q = 0.53$, then a second drift of length 37 m before the absorber H/E. Using the formula of Section 9.2.2 yields $\sqrt{(R_{12}R_{34})} = 55\,\mathrm{m}$. Following the first vertical spoiler (v) is a drift length of 37 m, then a quadrupole pair with $k_Q = .037$, followed by a drift of length 11.6 m, for which $\sqrt{(R_{12}R_{34})} = 43\,\mathrm{m}$. A photon dump will be required in the region of the four bends, indicated in Figure 9-42 by the letter BCXR, and an absorber will be located before QX1.2 as well as QX1.1.

The incident beam was 50 mm from the edge of the spoiler slit h/e_1. The quadrupoles are simulated by 8-cm-radius copper cylinders with a 0.25-cm-radius bore. The four 10-m dipoles were simulated by 5-cm radius copper cylinders with a 0.5-cm radius. The percent energy absorbed is indicated in Table 9-11.

For a 500-GeV beam energy, at 120 Hz, with $0.9\ 10^{12}$ particles per bunch train, the average power in the beam is 8.4 MW. Assuming 1% is incident on a spoiler, downstream absorbers will need to accept a continuous 84 kW of power. The main absorber placed at the end of the second straight section following the spoiler will receive about one-half of this energy, hence it will need to disperse 40 kW of energy. About 20% of the energy exiting the spoiler is in the form of photons. A large number of electrons will pass through the bend and impact absorbers in the second half of the collimation section, or in the $3\pi/2$ section between collimation sections.

Power Deposition from "Virtual" Spoilers. There have been suggestions that it would suffice to have just one stage of collimation, omitting the second IP-stage section. This seems on the face of it improbable

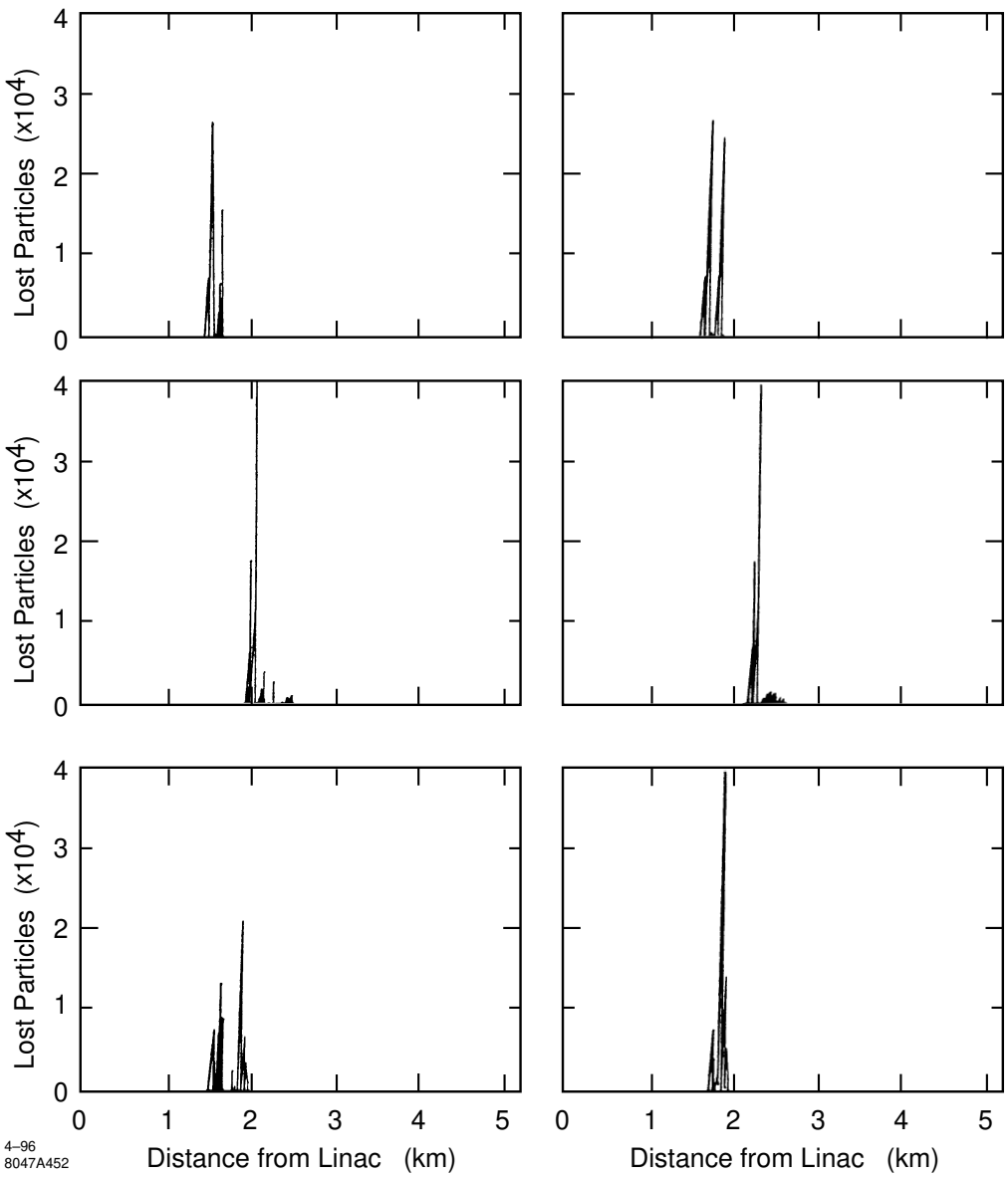

Figure 9-39. *These six pictures show the energy deposition from particles impacting the spoilers in the collimation system. The initial angular and energy distribution correspond to those shown in Figure 9-13–9-14. The six pictures are for the left or top edge of the six spoilers.*

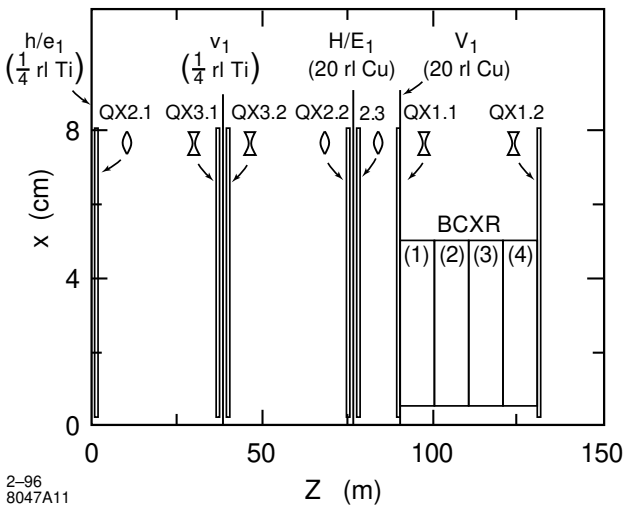

Figure 9-40. *A close-up view of a 150-m section of lattice, starting at the first horizontal spoiler. This physical arrangement was used for an EGS study of energy deposition in the 1-TeV-c.m. collimation system. The results of this study are presented in Table 9-11.*

Element	% Energy Absorbed
QX2.1	0.04
QX3.1	4.0
V1 (0.25 rl Ti)	0.1
QX3.2	1.0
QX2.2	30.1
HE1 (20 rl Cu)	36.0
QX2.3	0.4
QX1.1	0.2
V1 (20 rl Cu)	11.6
Thru V1	16.4

Table 9-11. *Results of an EGS run showing energy deposition downstream from the first spoiler.*

because, according to our assumptions, there are potentially 10^{10} particles impacting the last spoiler. Of these about 2/3 are expected to impact absorbers placed immediately downstream from the spoiler. Indeed tracking shows about 79% hit absorbers in this section. Another 19% are lost in the bend that terminates the dispersion and the beta-match out of the collimation system. That leaves 4 10^8 particles traveling toward the IP with large IP-phase amplitudes. If a particle is off-energy one would expect it to be lost in the bends. But according to the energy distribution of Section 9.2.2, 35% of the particles have an energy loss less than 4%. So many particles have energies near the beam energy, and the majority of the ones that get lost because of low energy are lost at the end of the collimation system. Only 0.5% are lost between the end of the collimation system and the beginning of the final-focus system. 1% are lost in the final-focus system and the remaining 2.5% pass through the IP. Since 1% represents 10^8 particles, this is two orders of magnitude larger than the number which can be collimated in the final-focus system. The only caveat to this statement would be a detector design that could veto 100 muons arriving parallel to the beam line.

Figure 9-41 shows the loss distribution along the beam line from "virtual" spoilers placed at locations in stage 2 where there would be spoilers if this was the only collimation stage [Cai].

9.2.6 Operational Issues

Orbit Stabilization

Changes in waist and skew aberrations that arise from orbit changes within the collimation system can be monitored non-invasively in the skew correction system (SCS) downstream, and corrections introduced. This strategy will relieve the tolerances listed in Table 9-9 in the sense that the stability tolerance can be considered to be for the time between skew and waist checks in the SCS rather than the time between skew and waist scans at the IP. Also the results are intrinsically better since the two beams are not intertwined here as at the IP.

However, it will still be important to occasionally monitor the orbit within the collimation system. This requires BPMs located in these sections. BPM performance will be adversely affected by the presence of intense backgrounds originating primarily from spoilers. Hence the BPMs must be carefully protected from the spray originating at the spoilers, or from any secondary particles that might be generated by this spray.

One can take advantage of the fact that the number of bunches in the beam-train and the emittance of a single bunch can be changed rapidly (a criteria that is important for the machine protection systems). If the collimators are designed so that they can be withdrawn rapidly, then the beam could be reduced to a single small-emittance bunch and the beam trajectory can be observed without the presence of spray and offsets due to beam loss. We note that it takes an acceleration of 2 10^{-3} g, where g is the acceleration of gravity, to move an object 5 mm in 1 second, with an original and final velocity equal to zero. The concern is that the collimator alignment accuracy not suffer in this process. Collimator alignment tolerances are typically 100 μm horizontally and 40 μm vertically, so this may not be a problem.

BPM Protection

Even with a single bunch it is important to protect and shield the BPMs. Because of their small length, and high resolution, and with an inner diameter that is twice the size of the quadrupole bore, the rf BPM [Shintake 1995] tested in the December 95 FFTB run should be easy to protect. One should choose the recess of the BPM and the shape of the protection collimator in such a way that particles could not reach or

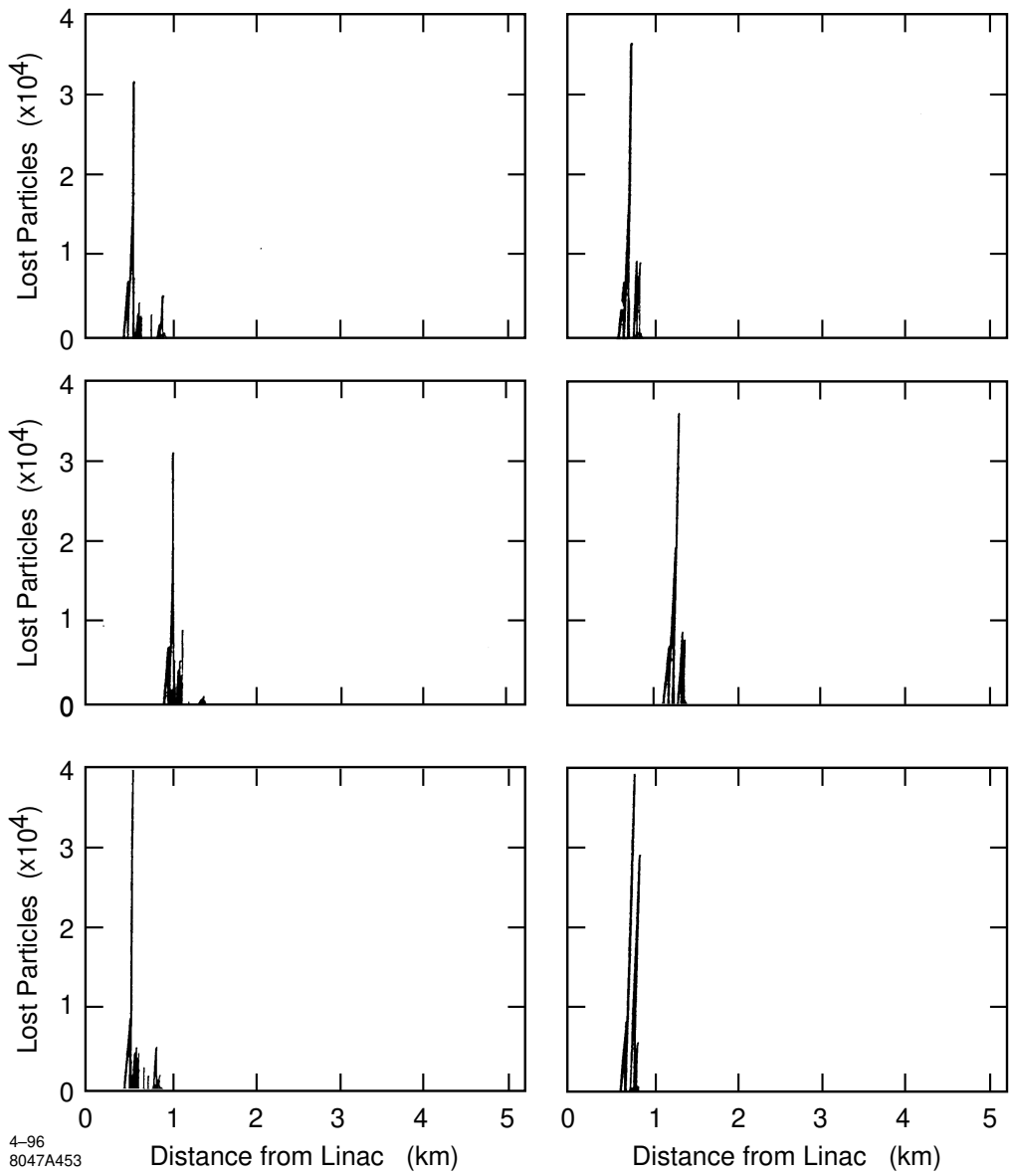

Figure 9-41. *These six pictures show the energy deposition from particles impacting "virtual" spoilers in stage 2 of the collimation system. The intent is to explore the consequences of having only 1 stage of collimation.*

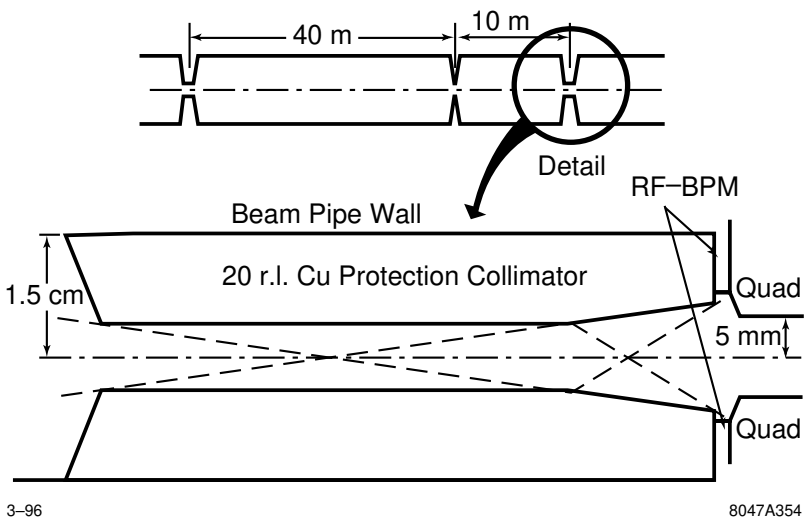

Figure 9-42. *A conceptual sketch of a possible protection collimator for BPMs of the collimation system.*

influence the BPM with a two-surface process (that is the beam would have to scatter or create a secondary electron at two distinct surface before reaching the BPM). The rf BPMs tested in the FFTB had an inner radius of 10 mm, and a resolution of 40 nm. Figure 9-42 shows a conceptual sketch of a protection collimator for a recessed rf BPM with an inner radius of 8 mm. This sketch is only intended to be suggestive, and does not represent a design. Research with rf BPMs has been very promising. It will be important to do studies of spray protection geometries to determine their effectiveness.

System Alignment

Magnet Alignment. It is presumed that all magnetic elements will be located on movers similar to the type used in the FFTB. These have step sizes of $1/3\,\mu$m with a total range of 1 mm. If the magnets are originally aligned to say $250\,\mu$m it is a straightforward task to align the magnets to tens of micrometers using beam-based techniques that rely on changing the current in each magnet. Such techniques were employed successfully in the FFTB.

Collimator Jaw Alignment. Collimator jaws can be aligned by changing the separation of the jaws while keeping the mid point between jaws fixed, and observing any centroid disturbance of the beam. As clarified in Section 9.2.5, the tolerance on collimator position is about 1 σ. For most collimators a 1-σ beam displacement produces about a 0.1-σ kick. In the first stages of the collimation system, with the large R_{12}s and R_{34}s to downstream stages, it is easy to detect these 0.1-σ kicks. Vertically 0.1 σ can be $4\,\mu$m, horizontally it is $30\,\mu$m. This will be detectable with the contemplated BPMs.

In the last stage of the collimation system this is more difficult. The typical beta functions in the big bend and skew correction system are 40 m, hence 0.1 σ is be $1.4\,\mu$m horizontally and $0.14\,\mu$m vertically. The former could be detected with an FFTB type strip line BPM. The latter could be detected with the rf BPM that has been tested. In principle there is no problem detecting these orbit changes. One has the additional advantage that one can observe the trajectory through the entire remaining beam delivery system, so there is a lot of redundancy.

The alignment of the final-focus system collimator is more sensitive yet. Here the maximum R_{34} to a downstream BPM will be much smaller, say 200 m. A 0.1-σ kick at the CCY collimators has a magnitude of 0.05 nr, and the downstream displacement will be 10 nm. It is expected that this tolerance can be achieved with an rf BPM since the first efforts resulted in a 40-nm resolution. This BPM would have to be placed at an optimum location in the final telescope.

We note that if the beam has a slight banana shape as a result of upstream wakes, this collimation alignment technique will be weighted to the head of the bunch, since the head is causing the wake on the tail. Any result coming from the banana part of the bunch would tend to move the collimator in the direction of the bunch. This will have the effect of causing a kick to the tail in the direction opposite to the banana tail. In a phase space diagram this kick is perpendicular to the tail in phase space.

Tuning and Stabilization

Since the IP-phase quadrupoles are in phase with the IP they have little effect on the IP beam size, hence the tolerances of the two stages of IP-phase collimation are much looser than the tolerances on the FD-phase collimation, and so we shall concentrate on the FD phases. Furthermore, stage 2 of the FD-phase collimation is optional, since the beam has been already well collimated by previous stages, and since the β functions are smaller, the tolerances are looser than stage 1. Thus we can focus our attention on stage 1 of the FD-phase collimation. We will assume that the BPMs have the required resolution and have been protected from spray.

There are five quadrupoles in each of two sections of this stage. Each section is separated from the other by π phase advance. The first section has one horizontal spoiler and one vertical spoiler; the second section has one horizontal spoiler. If we assume that 1% of the beam is indeed intercepted at the spoilers, then since their gaps are about 2 mm, a change in the beam centroid of 20 μm can occur. Since the tolerance on the centroid position at the sextupole located next to the vertical spoiler is about 0.4 μm, we must determine the vertical centroid to a factor of 50 better than the change due to beam scraping. Thus stabilization to maintain the tolerances of Section 9.2.4 is not possible when the beams are being collimated to this extent.

As mentioned above, either the aberrations caused by a change in the collimation system orbit can be measured out and compensated in the skew correction section, or the collimators can be withdrawn after reducing the train to a single bunch. In the latter case methods similar to those described in Section 11.5.6.

Another strategy is to insure that the elements (strengths and positions) of the beam line are stable without any intervention. This is always a good course of action if possible. This strategy is greatly enhanced by the ability to non-invasively monitor the waist and skew aberration in the skew correction system (SCS) which follows the big bend. In this case the required stability times is a fraction of an hour rather than an hour. The stability tolerances on the bends are all a few times 10^{-5} which is achievable and should not cause a problem. The smallest vertical beam position tolerance at the sextupole is 0.3 μm, which could result from the motion of a quadrupole by abut 0.1 μm. Recent FFTB measurements show a beam-line element motion of about 0.1 μm per hour, which would suggest a drift of less than 10 nm in a six-minute stability time [Assman]. The FFTB measurements require further analysis and a model development to extrapolate to longer beam-line lengths. Since the FFTB line is located in a concrete block structure in the research yard at SLAC, not 20 m underground in an environment that should be thermally more stable, it appears we can achieve the required stability without intervention. (Recall that the tolerances were based on 1/2% luminosity loss for the skew and waist aberrations from the entire collimation system.)

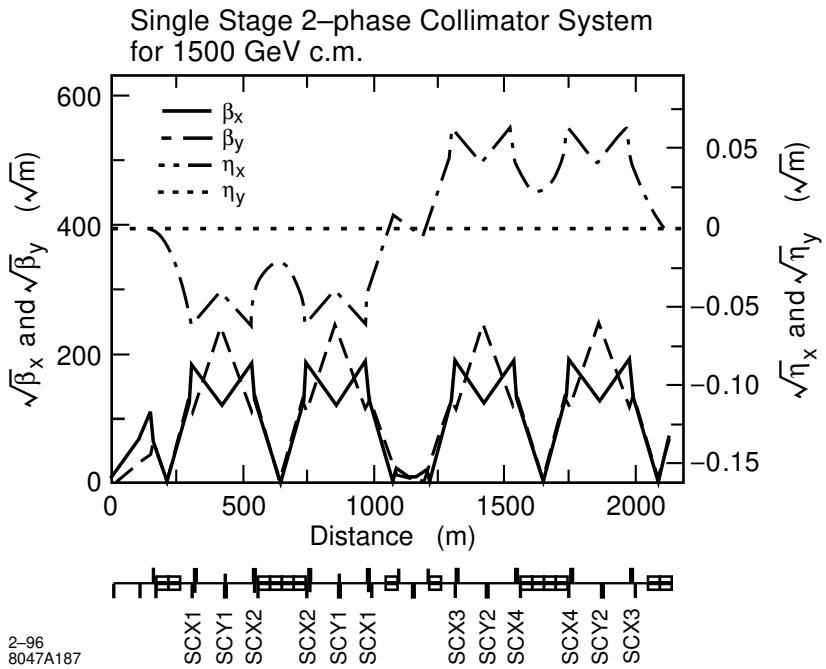

Figure 9-43. *The lattice functions for a 1.5-TeV-c.m. collimation system.*

9.2.7 Energy Scaling Laws

As we indicated in Section 9.2.4 the $\overline{n}$ are independent of energy, and since the equation for the gap is independent of energy, so is g_0. It follows that the spot sizes at the collimators are independent of energy but that β_0 must increase linearly with energy. Since energy deposition at the surface of a collimator is independent of energy, the requirements of beam-size to insure spoiler survival remain the same.

According to this scaling the beam divergence at the spoilers will scale as $\sqrt{(\varepsilon/\beta)} \sim 1/\gamma$. But the rms angle in the multiple scattering formula also varies as $1/E$, so the scattering angle to beam divergence ratios remain unchanged. Thus many of the considerations of particle counts we have presented in Section 9.2.3 above remain unchanged.

A Collimation System for 1.5-TeV c.m.

A lattice for a 1.5-TeV-c.m. system is shown in Figure 9-43. This lattice was designed so that the horizontal and vertical planes could be collimated at the same location, where the vertical β-function is a maximum. At this energy, collimating each phase one time requires a beam-line length of 2 km. As described in the text, the optimum system will have 2 IP phases and 1 FD phase of collimation. The second IP phases can have a smaller β-function. If more beam-line length is required we can extend the collimation system in to the linac tunnel.

Figure 9-44 shows the band pass and emittance growth for this lattice. Both are satisfactory.

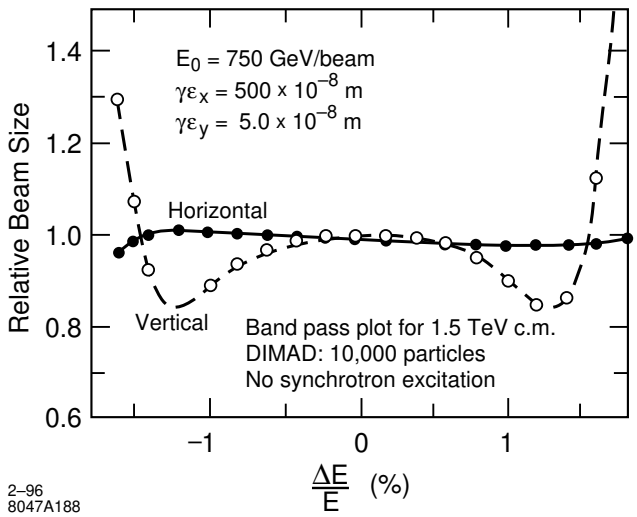

Figure 9-44. *The band pass plot for the 1.5-TeV-c.m. collimation system.*

9.2.8 Nonlinear Collimation Systems

Nonlinear collimation systems were proposed by Merminga *et al.,* [Merminga 1992] and described in several papers. The collimation system proposed for the JLC was also nonlinear and described in the JLC report [Oide]. It had a new interesting feature that the horizontal and vertical planes were collimated at the same time. Before beginning the design and analysis of the linear collimation system described here we assessed the results of these papers. We were impressed that the lengths of the nonlinear systems were not obviously shorter, and either the sextupoles were impossibly strong, or the beta functions were as large as linear system beta functions. This led us the conclusion that it would be best to begin with the more conservative linear system, pursue an optimization of that design, calculate its tolerances and assess its operational behavior, and then return to the nonlinear system for a comparison.

Now that the linear design has reached some maturity, it is appropriate to turn to the nonlinear systems, or to a combination of linear and nonlinear designs, and carry out the above intentions. Unfortunately that has not been completed.

9.2.9 Summary and Conclusions

We have described the specifications, discussed the relevant properties of materials, presented spoiler and edge-scattering distributions, clarified the relevant wake-field of tapered collimators and defined the optimum choice of collimator shape, quantified the impact of near-wall wakes for on-axis and mis-steered beam, designed lattices that implement the required functionality, calculated the position and strength tolerances of the magnetic elements, clarified the impact of ground motion, tracked the lattices to confirm their functionality, tracked spoiler distributions in the collimation system to determine power deposition, traced edge-scattered distribution in the final-focus system to determine the probability of particle impacts on the final doublet, determined the extent of tail repopulation due to gas scattering, discussed the operations problems, and addressed machine protection issues. To our knowledge all issues have been addressed with

the satisfactory conclusion that it is possible to build and operate a collimation system for the proposed beam parameters from beam energies of 175 GeV to 750 GeV, that will collimate the beam at apertures that are required by the final-focus system and final-doublet apertures. We are confident that we have an existence proof. However the systems are long and they are sensitive.

Because of the system length and its delicate nature, we feel that further research is warranted in four directions:

1. As the machine protection system (MPS) is better determined and clarified, it may evolve that the passive protection requirement we have assumed is not warranted by the magnitude of additional risk avoided. The second level of the MPS already requires careful monitoring of all system changes and limiting the range of change that can occur in fast systems. At the present moment the only fast change, which to our knowledge can occur upstream of the collimation system, is the sudden dropping of klystron families, resulting in a sudden large energy change. This is a special kind of change that must already be addressed in the linac beam diagnostic sections (chicanes). If the requirement of passive collimator protection were dropped, the collimation system would become much shorter and less delicate.

   It would be also worthwhile to better determine the worst-case tail population expected from the linac. Is it larger or smaller than the number we have assumed? This does not alter the lattice design, but does impact the power that must be handled by the absorbers.

2. Experiments should be carried out to verify the wakes of tapered collimators.

3. Nonlinear systems and combinations of linear with nonlinear systems should be studied. It is time to search for the "optimum" collimation system.

4. Improvements in the present system should be pursued, including a redesign to meet recent beam parameter changes.

5. Finally, non-conventional collimation ideas should be pursued. Though they have been discussed, it would be a worthwhile study to clarify the impracticality of all wild ideas, with the hope that one will actually survive.

9.3 Pre-Linac Collimation

The pre-linac collimation system is intended to remove the low energy, 10-GeV, contribution to the beam halo produced from the electron/positron source, damping ring, pre- accelerator and bunch compressor. The pre-linac collimation system should be able to collimate continuously 1% of the beam, 10^{10} particles, at the IP and FD phase in both planes and must withstand one full mis-steered bunch-train. Using simple energy scaling laws the post-linac collimation-system design can be scaled to produce the pre-linac design. There are some differences based on requirements for the dispersion function, and with synchrotron radiation in dipoles.

9.3.1 Pre-Linac Collimation Function:

Halo particles before the main linac are present upon extraction from the damping ring and generated in the bunch compressor. If not removed this low energy halo will be injected into the main linac and accelerated

up to full energy. By placing a collimation system at the entrance to the main linac the amount of this low-energy halo accelerated to full energy will be minimized easing the load on the final collimation system, and reducing potential background in the IR region. The strategy used to achieve the needed passive protection is "spoiler followed by absorber." The spoilers will be constructed of titanium. The spoilers function is to increase the angular divergence of an accidentally mis-steered beam so that it can be intercepted by the downstream copper absorbers.

9.3.2 Pre-Linac Collimation System Requirements:

To match the post-linac specifications, the beta functions at the collimators must collimate at a depth of 6 σ_x, and 35 σ_y. The collimator jaw gap is determined by two conditions. The first is the spoiler survivability which requires that $\sqrt{(\sigma_x \sigma_y)} \leq 100\,\mu$m so that the spoiler does not exceed its tensile strength and break due to thermal expansion. The second condition on the jaw gap is determined from minimizing the wakefields induced by the collimator jaws. The equation for the optimal collimator jaw gap is independent of energy so the optimum pre-linac collimation jaw gap will be the same as the post-linac gap, approximately 1 mm.

In order for the spoilers to survive it is required that the thermal stress created by the temperature rise remain below the tensile limit of the spoiler for one mis-steered bunch train. A titanium alloy has been found to offer the best performance and it can be coated with pure titanium or titanium nitride to reduce resistive-wall wakefield effects. Following the arguments for the temperature rise and tensile strength requirements for the post-linac collimation system one can scale the results for the pre-linac collimation system. The energy deposition at the surface of a material is independent of energy above 1 GeV, hence the instantaneous heat load at 10 GeV is the same as 500 GeV. The heat load in the absorber however will simply decrease from 84 kW to 1.7 kW due to the fact that the beam has less energy to deposit. Hence the spoiler material and thickness remain the same as the 500-GeV design and the absorber design can be relaxed.

The beam divergence varies as $1/\gamma$ and the rms multiple scattering angles also vary as $1/\gamma$, thus the ratio of scattering angles to beam divergence remain constant. The energy scaling laws show that much of the previous work done on the post-linac collimation system can simply be carried over for the pre-linac collimation system. A detailed discussion of heat loads, multiple scattering, absorber properties, spoiler transmission, wakefield tolerances, etc., can be found in the post-linac Section 9.2 Energy scaling is specifically discussed in Section 9.2.7.

9.3.3 Pre-Linac Collimation Optical Design:

The optical design follows the post linac design utilizing an interleaving of the horizontal and vertical scraping to minimize the collimation section length. The beam is collimated at the IP and FD phase in both planes one time. Using the constraint $\sqrt{(\sigma_x \sigma_y)} \leq 100$ mm for spoiler survival the beta functions at the design emittances must satisfy the condition $\sqrt{(\beta_x \beta_y)} \leq 80$ m at 10 GeV. Figure 9-45 shows a 10-GeV lattice which satisfies these conditions. The spoiler and absorber gaps are about 1 mm. There are two subsections each having a set of horizontal and vertical spoilers and absorbers each separated by $-I$ transformations. The two subsections are separated by a $5\pi/2$ transform.

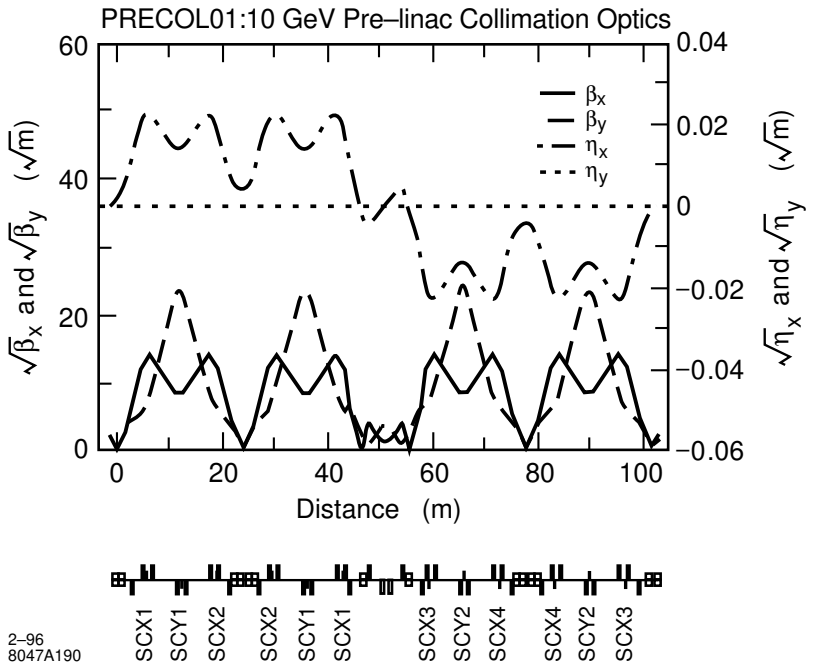

Figure 9-45. *The pre-linac collimation system lattice.*

9.3.4 Pre-Linac Collimation System Bandwidth

The pre-linac collimation system bandwidth is shown in Figure 9-46. Though it is larger than the post-linac bandwidth, the energy spread at the beginning of the linac is quite large because of the second bunch compressor. The bandwidth should be three times this large. This problem must be addressed, either by attempting to design a collimation system with 4.5% bandwidth or locating the collimation system downstream in the linac after the energy spread is reduced. The latter option, though seemingly attractive, has the problem that the first 600 m (to 30 GeV) of the linac is used to induce a coherent energy spread to facilitate BNS damping in the linac. Hence at 30 GeV the energy spread is still 1.5%, and it would be necessary to place the collimation system at 90 GeV. This is nine times the energy of the existing design, so the system would have to be redesigned for that energy. Since pre-linac collimation is optional we have not investigated this subject further.

9.3.5 Summary

We haved presented a design for an optional 10-GeV pre-linac collimation system. This system is a scaled-down version of the 500-GeV post-linac collimation system. The beta functions were scaled so that the spoiler survival criteria of $\sqrt{(\sigma_x \sigma_y)} \leq 100\,\mu$m, a 1% beam halo collimation, and a minimal wakefield condition are satisfied. The system uses the same quadrupole magnet design as the post-linac system and its length is 100 m. The design presented has a bandwidth of 1.5% which is too small to be located immediately after the bunch compressor. If pre-linac collimation is deemed necessary this system will need to be improved upon.

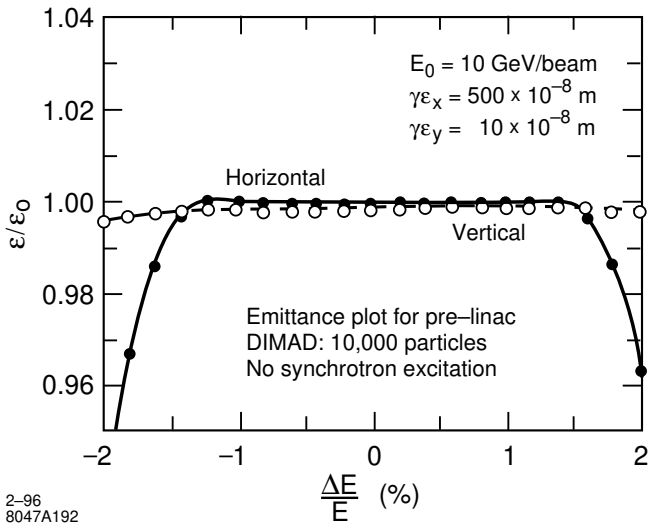

Figure 9-46. *The pre-linac emittance growth.*

9.4 Bunch Length Collimation

9.4.1 Introduction

In order to achieve high luminosity, the NLC requires very short bunches. The three primary considerations that determine the bunch length are: the bunch length should not be much larger than β_y^*, the emittance growth due to the transverse wakefields increases with the bunch length, and the energy spread due to the longitudinal wakefield decreases with increasing bunch length. For the NLC parameters, the optimal bunch length is between 100 and 200 μm.

When generating these bunches in the bunch compressors, one typically populates long bunch length tails. These tails will be deflected to large transverse amplitudes by the transverse wakefields. In addition, the long longitudinal tails will be converted into energy spread as they go through the main linac. In the post-linac collimation system and the final-focus system, the energy tails will generate transverse halo due to chromatic effects. Both sources of transverse tails will create unacceptable backgrounds in the detector if not collimated. Therefore, the longitudinal tails have to be collimated before entering the final focus. It is better, and presumably easier, to collimate them before the main linac.

For these reasons we decided to design a bunch length collimation system for the NLC. The system should be located before or at the beginning of the NLC main linac, and remove particles beyond $3\sigma_z$. The usual method to cut longitudinal tails is to convert them to transverse tails and remove them with a collimator. The ideal case is when the bunch length has a monotonic energy distribution. Then the energy spread can be transferred into horizontal displacement with dispersion.

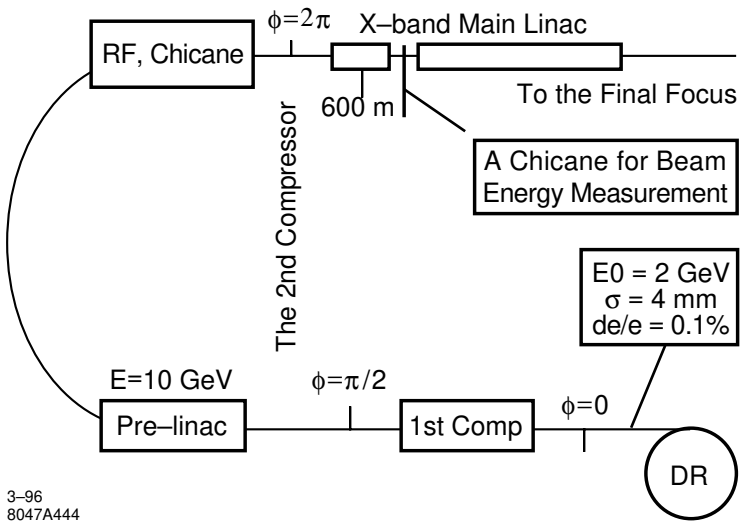

Figure 9-47. *The layout of the NLC.*

9.4.2 Collimator location

Figure 9-47 is the layout of the damping ring to the final focus of the NLC, showing the damping ring, two steps of bunch compression and the X-band main linac.

The longitudinal phase $\Phi = n\pi$ is the necessary phase to place the collimator. Hence we may choose the first collimation at the exit of the damping ring. Here, the energy spread is small (0.1%), and for $3\sigma_z$ bunch length collimation, it will need to cut beyond $+/-0.3\%\Delta E/E$. Assuming the collimator half gap equals 1.5 mm and $\sigma_e/E = 0.1\%$, then a dispersion $\eta = 0.5$ m is needed. Since there is already a spin rotation system at this location, the 0.5-m dispersion is available.

A second bunch-length collimation could be put after the second bunch compressor. Due to the space limitation, we choose to put this collimator after the first 600 m of acceleration in the X-band main linac, where there is a chicane for beam energy measurement.

9.4.3 Particles Loss at Bunch Length Collimators

We put the two bunch length collimation systems into the present two-step compression system and the main-linac lattice design. Table 9-12 presents the expected particle loss at the collimators with a cut at $2\sigma_e$ [Raubenheimer 1994, Zimmermann].

The following figures show the bunch shape at the end of the main linac as calculated by a modification of the LITRACK program [Bane].

Collimation location	Beam loss %
1st collimation only	4%
2nd collimation only	2%
1st and 2nd together	5%

Table 9-12. *Particles loss percentage at the collimation systems.*

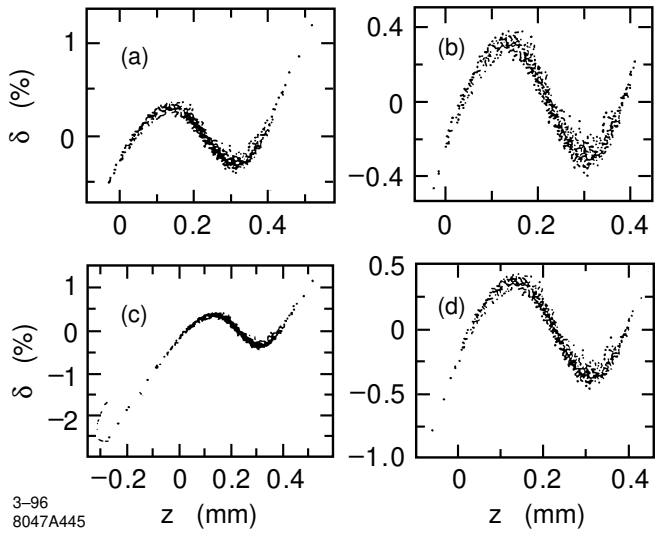

Figure 9-48. *(a) The bunch shape without collimation. (b) The bunch shape with the first collimation only. (c) The bunch shape with the second collimation only. (d) The bunch shape with both bunch length collimation systems.*

9.4.4 Collimation in the Linac

It is important to have the beam energy be longitudinally monotonic, so that the bunch length collimation can be made by energy tail cuts. To meet the above requirement, we can put the beam behind the rf crest, so that only 10% of the particles are beyond $4\sigma_z$ and have energy deviation greater than $4\sigma_\epsilon$. For a collimator half gap equal 750 μm, and $\sigma_\epsilon/E = 1\%$, a dispersion of $\eta = 2.5$ cm implements a $+/-3\sigma_\epsilon$ energy tail cut.

At the beginning of the main linac, the beam bunch length is 100 μm. The energy distribution may be calculated with the formula:

$$E(z) = E_0(z) + V_{\rm rf}\cos(\Phi_0 + kz) - \int W_L(z'-z)\rho(z')dz' \quad . \tag{9.86}$$

Here $E_0(z)$, is the initial energy distribution at the beginning of the main linac, with $< E_0(z) >= 10$ GeV. $V_{\rm rf}$ is the main linac rf peak voltage. Φ_0 is the center particles' accelerating phase, and k is the wave number of the rf wave form. $W_L(z'-z)$ is the main X-band linac longitudinal wakefield, which has been calculated by K. Bane. $\rho(z')$ is longitudinal distribution, which we will assume to be Gaussian. The minus sign indicates beam energy loss.

For the three NLC designs, when $\Phi = 16°$ behind the crest of the rf phase is chosen, the beam energy spreads are about 1%. If we set the collimator to cut $+/-2\sigma_e$ (*i.e.*, $+/-2\%$), less than 10% particles will be cut.

	NLC-I	NLC-II	NLC-III
Rf phase	16°	16°	16°
Energy gain	33 MV/ m	55 MV/ m	70 MV/ m
In 600 m	20 GeV	33 GeV	42 GeV
# of particles	$7\ 10^9$	$11\ 10^9$	$14\ 10^9$
Energy spread	1.0%	1.2%	1.28%
# of particles	$1.54\ 10^8$	$3.30\ 10^8$	$7.84\ 10^8$
(%) Cut	(2.2%)	(3.0%)	(5.6%)

Table 9-13. *Some parameters for the three NLC design energies.*

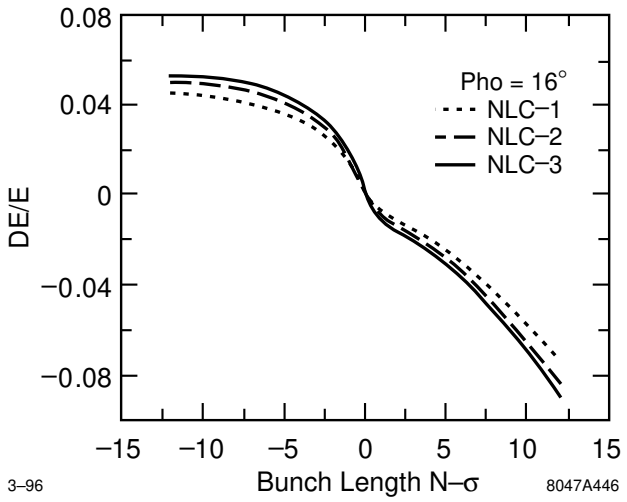

Figure 9-49. *Energy distributions for the three NLC design phases.*

Table 9-13 lists some parameters and percentages of particles that are lost at the collimators. Figure 9-49 shows the energy distribution along the bunch.

9.4.5 Conclusion and Discussion

It is possible to have two bunch-length collimation systems in the NLC design lattice. The bunch has a nearly monotonic energy distribution when we choose the rf phase to be 16° behind the rf crest for all three NLC design phases. The energy spreads are about 1%. If we decide to collimate $+/-2\sigma_e$ energy tails, there will be less than 10% of particles cut.

Before determining the utility of the collimators, a number of additional questions remain to be answered. In particular, we need to study the longitudinal and transverse wakefields induced by the collimators and related tolerances.

Our results show that the collimator at the exit of the damping ring is relatively straightforward and effective. Because of a non-linear $\delta - z$ relationship, and therefore a nonlinear $x - z$ dependence at the collimator, the second collimation is more difficult and less beneficial.

References

[Assman] R. Assman and C. Montag have studied quadrupole motion in the FFTB using the DESY wire system. Data analysis is in process.

[Bane] K. Bane wrote the program LITRACK (1994). Undocumented.

[Brown 1979] K. Brown and R. Servranckx, "Chromatic Corrections for Large Storage Rings", SLAC–PUB–2270, in *IEEE Trans. Nucl. Sci.* **26**, 3598 (1979).

[Cai] Y. Cai performed the tracking studies for this chapter using a C++ mapping and tracking code he has written called LEGO.

[Chao 1992] A. Chao, "Coherent instabilities of relativistic bunched beam", SLAC–PUB–2946 (1982).

[DeStaebler-Walz] Spoilers followed by absorbers have been in use for many years at the Stanford linac.

[DeStaebler 1994] H. De Staebler first pointed this out to us. Private communication.

[Drozhdin 1996] A. Drozhdin and N. Mokhov, "NLC-1000 Beam Collimation System Simulation", Jan. 18, 1996. The authors have prepared distributions similar to those presented in the text generated by Y. Cai. We thank them for supplying us with a preprint of this study they did of the NLC collimation system.

[FFTB BPMs] The FFTB strip line BPMs have a resolution of 1 mm. The stability of the zero point has not yet been determined. According to S. Smith the one-hour stability could conceivably be a factor of ten better than the resolution. A proposal has been submitted to study the zero point drift of these BPMs.

[Helm] All of the collimation lattices have been prepared by R. Helm. Lattice angle control was studied by Y. Nosochkov.

[Irwin 1991] J. Irwin, N. Merminga, R. Helm, and R. Ruth, "Optimizing a Nonlinear Collimation System for Future Linear Colliders", SLAC–PUB–5507, in *Proc. 1991 Part. Acc. Conf.* (1991).

[Keller] L. Keller provided this tracking study.

[Merminga 1992] N. Merminga, R. Helm, J. Irwin, and R. Ruth, *Particle Acclerators* (1992).

[Nelson 1993] R. Nelson has provided the EGS simulations described in this chapter. See The EGS Code System, SLAC–PUB–265 (1985).

[Oide] JLC collimation system, Section 4.8.6, "JLC-I", KEK Report 92–16 (1992).

[Piwinski] A. Piwinski, "Wake Fields and Ohmic Losses in Flat Vacuum Chambers", DESY–HERA–92–04 (1992).

[Rossi 1952] B. Rossi, *High-Energy Particles*, (Prentice-Hall 1952).

[Raubenheimer 1995] T. Raubenheimer has carried out these first estimates of expected tail populations. Further detailed studies are recommended. Private communication (1995).

[Raubenheimer 1994] T.O. Raubenheimer, "Bunch Compressor Parameters", NLC–Note–2 (1994).

[SLC] Recent experiments with collimator wakefield kicks are indicating that the wake kick is about three times larger than predicted by theoretical formulas. It appears to have the gap behavior appropriate to a resistive-wall wake, but a geometric source is not ruled out.

[Shintake 1995] Rf BPMs with a resolution of 40 nm were demonstrated in the Dec. 95 FFTB run.

[Smith 1995] Private communication. Steve Smith designed and built the BPMs for the FFTB.

[Stupakov 1995] "Geometric Wake of a Smooth Taper", SLAC–PUB–7086 (Dec. 1995).

[Stupakov 1996] This limit was computed by G. Stupakov. Private communication.

[von Holtey] G. von Holtey suggested the use of curved collimators for this reason. G. von Holtey, "LEP Main Ring Collimators", CERN/LEP–BI/87–03.

[Walz 1973] D. Walz, D. Busick, T. Constant, K. Crook, D. Fryberger, G. Gilbert, J. Jasberg, L. Keller, J. Murray, E. Seppi, and R. Vetterlein, "Tests and Description of Beam Containment Devices and Instrumentation–A New Dimension in Safety Problems", SLAC–PUB–1223 (1973).

[Walz 1991] D. Walz has provided the information on properties of materials used in this chapter.

[Walz 1992] "NLC Final-focus Collimation and Dumping", Working Group Talk, Final Focus and Interaction Region Workshop, (1992).

[Warnock] According to Warnock the resistive-wall wake is not given by this integral in perturbation theory (for small disturbances of the beam wall). Private communication. However, we know of no better approximation to use for these deep tapers.

[Yan] Y. Yan has created and analyzed the maps used to analyze the chromatic behavior of the beam delivery beam line.

[Yokoya 1988] "Impedance of Slowly Tapered Structures", CERN SL/90-88 (AP).

[Yokoya 1991] K. Yokoya and V. Telnov prepared estimates of this at the LC91 workshop in Protvino, USSR. The argument here follows a transparency prepared by K. Yokoya.

[Yokoya 1995] K. Yokoya has pointed out the importance of the on-axis wakes for parallel plate collimators. We thank K. Bane for communicating these results.

[Zimmermann] F. Zimmermann, "Longitudinal Single-bunch Dynamics and Synchrotron Radiation Effects in the Bunch Compressor", NLC–Note 3 (1994).

Contributors

- K. Bane
- Y. Cai
- A. Drozhdin
- R. Helm
- L. Keller
- J. Irwin
- R. Messner
- R. Nelson
- T. Raubenheimer
- G. Stupakov
- F. Tian
- D. Walz
- M. Woodley
- Y. Yan
- F. Zimmermann